Light Scattering in the Rainbow Region of a Large Particle by Vectorial Complex Ray Model and Physical Optics

Ce Zhang

Normandie Université

THESIS

For the degree of Doctor of Philosophy

Specialty: PHYSICS

Prepared at the University of Rouen Normandie

Light Scattering in the Rainbow Region of a Large Particle by Vectorial Complex Ray Model and Physical Optics

Presented and defended by

Ce ZHANG

publicly on 26/10/2022
before the jury composed of

Fabrice ONOFRI	Director of research at IUSTI CNRS UMR 7343, Aix-Marseille University, France	Reviewer
Bing WEI	Professor at Xidian University, China	Reviewer
Bingqiang SUN	Director of research at Fudan University, China	Reviewer
Philip LAVEN	Researcher at 9 Russells Crescent, Horley RH6 7DJ, United Kingdom	Guest
Marc BRUNEL	Professor at University of Rouen Normandie, CORIA-UMR 6614, France	Examiner
Loïc MÉÈS	Research fellow at LMFA CNRS UMR 5509, Ecole Centrale de Lyon, France	Examiner
Claude ROZÉ	Professor at University of Rouen Normandie, CORIA-UMR 6614, France	Co-supervisor
Kuan Fang REN	Professor at University of Rouen Normandie, CORIA-UMR 6614, France	Supervisor

Thesis directed by Kuan Fang REN and Claude ROZÉ, at laboratory CORIA-UMR 6614

UNIVERSITÉ DE ROUEN NORMANDIE

ED PSIME

CORIA UMR 6614

Acknowledgements

This thesis would not have been completed with much guidance, encouragement and support from many people. I want to take advantage of this opportunity to express my heartfelt thanks.

Firstly, I would like to express my sincere gratitude to my supervisors Kuan Fang REN and Claude ROZÉ of their insightful guidance and patient cultivation. Their rigorous attitude towards academic research, strong sense of responsibility and enthusiasm for work have affected me deeply during the past three years. This thesis contains their invaluable instructions and support from beginning to end.

I want to acknowledge the financial support from the China Scholarship Council for my study in France as a Ph.D student.

I also want to express my gratitude to my friends those met in France, Dr. Rui Ping YANG, Dr. Lin Lin JIA, Dr. Chao REN, Dr. Jie XU, Dr. Jing ZHANG, Dr. Xue Fei WANG. We ever travelled in different countries, played cards, drank coffee, celebrated the Chinese Spring Festival, joked and helped with each other in our daily life. With their accompany, my life in France became more colorful and interesting.

I want to express my love to my parents and my sister. With their supporting and caring, I have energy to finish this thesis.

Finally, I especially thank the scholars and experts for reviewing this thesis.

Ce ZHANG

25/09/2022

Université de Rouen Normandie

List of Symbols and Abbreviations

Roman Symbols

a : radius of a sphere or a circular cylinder or semi-axes of an ellipsoid or an elliptical cylinder along x
b : length of semi-axes along y
c : length of semi-axes along z
d : distance between two successive interaction points of a ray with particle surface
m : relative refraction index
t : refraction coefficients or time factor
k : wave number
$\vec{k}$: wave vector
$\vec{r}$: position vector
$\hat{n}$: unit vector normal to the particle surface
$\hat{\mathrm{t}}$: unit vector tangent to the particle surface
ω : angular frequency
r_{X} : reflection coefficients
r : distance from the exit point to the observation point
R : curvature radii of the wavefront
D : divergence factor
$\vec{\mathrm{E}}$: electric vector
$\vec{\mathrm{H}}$: magnetic vector
$\vec{\mathrm{S}}$: Poynting vector
$\hat{e}$: polarization vector of electric vector
E : amplitude of electric vector
N : number of rays
I : intensity of light

Greek Symbols

ϵ : Fresnel factor: amplitude ratio of the emergent wave to the incident wave due to reflection and refraction coefficients
λ : wavelength of light
θ : scattering angle in 2D
ρ : curvature radii of the particle surface
τ : complementary angle of incident angle
τ' : complementary angle of refracted angle
Φ : phase of light or wave
α : size parameter of the particle

Subscripts or Superscripts

i : incident
l : reflected
r : refracted
e : emergent
n : component in normal direction
τ : component in tangent direction
f : focal line
$\parallel$: parallel polarization
$\perp$: perpendicular polarization
X : polarization of electric vector : $\perp$ or $\parallel$
ν : perpendicular (1) or parallel (2) to incident plane of the curvature radii
p : order for scattering ray
q : Number of interactions of a ray with particle surface
R : rainbow angle
B : Brewster angle
c : critical angle

Abbreviations

GO	: Geometrical Optics
LMT	: Lorenz-Mie Theory
DDA	: Discrete Dipole Approximation
FDTD	: Finite Difference Time Domain
VCRM	: Vectorial Complex Ray Model
II-TM	: Invariant Imbedding T matrix
GO+PO	: Geometrical Optics and Physical Optics
MLFMA	: Multilevel Fast Multipole Algorithm
VCRM+PO	: Vectorial Complex Ray model and Physical Optics

Contents

List of Figures

List of Tables

Chapter 1

Introduction

Research on light scattering by particles is a fundamental domain. Many scientists like Fermat, Descartes, Newton, Airy ever studied in this field [1–3]. Even today, it is still an active area both for science and industry [4, 5].

In our daily life, the phenomena like rainbows (in Figure 1.1), glories and the blue sky, are all relevant with light scattering by particles. Understanding their physical principles is always the pursuits of mathematicians and physicists [6, 7]. In industry, laser technology was developed in 1960. It was largely used in different domains like chemistry [8], medicine [9–11], meteorology [4, 12], atmosphere science [13, 14], remote sensing [15] because of its advantages in accuracy, efficiency and non-invasion.

In these conditions, the theory of light scattering by particles plays the roles connecting the relation between the scattered field and the particle parameters. According to this relation, the particles parameters can be reversed by its scattered field (the parameters of the incident field being known). Such relation is useful in industry and science, such as, for the particles like flow or spray, their optical character is helpful to improve the liquid fuel utilization efficiency in atomization [16–18]. The optical properties of particles, like ice crystal, can also help us to study climate change [13, 14].

In the field of optical metrology, many optical measurement techniques have been developed to measure different parameters of the particles, like particle tracking velocimetry, particle image velocimetry, laser Doppler and phase Doppler measurement, phase rainbow refractometry, global rainbow technique [16, 17, 19]. According to the scattered field and the theory of light scattering by particles, we can reverse the particles parameters like particle size, shape, temperature and velocity.

Figure 1.1 – Rainbows above lab. CORIA. taken by Ce ZHANG on 01/10/2019

So, the research on the theory of light scattering by particles is crucial.

In this thesis, our attention is on the development of an accurate and efficient model for light scattering by large particles near the rainbow region. In the following sections, the basic models of light scattering by particles and the rainbow theories are introduced respectively.

1.1 Models for scattering by particles

Different models for theory of light scattering by particles have been developed. These models are mainly divided into three kinds as analytical (or rigorous) methods, numerical methods and approximate methods [20–22]. In this section, these models are briefly introduced.

Analytical methods The analytical method is proposed by Lorenz [23], and Mie [24] independently, for scattering of an incident plane wave by an isotropic homogeneous sphere in 1890 and 1908. Its solution takes the form of an infinite series summations and now known as Lorenz-Mie theory (LMT) or Mie theory [25–28]. The Debye theory is also an analytical method and it gives the LMT series solution a clear physical interpretation as multi interactions process between the wave and particle [29]. So, it can be used to study the contributions of each order of the wave to the scattered field.

The analytical methods have been developed for many years and its application conditions are extended. For example, the scattered field of the multi-layered circular cylinder [30] and sphere [31] have been solved, the generalized LMT [27] is raised for the spherical particles illuminated by the Gaussian beam. However, because some separation variables technique is used, the analytical methods are limited to particles of every simple shape, such as sphere, infinite circular cylinder. For scattering of non-spherical particles, like an ellipsoidal particle, it is very difficult to deal with [32, 33].

Numerical methods The numerical methods can be further divided into two kinds as differential and integration methods [34].

The finite-difference time domain (FDTD) is proposed by Yee in 1966 based on Maxwell differential equations [35, 36]. In this model, the scatterer and fields are discretized as a lot of the cubic cells. Owning to the flexibility this model, Yang and Liou used FDTD to simulate light scattering by non-spherical particles as ice crystals [37]. But, FDTD is usually applicable to the particles whose size parameter $\alpha = ka$ is smaller than 20 in 3D because of its time-consuming computation and heavy memory requirements, where k is the wave number, a is the radius of the sphere.

The discrete dipole approximation (DDA) is proposed by Purcell and Pennypacker [38] in 1973, who replaced the scatterer by a set of point dipoles. These dipoles interactions are approximated by the integral equation for the electric field. This basic model can be used to non-spherical particles scattering. However, as particle size or relative refraction index m increases, the requirement of the computer resource both in time and memory increases quickly. Even when the parallel computation technique is used, it takes 7.5 hours and used 512 processors and 700Gb memory for light scattering by a sphere with size parameter $\alpha = 320$ and $m = 1.05$ [39].

The method of moments [40] is based on the integration method for the electric and magnetic currents on the particles surface. Due to the development of multilevel fast multipole algorithm (MLFMA), the computational complexity reduced from $O(N^2)$ to $O(N \log N)$ [41]. In 2015 [42], MLFMA was applied to light scattering by non-spherical particle in 3D problems. However, it takes 18.9 hours and used 200Gb memory for light scattering of a particle size near 400.

The T-matrix is raised by Peter Waterman in 1965 [43, 44]. Because its incident

and scattered fields are expressed in vector spherical functions like LMT, it might be the most accurate and efficient numerical method for light scattering by non-spherical particles. That is why many scholars researched this method like Barbar, Hill, Mishchenko [45, 46] etc. In 1988 , invariant imbedding T matrix (II-TM) is proposed by Johnson [47] for scattering of an arbitrarily shaped, inhomogeneous, dielectric object. In 2014, Bi and Yang used II-TM to compute the optical properties of randomly oriented ice crystals, and optical effects of surface roughness and inhomogeneity are investigated [48]. However, II-TM is restricted by the memory limitation because the memory demand increases drastically with respect to the particles size, especially for asymmetric particles.

Though these numerical methods are accurate and can be used to simulate the light scattering of non-spherical particles, the simulation is limited by the particle refractive index m or symmetry or computation consumption both in time and memory when the particle size is large even with help of parallel computation. Therefore, finding other efficient and accurate models is still necessary.

Approximate model For light scattering by large particles, the approximate models are usually preferred because of its flexibility and efficiency. These approximate models mainly fall into two categories: One is the ray model, the other is the wave model.

Ray model: Geometrical optics (GO) is one of fundamental approximate methods based ray model and it assumed that the wavelength is much smaller than the size of the particle or objects [4, 49, 50]. In a homogeneous medium, the rays propagate along straight lines.

For light scattering by a large spherical water droplet, the scattering patterns of GO and LMT match well except in the forward region (near the $\theta = 0°$) and in the neighbour of rainbow angles [4, 28]. For light scattering of a large spherical air bubble, its scattering patterns are in agreement between GO and LMT except in the forward region and critical angle [51, 52]. Though the GO has defects in some regions, its accuracy is inspiring for spherical particles in general.

For light scattering of a large non-spherical particle with smooth surfaces, because there is no analytical form of the divergence factor as for spherical particles [4], the vectorial complex ray model (VCRM) is proposed by Ren et. al [53]. In VCRM, the wavefront is integrated as an intrinsic property of a ray, the relationship between the curvature radii of wavefront and the curvature of the surface are

expressed by the wavefront equation [50, 53, 54]. So, the divergence factor and the phase shift of focal line can be calculated directly. Therefore, VCRM provides a feasible method for light scattering of a plane wave or shaped beam by a large particle with arbitrarily smooth surfaces.

Based on VCRM, light scattering by some non-spherical particles on the equatorial plane had been made and compared with experimental results and numerical method [42, 53, 55, 56]. In 2011, Ren et al. proposed VCRM for light scattering by an ellipsoid on its equatorial plane (or symmetrical plane) illuminated by a plane wave. For spherical particles, the VCRM and GO have the same scattering pattern [53, 57]. In 2013, Jiang et al. applied it to the scattering of Gaussian beam by an elliptical cylinder, and the scattering intensities in different observation distances are presented [58]. In 2015, experimental validation of VCRM for the scattering of an oblate droplet is made by Onofri et al. The two principal radii and refractive index of the droplet are retrieved [55]. Yang et al compared the scattering diagrams for a non-spherical particle between VCRM and MLFMA. The good agreements between them proved the ability of both MLFMA and VCRM for scattering by large non-spherical particles [42]. In 2017, Duan et al studied the effect of curvatures for a liquid jet to its rainbow positions by experiment measurements and theoretical analysis [59]. In 2019, Duan et al reported the VCRM in 3D for light scattering by a real liquid jet. A good agreement has been found between the scattering patterns of the VCRM stimulation and the experimental measurements [60]. Yang applied the statistical VCRM proposed by Rozé to light scattering of a pendant droplet. Comparisons between experimental measurements and statistic VCRM have been made but it requires a lot of computation resources both in time and memory [61]. In 2020, Duan et al studied light scattering by a composite infinite elliptical cylinders. The effect of the particle's parameters like particles shape, refraction index (affected by the temperature) and the direction of incident wave are analysed [62]. In 2021 [56], Duan et al studied light scattering of oblate drops in the rainbow region by VCRM in 3D and compared the scattering patters with experimental measurement. The scattering patterns by VCRM and experiment measurement are in agreement except in the caustics regions. One caustic is still at rainbow angle in incident plane, the other caustic being in perpendicular plane.

Therefore, VCRM can simulate the light scattering by large particles with smooth surface of plane wave or shaped beams. Their validations have been proved with a good accuracy except in the forward region and rainbow region.

Wave model: The physical optics (PO) as one of fundamental methods in wave model has been used to scattering of large particles or scatterers.

For light scattering by spherical particles in the forward direction, the scattering field is considered as a wave diffracted by an circular disk [4, 53, 63]. For light scattering by a large spherical water droplet in the rainbow region, GO fails because of infinite intensity. Airy in 1830s proposed his method based on the idea combining GO and PO for the scattering in the rainbow region on the equatorial plane of a sphere [3]. However, the positions and intensities of the supernumerary bows predicted by Airy theory differ from those of rigorous Debye theory with increasing the order of ray and the scattering angle from the rainbow angle [64, 65]. For light scattering by a large spherical air bubble in water, the derivative of the scattering intensity calculated by the GO is not continuous in the critical angle. In 1979, Marston proposed his method based on diffraction theory with a similar idea as Airy theory for rainbow [51]. The scattering intensities near the critical angle are shown by simulation and experimental measurements. In 2016, Sentis et al calculated scattering intensities of an air bubble by combining GO and PO [66]. But there still are some discrepancies between this combined method and LMT near the critical angle region. It is probably due to the inaccuracy approximations of the emergent wavefront near critical angle and infinite integral region in Fresnel integral.

For light scattering by non-spherical particles of ice crystals with *plane surface*, Ping Yang and KN Liou proposed a GO integral equation method in 3D case based on electromagnetic equivalence theorem [67]. The near field character is described by GO and ray tracing is applied to calculate the multi-interactions between the light and the particle. The scattering field integral on the particle surface is based on the principle of PO. The comparisons of this GO + PO model and FDTD had been made with a good accuracy for the size parameter smaller than 20. By the method GO + PO, light scattering of a particle aggregated by 8 hexagonal columns had been simulated where the size parameter is to 1000 [68]. By the two methods of T-matrix and GO + PO, light scattering of the non-spherical particle whose size parameters is in the regime of 0.1 to 2000 is reported, where T-matrix is for the regime of 0.1 to 150, GO+PO is for the regime of 100 to 2000.

For scattering of a non-spherical scatterers like an opening arbitrarily shaped cavity with curved surfaces [69], the combining method GO + PO (also called *Shooting and bouncing rays* in reference [69]) was also applied for its scattering field. The comparisons of scattering diagrams of a large open-ended perfect electric conduct-

ing circular cylinder between GO + PO and rigorous model analysis [70] were made with a good agreement. The size of the circular cylinder is 40λ in length and 20λ in diameter. However, the reason why its integral area was on the outlet of the cavity was not given (The divergence factor of a ray is affected by this integral area).

In fact, besides GO and PO, there are other approximate models like, geometrical diffraction theory [71, 72], physical diffraction theory [73, 74], and uniform geometrical theory of diffraction [75]. These models are the extensions of GO or PO and they are for scattering of the particles or scatterers with *edges* (or diffraction in shadow). In this thesis, we focus on the light scattering by the particles with curved smooth surfaces[1], the diffraction of light by the edge of particle is not considered.

Therefore, for light scattering by large particles, the analytical methods are limited to the scattering by very simple form, the numerical methods are limited by the expensive computation resource and the particle's refraction index and symmetry. The approximate models, such as GO, VCRM, PO and their combination are promising and will be used in this thesis to study the light scattering of large particles (like infinite cylinder with circular or elliptical section, sphere and ellipsoid) in the rainbow region.

In this thesis, our topic is for light scattering by large particles with smooth surface in its rainbow region. The theories of light scattering near rainbow region are called as rainbow theories. In the following section, the rainbow theories are introduced.

1.2 Rainbow theories in light scattering by spherical particles and non-spherical particles

Rainbow is one of the most beautiful phenomena in nature. It occurs intensively in different cultures, arts and philosophies because of its pleasant and inspiring visual display [1, 76]. Since ancient time, in order to understand its formation, many scientists and mathematicians studied it.

In the following, the rainbow theories are introduced in two categories. One is for light scattering by spherical particles, the other is for non-spherical particles.

[1] It means that the particle surface is differentiable to the second order or more

Rainbow theories for spherical particles For light scattering by spherical particles, Descartes, based on his novel discovery of reflection and refraction, gave experimental verification and the numerical calculation of the direction of the rainbow [1]. The formation of rainbow in nature explained by Descartes is shown in Figure 1.2

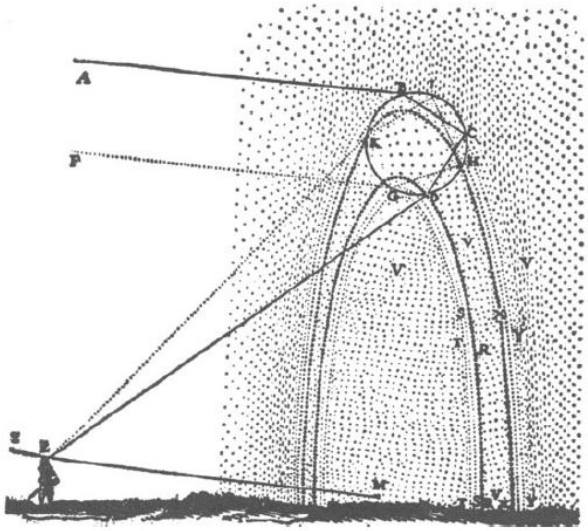

Figure 1.2 – Descartes' diagram to illustrate the formation of the rainbow.

Newton explained the colours of rainbow by optics dispersion in water drops. However, the intensity at rainbow angle trends to infinite in GO (known as caustics problem), as shown in Figure 1.3.

In the 1830s, Airy proposed his method based on diffraction theory for the intensity of light in the neighbourhood of a caustics [3]. In Airy theory, the diffraction theory is applied to calculate the intensity in the rainbow region [4]. So, the amplitude and phase are required. For the amplitude at emergent point, Airy assumed it as a constant determined by Fresnel's coefficients in optical path. For the phase of the emergent wave near rainbow angle, Airy calculated it approximately as a cubic function. In order to compute the rainbow integral, its integral region is extended to infinite [77]. According to Airy theory, the formation of the rainbow is explained by diffraction theory, the amplitude and phase are calculated by GO. From the author knowledge, such a method firstly built a basic model of the combining method GO + PO.

After Airy theory, many scholars continued to study his theory and pointed its flaws. Based on Airy theory, Pernter's contribution was the detailed applica-

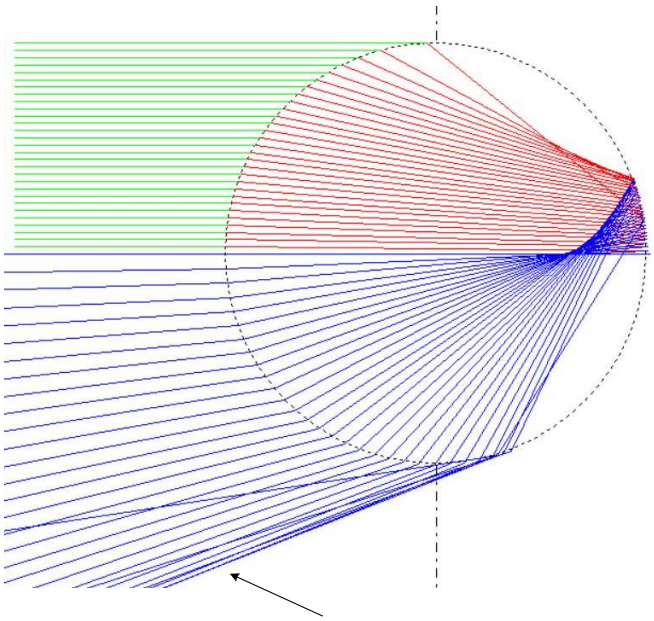

Figure 1.3 – The infinite amplitude of the edge ray (or rainbow ray) in light scattering by a spherical water drop.

tion of Airy theory to the rainbow so as to disentangle the various colour formations [12, 78, 79]. A high frequency scattering by a transparent sphere was made by Nussenzveig for the rainbow [80]. The modified Watson transformation was applied to the rigorous Debye theory in his method. Khare and Nussenzveig compared the scattering patterns between their method, which later was known as complex angular momentum theory, Mie theory and Airy theory near the rainbow region [81–83], the failure of Airy theory in parallel polarization was shown.

In order to improve the Airy theory in parallel polarization, Können and de Boer took into account still based on diffraction theory the strong variation of the amplitude around the Brewster angle, where the Fresnel coefficient was expanded in the neighborhood of the angle, but they had not given any quantitative comparisons with the rigorous method [6, 84]. Only Laven gave its real scattering diagrams but still no comparison was made with rigorous method [85].

Wang and Van de Hulst compared the scattering patterns between LMT and Airy theory for higher order near the rainbow region, but the comparisons was not clear because the contributions of different orders are included in LMT. Besides, the enhancement factor $\alpha^{1/3}$ of the peak intensity was pointed and explained its from scattering diagrams, but their explanations for the enhancement factor are not reason-

able. Nussenzeig's comment on the enhancement was from his own method [86], but no reasonable analyses were given. Hovenac and Lock compared the scattering patterns between Airy theory and Debye theory near the rainbow region, obvious discrepancy was observed with increasing with the order of ray and scattering angles from the rainbow angle [65].

Nowadays, benefit from development of computer technology, though the direct computation of the rigorous LMT or Debye theory for spherical particles scattering is feasible on ordinary laptop computer, e.g. with Laven's MiePlot software or Ren's ABSphere software [87, 88], the research on light scattering by spherical particles is still meaningful. Because, for the models like GO and PO, not only can they give a simple and intuitive understanding like the interference and diffraction principle, but also these models can be extended to non-spherical particles easily.

Rainbow theories for non-spherical particles We briefly divide the rainbow theories for light scattering by non-spherical particles into three kinds. The first kind is based on Möbius method. The second kind is the catastrophe optics which is the same principle as Airy theory for rainbow. The third kind is based on ray model. In the following, the developments of these methods are introduced.

In 1909, Möbius firstly discussed the rainbows of flattened water drops [89, 90]. using Möbius method, Lock studied the behavior of the first and second order rainbows produced by a normally illuminated glass rod and examined by experimental measurement. Its cross section was nearly elliptical [91]. However, this approach is limited by the particle shape that is close to a sphere, and there is no comparison of scattering patterns between Möbius method and any rigorous method [79, 92, 93].

The catastrophe optics was developed for light scattering by particles near the caustics regions. In 1946, based on the idea of Airy theory for rainbow, Pearcey studied the structure of an electromagnetic field in the neighbourhood of a cusp of a caustic [94]. In 1975, Berry studied the wave character of the caustics in different kinds. The Thom's theorem was applied to classify the different caustics diffraction integrals (in polynomials form) [95–97]. Then, Nye and Berry studied caustics of liquid drops and examined by experimental measurement and theoretical analysis, where the theoretical analysis of the diffraction field is based on the local caustic structure, the stationary phase method is used for diffraction integrals [98–100]. Based on this, the catastrophe optics is gradually developed. In 1984, Marston and Trinh observed hyperbolic umbilici diffraction catastrophe near the rainbow region

for light scattering by oblate spheroidal drops. The diffraction patterns are sensitive to the ratio of a/c, where a is the radius of the circular cross section between the incident light and the oblate spheroidal on its equatorial plane, c is the radius in the perpendicular plane. Nye analysed how this ratio a/c affected the diffraction catastrophe based on GO and catastrophe optics [101, 102]. In 1985, Marstion explained the generalized rainbows from cusp diffraction catastrophe and pointed its application in inverse scattering [103]. In 2010, for light scattering by an oblate spheroid, Lock and Xu studied different kinds optical caustics of the rainbow, transverse cusp, and hyperbolic umbilic caustics were analysed based on catastrophe optics quantitatively [32].

Based on ray model, in 1998, Lock et al studied the intensity of high order rainbows by geometric ray theory for normally incident light of a cylinder with an elliptical cross section. The amplification for the intensity of high orders rainbow was observed and analyzed by total internal reflection of the rays near rainbow region [104]. Yu studied the rainbow caustics line in 3D based on vector-ray tracing model for non-spherical particles. In 2013, Yu et al studied the secondary rainbow caustics line of oblate droplets in the equatorial plane by vector-ray tracing model [105, 106]. Because this vectorial ray tracing model is based on GO, only the boundary limits of the rainbow can be calculated. But these boundaries limits are not the real intensity maximum in rainbow patterns. So, only the curvature of the caustic line is relevant with particle shape. Besides, because the interference phenomenon is not considered, the supernumerary structure can not be predicted. So, the parameters of particle size can not be taken into account.

There are some other methods for the rainbow of non-spherical particles. Lock and Adler researched the semi-classical scattering theory to analyse the exterior caustics produced in scattering of a diagonally incident wave by a circular cylinder [107, 108]. The comparisons between semi-classical approximation, ray theory and wave scattering theory were made. When an elliptical cross section cylinder is normally illuminated by a plane wave, the supernumerary spacing for scattering pattern are analysed in theory and experimental measurement. It is affected sensitively by the shape of its cross section. In 2002, the first order rainbow of a coated cylinder was examined by experimental measurement as the coating thickness changes [109]. There are twin rainbows produced for the large thickness a coated cylinder, there was a single rainbow for the small thickness a coated cylinder but with intensity varies periodically as the coating thickness varies.

In recent years, the study on rainbow theories is still under developments. In 2017, Lock and Können analysed the high-order rainbows of a flattening droplet by combination Möbius and Airy approximations [93, 110]. From interference theory, Laven pointed out the phase shift $\frac{\pi}{2}$ in the supernumerary arcs of rainbows [4, 111]. In 2019, Yu et al studied the primary rainbow caustics from tilted spheroidal drops [112]. In 2021, Berry studied the images in mirrors whose curvatures are convex in some places and concave on other places. The theoretical analysis is attributed to the scattering near caustics [113, 114]. Duan et al studied the scattering patterns of oblate water droplets by VCRM in 3D near the rainbow region and compared with experimental measurements. However, the intensities near caustics fails like GO. In 2022, Marston recalled his communications with Mishchenko on the rainbow in light scattering by oblate spheroidal drops. The developments on the study of rainbow problems were reported [115].

In the aspect of experimental measurement of rainbow and its applications, in 2016, Wu et al developed a one-dimensional phase rainbow refractometry to measure the droplet size at the micrometers scale as well as the tiny droplet diameter variations at the nanoscale [116]. In 2018, Wu et al used the phase rainbow refractometry to measure the droplet temperature (or refraction index), size and evaporation rate [117]. However, these measurement techniques are limited to spherical particles. The measurement of non-spherical particles by rainbow technologies is dependent on the rainbow theory of non-spherical particles.

Therefore, the developments of rainbow theories never stop from ancient to today. It helps us further understand the interactions between light and particles. This makes the basement for applications both for rainbow technologies and other fields that light scattering related.

1.3 Motivation and structure of the thesis

The author is motivated by the light scattering in the rainbow region of a large particle by the method VCRM + PO. The VCRM can calculate the phase and amplitude of all the emergent rays rigorously in the sense of ray model, PO permits to take into account the diffraction in the rainbow region. The structures of the thesis are organized as follows:

In Chapter 2, the fundamentals of GO and PO are introduced. The light scattering of an large infinitely circular cylinder and a large sphere are presented in the

framework of GO by taking into account the diffraction effect in the forward direction.

In Chapter 3, the fundamentals of VCRM are introduced. The light scattering by non-spherical particles like an infinite elliptical cylinder or an ellipsoid are simulated by VCRM.

In Chapter 4, by combining method VCRM + PO, light scattering in the rainbow region by the particles like an infinite circle cylinder or a sphere are introduced.

In Chapter 5, because of the flexibility of VCRM + PO, this combining method is extended to light scattering of non-spherical particles near its rainbow region.

In Chapter 6, the conclusions and perspectives of this thesis are summarised.

Chapter 2

Geometrical optics and physical optics for light scattering

The geometrical optics (GO) and the physical optics (PO) are two fundamental approximate models to describe the interaction between light and objects. They can be used to deal with light scattering by particles in different conditions [4]. In this chapter, we will recall their fundamental laws and apply them to the light scattering by infinite circular cylinders and spherical particles. The concepts and the laws introduced here will be served as a base and a reference to the study of light scattering by a non-spherical object with the Vectorial Complex Ray Model (VCRM) in the following chapters.

The GO is an efficient and flexible model for light scattering by particles. It is admitted often that GO is applicable to the particles of size much bigger than the wavelength. In fact, this is just a necessary condition. The precision of the GO depends also on the phenomena and the scattering regions under study. For example, in the vicinity of the GO rainbow angles and in the forward direction, the GO fails to predict correctly the scattering intensities what ever the size of the particle. In these cases, the wave properties of the light must be considered. In this thesis, the physical optics or simply the Huygens-Fresnel principle will be applied to take into account the diffraction effect in light scattering by particles.

2.1 Geometrical optics

In the GO, the waves are described by bundles of rays and the rays propagate rectilinearly in a homogeneous medium. The electric field of a monochromatic electro-

magnetic wave [50] of angular frequency ω along a ray is given by

$$\vec{\mathrm{E}}(\vec{r},t) = \mathrm{E}(\vec{r})\exp\left[-i(\vec{k}\cdot\vec{r}-\omega t-\Phi_i)\right]\hat{e}. \tag{2.1}$$

where $\mathrm{E}(\vec{r})$ is the amplitude at point $\vec{r}$ and time t, $\vec{k}$ the wave vector defined as $\vec{k} = k\hat{k}$, $k = 2\pi/\lambda$ being the wave number, λ the wavelength, $\hat{k}$ the unit vector of the propagation direction, $\hat{e}$ the polarization direction of electric vector, ω is its angle frequency, Φ_i is the initial phase, i is the imaginary unit.

When a ray impinges on a surface of an object (diopter), it will be reflected and refracted. The directions and the amplitudes of the reflected and refracted rays depend on the incident angle, the refractive index of the two media and the polarization state, i.e. the direction of $\vec{\mathrm{E}}$ relative to the incident plane defined by the normal of the diopter and the incident ray.

2.1.1 Fundamental laws

Snell's laws Consider a ray incident on a diopter from a medium of refractive index m_i to another medium of refractive index m_r with a incident angle θ_i relative to the normal of the diopter, then the reflection angle θ_l and the refraction angle θ_r are given by the Snell's laws

$$\theta_i = \theta_l, \tag{2.2}$$

$$\sin\theta_i = m\sin\theta_r. \tag{2.3}$$

where $m = m_r/m_i$ is the relative refractive index. The Snell's laws state also that the incident ray, the reflected ray and the refracted ray are all in the incident plane defined by the incident ray and the normal of the diopter.

Fresnel's formulas: The amplitudes of the reflected and the refracted rays are proportional to that of the incident field and described by their ratios to the incident amplitude. These ratios depend on the polarization state and can be determined by the boundary conditions of the electromagnetic fields $\vec{\mathrm{E}}$ and $\vec{\mathrm{H}}$ according to Figure 2.1. We will omit the derivation and give directly the Fresnel formulas as follows:

$$r_\perp = \frac{\mathrm{E}_\perp^l}{\mathrm{E}_\perp^i} = \frac{\cos\theta_i - m\cos\theta_r}{\cos\theta_i + m\cos\theta_r} = -\frac{\sin(\theta_i-\theta_r)}{\sin(\theta_i+\theta_r)}, \tag{2.4}$$

$$t_\perp = \frac{\mathrm{E}_\perp^r}{\mathrm{E}_\perp^i} = \frac{2\cos\theta_i}{\cos\theta_i + m\cos\theta_r} = \frac{2\sin\theta_r\cos\theta_r}{\sin(\theta_i+\theta_r)}, \tag{2.5}$$

$$r_\parallel = \frac{\mathrm{E}_\parallel^l}{\mathrm{E}_\parallel^i} = \frac{m\cos\theta_i - \cos\theta_r}{m\cos\theta_i + \cos\theta_r} = \frac{\tan(\theta_i-\theta_r)}{\tan(\theta_i+\theta_r)}, \tag{2.6}$$

$$t_\parallel = \frac{\mathrm{E}_\parallel^r}{\mathrm{E}_\parallel^i} = \frac{2\cos\theta_i}{m\cos\theta_i + \cos\theta_r} = \frac{2\sin\theta_r\cos\theta_r}{\sin(\theta_i+\theta_r)\cos(\theta_i-\theta_r)}. \tag{2.7}$$

where r_X and t_X represent the reflection and the transmission ratios and the index

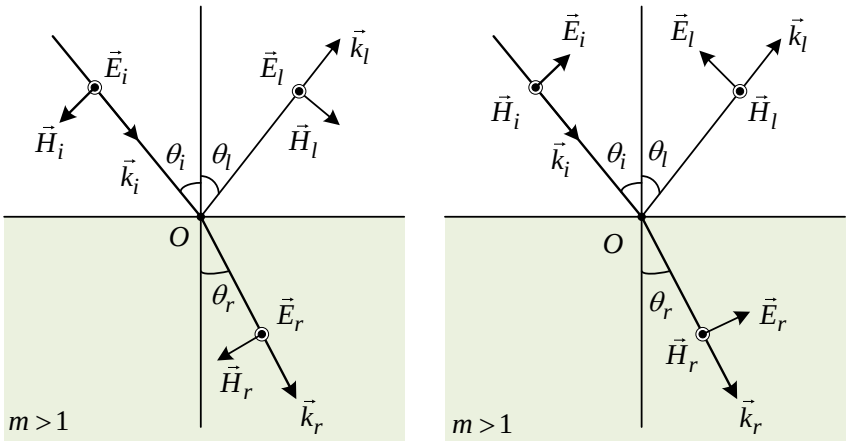

(a) Perpendicular polarization (b) Parallel polarization

Figure 2.1 – Schema for derivation of Snell's law.

X =$\perp$ or $\parallel$ stands for the polarization state: electric field perpendicular $\perp$ or parallel $\parallel$ to the incident plane.

Reformulation of Snell's laws and Fresnel formulas In the Snell's laws, the directions of the reflected ray and the refracted ray are described by the angles relative to the normal of the diopter. This is not convenient for 3D scattering. We will show in the following that the Snell's laws and the Fresnel formulas can be rewritten as function of the components of the wave vectors.

In fact, we multiply Eq. (2.3) by the wave number in the vacuum k and get $km_i\sin\theta_i = km_r\sin\theta_r$. This implies that the tangent component of wave vector of the refracted ray $k_{r\tau}$ is equal to that of the incident wave $k_{i\tau}$. Similarly, we can deduce that the tangent components of the reflected ray $k_{l\tau}$ and that of the incident ray $k_{i\tau}$ are also equal. Therefore, we conclude that the tangent components of the incident ray, the reflected ray and the refracted ray are all equal, i.e. the Snell's laws

can be rewritten simply as

$$k_{i\tau} = k_{l\tau} = k_{r\tau}, \tag{2.8}$$

The normal component of the wave vector of reflected ray k_{ln} is equal to that of the incident wave but in the opposite direction since they are in the same medium. The normal component of the refracted ray k_{rn} can be determined by its wave number k_r. So we have

$$k_{ln} = -k_{in}, \quad k_{rn} = \sqrt{k_r^2 - k_{r\tau}^2}, \tag{2.9}$$

Knowing that the normal component of a wave vector is the product of the wave number and the cosine of the corresponding angle relative to the normal of the diopter $k_n = k\cos\theta$, the Fresnel formulas can be rewritten as function of the normal components of the wave vectors

$$r_\perp = \frac{k_{in} - k_{rn}}{k_{in} + k_{rn}}, \tag{2.10}$$

$$t_\perp = \frac{2k_{in}}{k_{in} + k_{rn}}, \tag{2.11}$$

$$r_\parallel = \frac{m^2 k_{in} - k_{rn}}{m^2 k_{in} + k_{rn}}, \tag{2.12}$$

$$t_\parallel = \frac{2mk_{in}}{m^2 k_{in} + k_{rn}}. \tag{2.13}$$

The reflection ratios calculated by Eqs. (2.10) and (2.12) may be positive or negative. If the ratio is positive, the reflected electric field is in phase with the incident field, if the ratio is negative, the reflected field is in the opposite direction of the incident field, that is a phase jump of π.

When a ray propagates from a denser medium to a thinner medium ($m < 1$) and the incident angle is larger than the critical angle θ_c (i.e. $\theta_i > \theta_c = \arcsin(m)$ or $k_{i\tau} > k_r$), the total reflection will take place. The reflection ratios calculated by Eqs. (2.10) and (2.12) will be complex. In this case, $k_{rn}^2 = k_r^2 - k_{i\tau}^2$ is negative, Eqs. (2.10) and (2.12) are written as

$$r_\perp = \frac{k_{in} + i\sqrt{k_{i\tau}^2 - k_r^2}}{k_{in} - i\sqrt{k_{i\tau}^2 - k_r^2}}, \tag{2.14}$$

$$r_\parallel = \frac{m^2 k_{in} + i\sqrt{k_{i\tau}^2 - k_r^2}}{m^2 k_{in} - i\sqrt{k_{i\tau}^2 - k_r^2}}. \tag{2.15}$$

It is evident that the numerator and denominator in Eqs. (2.14) and (2.15) are conjugate to each other, so the moduli of amplitude ratios are certainly unity which reflects correctly the fact of total reflection. The argument of the complex ratios are the phase shift of the reflected field relative to the incident field. This phase shifts due to Fresnel coefficient, noted by Φ_F and calculated as follows

$$\Phi_F = \arg(r_X) \tag{2.16}$$

where r_X is the refection coefficients in polarization X. It is worth noting that Eq. (2.16) is applicable to all the cases discussed above: r_X positive, negative or complex.

Numerical results and discussion To illustrate the evolution of the amplitude and the phase of the reflected field as function of the incident angle, the refractive index and the polarization state, we present in the following the numerical results of the amplitude ratios and the phase shifts calculated with the Fresnel coefficients for the reflection of a light ray on a surface of water in two cases: air-water ($m = 1.333$) and water-air ($m = 0.75$).

Figure 2.2 shows the Fresnel coefficients of reflection and refraction on the surface air-water for the two polarizations. We find that the reflection coefficient is always negative for the perpendicular polarization, that means the reflected field is always opposite to the incident field (phase shift $\Phi_F = \pi$). For the parallel polarization, the Fresnel coefficient is positive when the incident angle is less than $\theta_B = \arctan(m) = 53.123°$ (called Brewster angle) and negative for a larger incident angle.

When a ray impinges on the surface water-air, the variation of the Fresnel coefficients (Figure 2.3) are similar to that of the reflection on the air-water surface with two particularities: (1) The curves are compressed to a narrow region from 0° to $\theta_c = \arcsin(m) = 48.590°$ (called critical angle) [51] and after this angle, the reflection is total. (2) The sign of the Fresnel reflection coefficients are opposite to that of the case air-water.

The phase shifts due to the Fresnel coefficients in the Figures 2.2-2.3 are clearly shown respectively in 2.4 and 2.5. Furthermore, the phase shifts in the total reflection region are also shown in Figure 2.5. It is important to note that this phase shifts vary contiuously from 0 at the critical angle to π at the tangent incidence.

The phase shifts of π [118] and in the total reflection are very important in the

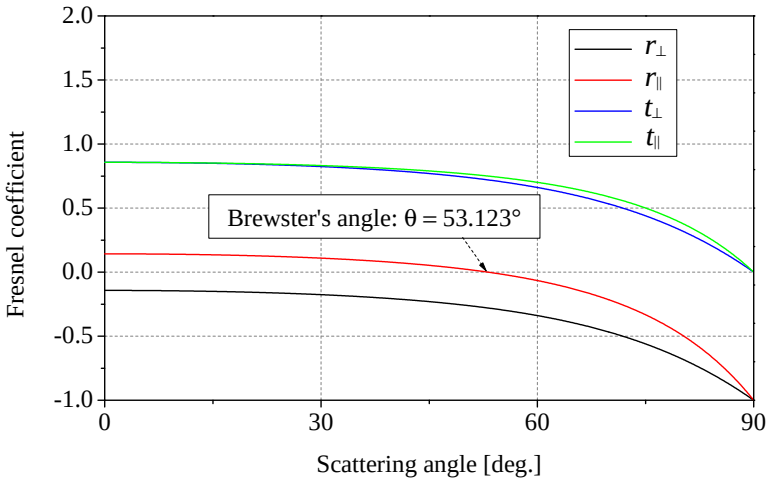

Figure 2.2 – Fresnel coefficients for a ray impinges on an air-water surface $m = 1.333$.

interpretation and understanding of certain phenomena such as the scattering by a bubble [51] and Goos–Hanchen effect [21].

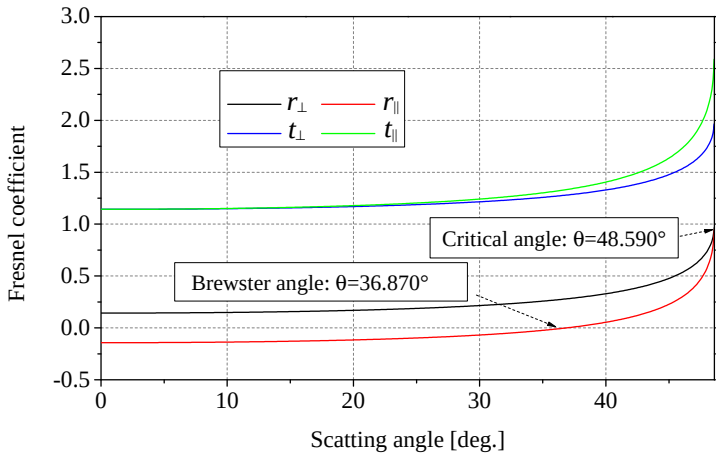

Figure 2.3 – Fresnel coefficients for a ray impinges on an air-water surface $m = 0.75$.

Finally, we should note that the amplitude ratios of transmission calculated by Fresnel formulas may be larger than unity (see Figure 2.3). This does not mean that the intensity of the transmitted wave is stronger than the incident one. This can be explained by the modulus of the Poynting vector which is defined as

$$\vec{S} = \vec{E} \times \vec{H} = \sqrt{\frac{\varepsilon}{\mu}} E^2 \hat{k} \tag{2.17}$$

where ε and μ are the dielectric constant and permeability respectively. In a non-

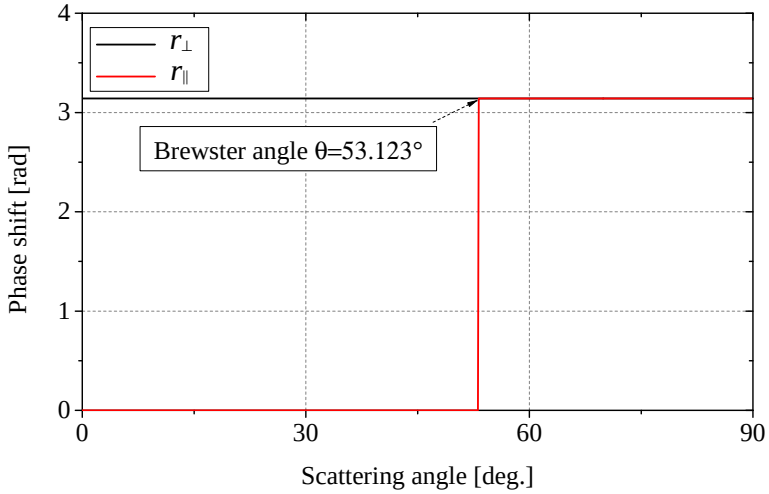

Figure 2.4 – Phase shifts in the reflection on an air-water surface.

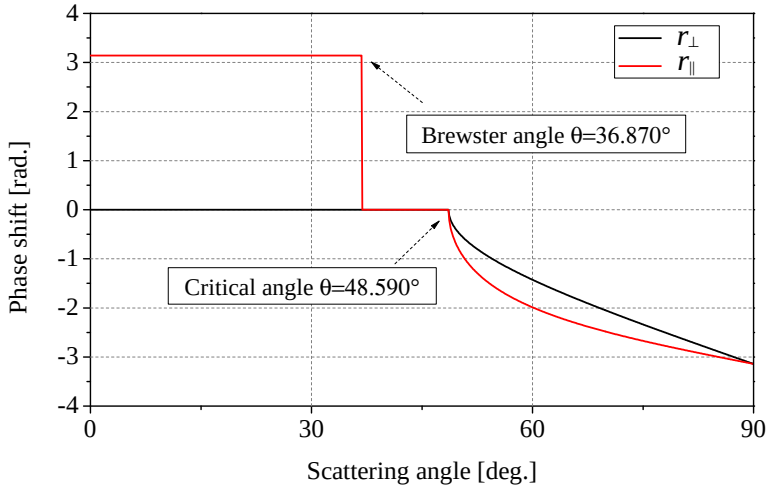

Figure 2.5 – Phase shifts in the reflection on a water-air surface.

magnetic medium $\mu = \mu_0$ and $\varepsilon = \varepsilon_0\varepsilon_r$, we know $m = \sqrt{\varepsilon_r}$, ε_r being the relative dielectric constant. So, the modulus of Poynting vectors of the incident, reflected and refracted waves are given respectively as

$$S_i = m_i \sqrt{\frac{\varepsilon_0}{\mu_0}} E_i^2 \cos\theta_i \tag{2.18}$$

$$S_l = m_i \sqrt{\frac{\varepsilon_0}{\mu_0}} E_l^2 \cos\theta_l \tag{2.19}$$

$$S_r = m_r \sqrt{\frac{\varepsilon_0}{\mu_0}} E_r^2 \cos\theta_r \tag{2.20}$$

where m_i and m_r are the refractive indexes in the incident and refraction media. Therefore, the ratios of reflected intensity and the refracted intensity to the incident intensity are respectively

$$R = \frac{S_l}{S_i} = \frac{m_i E_l^2 \cos\theta_i}{m_i E_i^2 \cos\theta_l} = |r|^2 \tag{2.21}$$

$$T = \frac{S_r}{S_i} = \frac{m_r E_r^2 \cos\theta_i}{m_i E_i^2 \cos\theta_r} = \frac{m\cos\theta_i}{\cos\theta_r} |t|^2 \tag{2.22}$$

We find that $R + T = 1$ is true for the two polarizations. This is consistent with energy balance.

2.1.2 Scattering by an infinite circular cylinder

The fundamental laws of the GO presented in the last section permit to calculate the amplitudes and the phases of all the reflected and refracted waves when a wave interacts with a particle, so it can be applied to predict the scattered field of an object when it is illuminated by a wave. To illustrate the procedure and examine some scattering properties, we begin with the simplest case: scattering of a plane wave of wavelength λ by a homogenous infinite circular cylinder at normal incidence (Figure 2.6).

1. Directions of emergent rays

The propagation of a ray in the cylinder is shown in Figure 2.7, where m and a are respectively the relative refractive index and the radius of the particle.

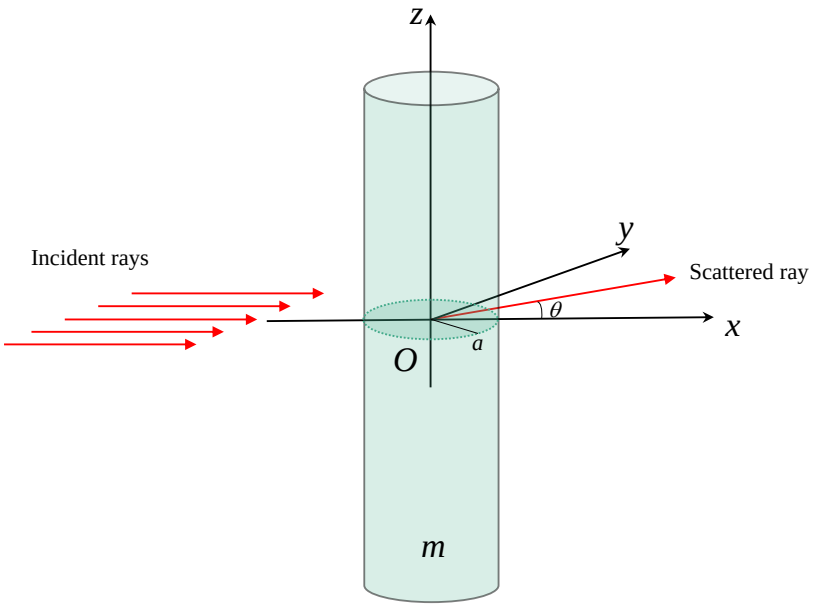

Figure 2.6 – A plane wave is scattered by an infinite circular cylinder.

The incident wave can be represented by N equal distant rays located at $y_i = (2t+1)a/\mathrm{N} - a$ with $t = 0, 1, 2 \ldots (\mathrm{N}-1)$. The coordinates x_i of the first interaction points are determined by the circle equation $x_i^2 + y_i^2 = a^2$. So, the first incident points on the particle are given as

$$\begin{aligned} x_i &= -a\sqrt{1-\tfrac{y_i^2}{a^2}} \\ y_i &= \left[\tfrac{2t+1}{\mathrm{N}} - 1\right] a \end{aligned} \tag{2.23}$$

The incident angle θ_i of all the rays are known.

According to the symmetry of the circle and the Snell's law, the derivation angle θ of the emergent ray of order p is given as

$$\theta_p = 2(\tau - p\tau'), \tag{2.24}$$

where τ and τ' are respectively the complementary angle of the incident angle θ_i and the refraction angle θ_r, i.e. $\tau = \pi/2 - \theta_i$, $\tau' = \pi/2 - \theta_r$. Owing to the symmetry, only the scattering intensity in the range 0 to π is necessary. The deviation angle θ_p is reduced to the scattering angle θ_p by

$$\theta_p = 2q_p(\tau - p\tau') + 2k_p\pi, \tag{2.25}$$

where q_p equals $+1$ or -1 and k_p is an integer that limits the angle θ in the range $[0, \pi]$.

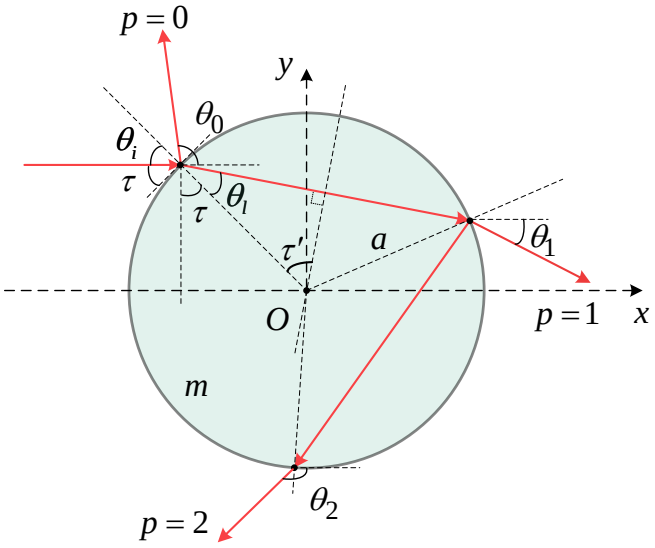

Figure 2.7 – Optical path in a circular cylinder.

2. Amplitude of a ray

When a wave is scattered by a particle of smooth surface, the amplitude of scattered wave is affected by two factors in the viewpoint of GO. One is due to the reflection and the refraction described by the Fresnel coefficients, the other is the divergence on the curved surface, which is described by the so called divergence factor.

The amplitude of an emergent ray of order p (after $q = p+1$ interaction with the circular cylinder) is given as function of the Fresnel coefficients by

$$\epsilon_{X,p} = \begin{cases} r_X, & p = 0 \\ (1 - r_X^2)(-r_X)^{p-1}, & p \geq 1 \end{cases}, \tag{2.26}$$

where $(1 - r_X^2)$ is due to the fact that all the emergent rays experience two transmissions and $(-r_X)^{p-1}$ is because that the rays of order p suffer $(p-1)$ internal reflections.

The divergence factor can be deduced from the energy balance. According to the geometrical relation of a circular cylinder (Figure 2.8), we have

$$y = a\cos\tau, |dy| = a\sin\tau|d\tau| \tag{2.27}$$

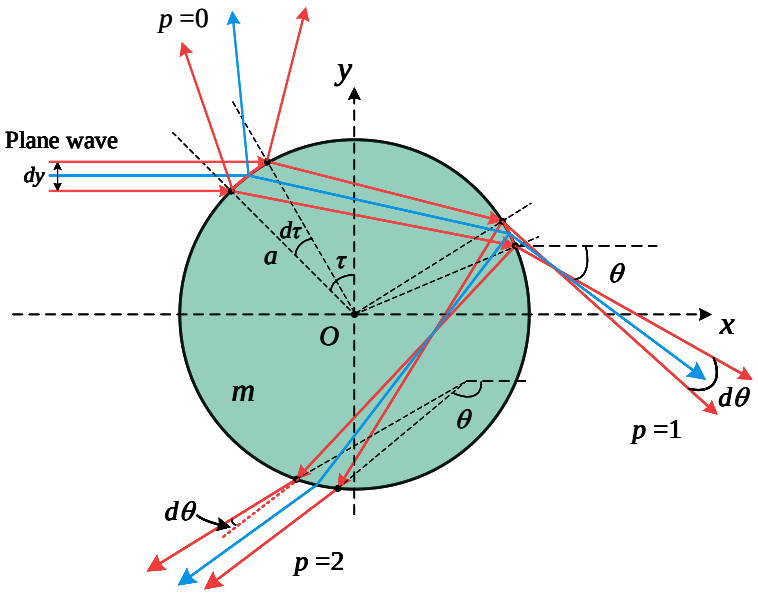

Figure 2.8 – Energy balance of a pencil of rays in a cylinder.

The energy on a surface element $dS_i = dydz = a\sin\tau|d\tau|dz$ is

$$W_i = I_0|dydz| = I_0 a\sin\tau|d\tau dz| \tag{2.28}$$

where I_0 is the intensity of the incident wave at the interaction point. This quantity of energy is emerged, after an attenuation due to the reflection and refraction $\epsilon^2_{X,p}$, into an angle interval $d\theta$ which corresponds to a surface $dS_S = rd\theta dz$ for large r. We note the intensity at r by $I_p(r,\theta)$, then according to energy balance $W_i\epsilon^2_{X,p} = W_S$, we obtain

$$I_0\epsilon^2_{X,p} a\sin\tau|d\tau dz| = I_p(r,\theta) r|d\theta dz| \tag{2.29}$$

and deduce therefore,

$$I_p(r,\theta) = \frac{\epsilon^2_{X,p} I_0 a\sin\tau|d\tau|}{r|d\theta|} = \frac{a}{r} I_0 \epsilon^2_{X,p} D \tag{2.30}$$

where D is called divergence factor given as

$$D = \frac{\sin\tau}{|d\theta/d\tau|} = \frac{\sin\tau}{|d\theta_p/d\tau|} \tag{2.31}$$

According to Eq. (2.24) and Snell's law, we have

$$\frac{d\theta_p}{d\tau} = 2\left(1 - p\frac{\tan\tau}{\tan\tau'}\right) \tag{2.32}$$

Therefore the divergence factor D of a circular cylinder is

$$\mathrm{D} = \frac{m\cos\theta_i\cos\theta_r}{2\left(p\cos\theta_i - m\cos\theta_r\right)} \tag{2.33}$$

The scattered wave being cylindrical in far field, we omit the distance dependent factor kr in Eq. (2.30) as a convention, the scattered intensity of order p is given therefore by

$$\mathrm{I}_p(\theta) = \mathrm{I}_0 ka\mathrm{D}\epsilon_{\mathrm{X},p}^2 \tag{2.34}$$

3. Phase of a ray

The phase of an emergent ray is affected by four factors: the initial phase Φ_i, the phase due to the optical path Φ_P, the Fresnel coefficients Φ_F and the focal lines Φ_f. The total phase Φ_T of a ray is therefore given as

$$\Phi_\mathrm{T} = \Phi_i + \Phi_\mathrm{P} + \Phi_\mathrm{F} + \Phi_f, \tag{2.35}$$

The phase of the incident wave Φ_i is constant for a plane wave and can be omitted.

To calculate the phase due to the optical path, we define the reference ray which arrives at the center of the particle (or a reference point in the particle) in the same direction as the incident ray as if there is no particle and exits in the same direction as the emergent ray (blue lines in Figure 2.9).

For a ray of order $p = 0$, the phase due to the optical path relative to the reference ray (Figure 2.9) is

$$\begin{aligned}\Phi_\mathrm{P} =& -\vec{k}_i\cdot\overrightarrow{\mathrm{OC}} + \vec{k}_0\cdot\overrightarrow{\mathrm{OC}}\\ =& 2ka\sin\tau\end{aligned} \tag{2.36}$$

For a ray of order $p = 1$,

$$\begin{aligned}\Phi_\mathrm{P} =& -\vec{k}_i\cdot\overrightarrow{\mathrm{OC}} + \vec{k}_1\cdot\overrightarrow{\mathrm{OE}} - mk|\mathrm{CE}|\\ =& 2ka(\sin\tau - m\sin\tau')\end{aligned} \tag{2.37}$$

Similarly, a ray of order $p \geq 1$ will have p elements of path $2a\sin\tau'$ inside the

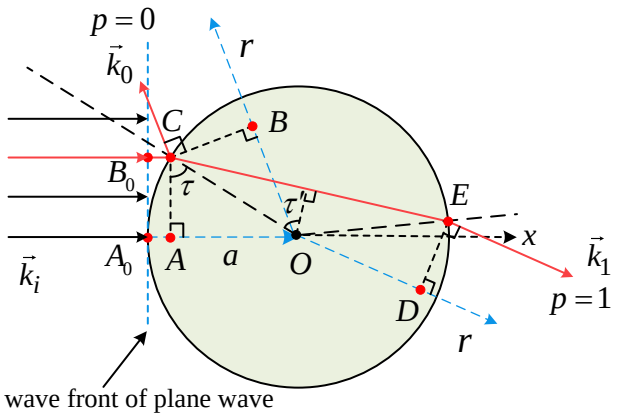

Figure 2.9 – Phase due to the optical path.

particle. We conclude therefore that the phase caused by the optical path of the ray of order p is

$$\Phi_{\mathrm{P}} = 2ka(\sin\tau - pm\sin\tau'), \tag{2.38}$$

The phase shift due to the reflections is evaluated by the Fresnel coefficients Φ_{F} using Eq. (2.16).

Each time, a ray passes a focal line, the phase jumps $\pi/2$. So the phase shift due to the focal lines Φ_f is a count of the focal lines which is given by [4]

$$\Phi_f = \frac{\pi}{2}\left[p - \frac{1}{2}(1-s)\right], \tag{2.39}$$

where s is the sign of $d\theta_p/d\tau$ in Eq. (2.32).

4. Total complex amplitude

Knowing the phase and amplitude of a ray, the complex amplitude of a emergent ray in far field is calculated by

$$\mathrm{E}_{\mathrm{X},p}(\theta) = \sqrt{\frac{\pi}{2}ka\mathrm{D}}|\epsilon_{\mathrm{X},p}|e^{i\Phi_{\mathrm{T}}}, \tag{2.40}$$

where $\pi/2$ is a constant added so that the amplitude calculated by GO is consistent with LMT [119].

The total scattered field $E_X(\theta)$ in direction θ is given as

$$E_X(\theta) = \sum_{p=0}^{\infty} E_{X,p}(\theta) \tag{2.41}$$

However, attention should be paid to the fact that the complex amplitude given in Eq. (2.40) is for the scattering angles determined by the incident ray and the scattering angle of emergent rays are usually irregular, while scattering summation of complex amplitude in Eq. (2.41) must be done for the same angle of different orders. The interpolation is therefore necessary.

The total scattered intensity in the angle θ is given as

$$I_X(\theta) = |E_X(\theta)|^2 \tag{2.42}$$

5. Scattering diagrams

As example, we show in Figures 2.10 and 2.11 the scattering diagrams of an infinite circular cylinder calculated with the GO described in the previous sections for two polarizations. The wavelength of the incident wave is $\lambda = 0.6328$ μm. The radius and the refractive index of the circular cylinder are $a = 100$ μm and $m = 1.333$. The total intensity is calculated with the rays of orders $p = 0$ to 7. The incident plane wave is discretized into 4000 rays. The number of interpolation for scattering angle θ is 4000. In this thesis, the Lagrange polynomials in third order is applied for the interpolation.

We would note firstly that the rays of orders 2 (blue) and 3 (yellow) rebound at 137.92° and 129.11° respectively. These angles correspond to the first and the second order of rainbows predicted by the GO. The rays of the same order near these angles generate the so-called supernumerary bows which will be discussed later.

For the perpendicular polarization (Figure 2.10) we find a strong oscillation around 70° caused by the rays of orders $p = 0$ and 1 since their amplitudes are in the same order of magnitude in this region. The amplitude of the refracted rays is much more important than the other orders in small angle. The oscillations around 120° and in the range from 140° to 180° are also strong which are caused by the rays of the same orders ($p = 2$ or 3) which causes the coarse structure and different orders which generate the high frequency oscillation structure.

In the case of parallel polarization (Figure 2.11), the intensity in the vicinity of the rainbow angles is much weaker than that of the perpendicular polarization. This

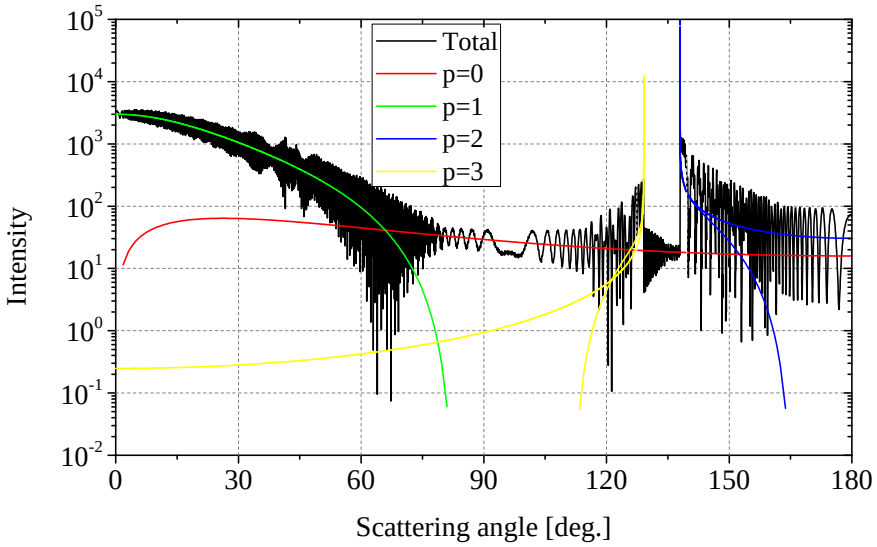

Figure 2.10 – Scattering diagrams of an infinite circular cylinder. The incident plane wave with wavelength $\lambda = 0.6328$ μm is in perpendicular polarization. The radius of particle and its refractive index are $a = 100$ μm and $m = 1.333$.

is because the Fresnel coefficient at those angles for the parallel polarization $\epsilon_{\parallel 2} = 0.059$, $\epsilon_{\parallel 3} = 0.060$ is much smaller than that for the perpendicular polarization $\epsilon_{\perp 2} = 0.296$, $\epsilon_{\perp 3} = 0.188$.

Furthermore, we note also that for parallel polarization (Figure 2.11), the intensity tends to zero near $\theta = 73.78°$ for $p = 0$, $\theta = 138.74°$ for $p = 2$, $\theta = 115°$ for $p = 3$, these correspond to the Brewster angles.

2.1.3 Scattering by a sphere

The scattering of light by spherical particle is the most common subject and the most popular in the interpretations of the natural phenomena, such as the rainbow in the nature.

Because a symmetric plane of a sphere is exactly a circle - the cross section of an infinite circular cylinder, the scattering procedure discussed in the last section is applicable to the scattering of a sphere. Two revisions are, however, to be done. The first concerns the divergence factor and the other is the phase shift due to focal lines.

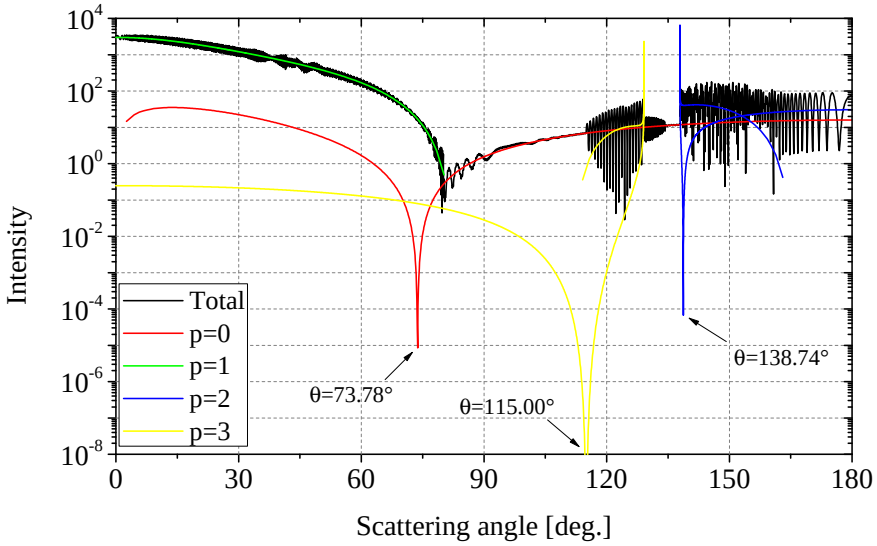

Figure 2.11 – same parameters as Figure 2.10 except for parallel polarization.

1. Divergence factor

Similar to an infinite circular cylinder, the divergence factor of light scattering by a sphere is deduced by the law of energy balance. We consider an incident beam of section dA_i illuminating an area $dA = a^2 \cos\tau d\tau d\phi$ on the sphere. All the flux in the beam, after interaction with the particle, spreads into a solid angle $d\Omega$ which intersects a sphere of radius r of surface $dA_s = r^2 d\Omega = r^2 \sin\theta d\theta d\phi$ in far distance r from the sphere. According to the balance of energy, the scattered intensity $I_p(r,\theta)$ of order p at r is related to the intensity of the incident wave I_0 by the relation $I_p(r,\theta) r^2 \sin\theta d\theta d\phi = I_0 \epsilon_{X,p}^2 a^2 \sin\tau\cos\tau d\tau d\phi$. We deduce therefore,

$$I_p(r,\theta) = \frac{\epsilon_{X,p}^2 I_0 a^2 \sin\tau\cos\tau d\tau d\phi}{r^2 \sin\theta d\theta d\phi} = \frac{a^2}{r^2} I_0 \epsilon_{X,p}^2 D \tag{2.43}$$

where D is the divergence factor of a spherical particle defined by

$$D = \frac{\sin\tau\cos\tau}{\sin\theta |d\theta/d\tau|}, \tag{2.44}$$

The derivative $d\theta/d\tau$ is the same as for a circular cylinder (Eq. (2.32)). The divergence factor of order p can be written in terms of incident and refraction angle as follows

$$D = \left| \frac{\sin(2\theta_i)}{4\sin\theta\left(p\frac{\tan\theta_r}{\tan\theta_i} - 1\right)} \right| = \left| \frac{\sin(2\theta_i)}{4\sin\theta\left(p\frac{\cos\theta_i}{m\cos\theta_r} - 1\right)} \right|. \tag{2.45}$$

The scattered wave being spherical in far field, we omit the distance dependent factor $(kr)^2$ in Eq. (2.43) as a convention, the scattered intensity of order p is given therefore by

$$\mathrm{I}_p(\theta) = \mathrm{I}_0(ka)^2 \mathrm{D}\epsilon_{\mathrm{X},p}^2 \tag{2.46}$$

2. Phase shift due to focal lines

In the scattering of a wave by a spherical particle, the light rays may cross in the direction perpendicular to the scattering plane. Therefore, there is a set of focal lines supplementary to the case of the scattering by a circular cylinder [4]. The phase shift due to the first set of focal lines Φ_{f2} is the same as for the circular cylinder Eq. (2.39). The phase shift due to the the second set is given as

$$\Phi_{f1} = \frac{\pi}{2}\left[-2k_p + \frac{1}{2}\left(1 - q_p\right)\right]. \tag{2.47}$$

where k_p and q_p are given in Eq. (2.25). So, the total phase shift due to the focal lines for a spherical particle is

$$\Phi_f = \Phi_{f1} + \Phi_{f2}. \tag{2.48}$$

3. Total complex amplitude

Knowing the scattering intensity in far field (Eq. 2.46) and the total phase of the emergent ray, we get the complex amplitude of the scattered field of a sphere as

$$\mathrm{E}_{\mathrm{X},p}(\theta) = ka\sqrt{\mathrm{D}}|\epsilon_{\mathrm{X},p}|\exp(i\Phi_{\mathrm{T}}) \tag{2.49}$$

The amplitude factor due to the reflection and refraction $\epsilon_{\mathrm{X},p}$ is the same as for a cylinder (Eq. 2.26). The formula for the total phase is also the same as for the cylinder but the phase shift due to the focal lines are to be calculated by Eq. (2.48).

4. Scattering diagrams

We compare now the scattering diagrams of a infinite circular cylinder and a sphere calculated by the GO for the perpendicular and parallel polarizations in Figures 2.12 and 2.13. We find first that the scattered intensity in the forward direction of the sphere is about three orders stronger than that of the cylinder. This is because that the scattered intensity of a sphere is proportional to $(ka)^2$ while that of

a cylinder is proportional to ka. For the cases of scattering shown in these Figures $ka = 2\pi a/\lambda \simeq 1000$. This ratio decreases as function of the scattering angle from about 1000 at 00° to about 500 at 90°. This can be understood by the transversal divergence effect of the spherical particle. Otherwise, the profiles of the scattering diagrams of a sphere are similar to those of a circular cylinder. Some other differences, such as the intensities around 100° for perpendicular polarization, and in backward direction are due probably to the phase shift of focal lines and divergence factor.

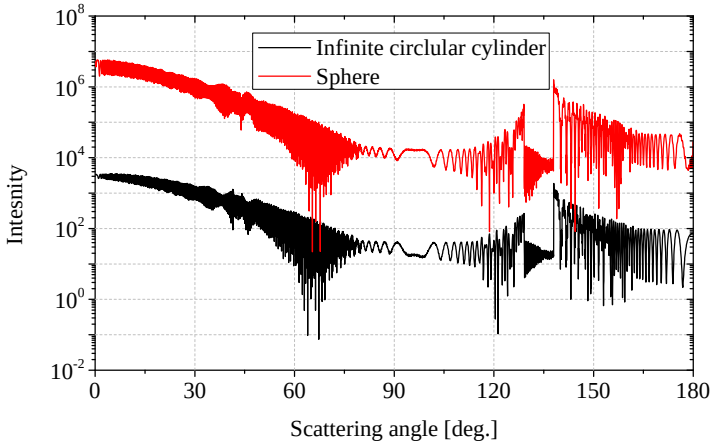

Figure 2.12 – Comparison the scattering diagrams of a sphere and infinite circular cylinder. The incident plane wave with wavelength $\lambda = 0.6328$ μm is in perpendicular polarization. The radius of particle and its refractive index are $a = 100$ μm and $m = 1.333$.

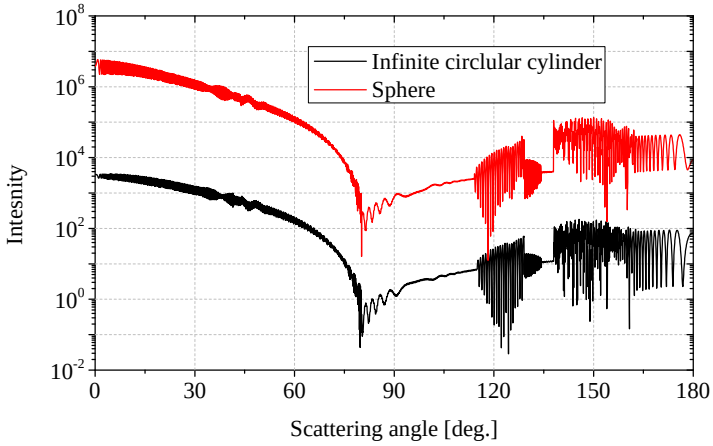

Figure 2.13 – The parameters are the same as in Figure 2.12 except for parallel polarization.

In Figure 2.12 and 2.13, we find their scattering diagrams have similarly trends on the whole, but there is a clear difference in intensity which is caused by their

different divergence factors.

2.2 Physical optics

The ray model of the GO described in the preceding section deals with only the rays which interact with the particle, but not the rays passing by the particle surface. The light represented by these rays play an important rule in the scattering in forward direction. On the other hand, we have seen that the intensity in the vicinity of rainbow angle predicted by the GO is not continuous. These are the intrinsic flaws of the ray model and can be remedied by the physical optics.

2.2.1 Huygens-Fresnel Principle

The physical optics is an approximate method to take into account the wave effect of light. In this thesis, especially for the two problems mentioned above, the Huygens-Fresnel principle [120] is sufficient.

Suppose that the complex amplitude E(P) at any point P on the surface Σ is known (Figure 2.14). The complex field $E(P_0)$ at an observation point P_0 is, according to the Huygens-Fresnel principle, the contribution all the points on the surface Σ, i.e.

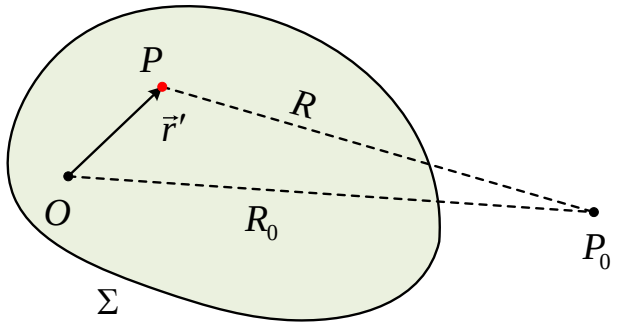

Figure 2.14 – Schema for the Huygens-Fresnel principle.

$$\mathrm{E}(\mathrm{P}_0) = \frac{i}{\lambda}\iint_{\Sigma} \mathrm{E}(\mathrm{P})\frac{\exp(-ik\mathrm{R})}{\mathrm{R}}\cos(\hat{n},\hat{k}_s)\,d\mathrm{S} \tag{2.50}$$

where λ is the wavelength. R is the distance from point P to P_0. R_0 is the distance

between the reference point O to P_0, $\hat{n}$ is the normal of the surface Σ at point P, $\hat{k}_s$ is the unit vector from point P to P_0.

If the point P_0 is in far field of the surface Σ, we have

$$\frac{\exp(-ikR)}{R} \approx \frac{\exp(-ikR_0)}{R_0} \exp(ik\hat{k}_s \cdot \vec{r}'), \tag{2.51}$$

Furthermore, if $\cos(\hat{n}, \hat{k}_s) \approx 1$, Eq. (2.50) is rewritten as

$$E(P_0) = \frac{i \exp(-ikR_0)}{\lambda R_0} \iint_\Sigma E(P) \exp\left(-ik\hat{k}_s \vec{r}'\right) dS \tag{2.52}$$

In the light scattering of small particles, the Huygens principle is often used with Babinet's principle [21, 119] to deal with the forward diffraction. For the light scattering of an infinite circular cylinder, the diffraction field in the forward direction is similar to that of a slit of the width equal to the diameter of the cylinder and given by [50]

$$E_d(\theta) = \frac{1+\cos\theta}{2} \frac{\sin(ka\sin\theta)}{\sin\theta} \exp\left(i\frac{3\pi}{2}\right) \tag{2.53}$$

where the factor $(1+\cos\theta)/2$ is for a non-polarized wave and the phase $3\pi/2$ is added for the field to be in consistence with that of the Mie theory.

For a spherical particle, the diffraction field in the forward direction is given as [28, 121]

$$E_d(\theta) = \frac{(ka)^2 J_1(ka\sin\theta)}{ka\theta} \tag{2.54}$$

where $J_1(\cdot)$ is the Bessel function of the first kind of order 1.

Therefore, the total scattered field by consideration of the forward difraction is

$$E_X(\theta) = \sum_{p=0}^{\infty} E_{X,p}(\theta) + E_d(\theta) \tag{2.55}$$

where $E_{X,p}$ corresponds to the scattered field calculated by the GO in the precedent section for a cylinder or a sphere.

2.2.2 Comparison the scattering diagrams of a spherical particle with rigorous theories

Now we will compare the scattering diagrams of a spherical particle calculated by the GO revised with PO to those of the Mie theory and Debye theory, for two pur-

poses: evaluation of the precision of the approximate methods (GO+PO) and observation of the points to be improved.

We compare first in Figure 2.15 the scattering diagrams calculated by the Mie theory and by the GO+PO for the perpendicular polarization. The agreement is very good in general. We observe, however, significant difference in the rainbow regions. This is due to the intrinsic default of the ray model [3]. The scattering diagrams

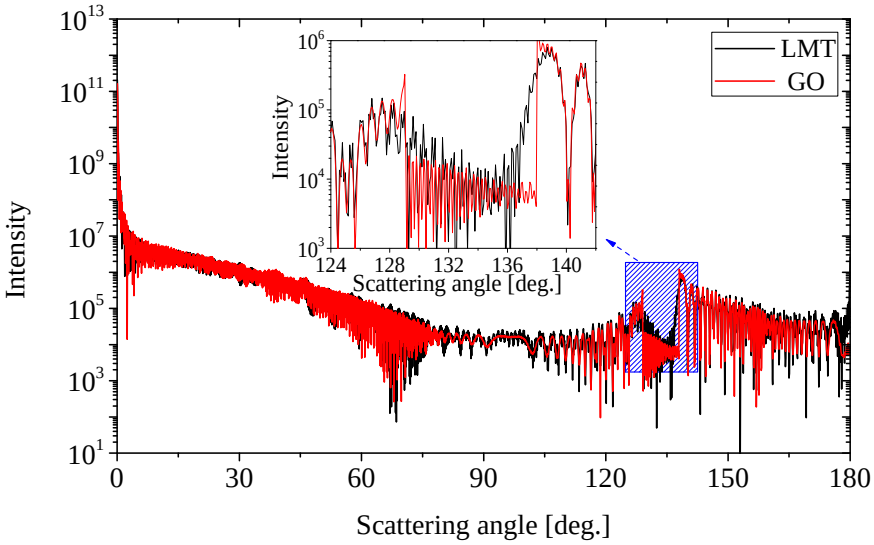

Figure 2.15 – Comparison the scattering diagrams of a sphere between LMT and GO in perpendicular polarization. The forward diffraction is also included here. The incident plane wave with wavelength $\lambda = 0.6328$ µm is in perpendicular polarization. The radius of particle and its refractive index are $a = 100$ µm and $m = 1.333$.

for parallel polarization calculated with the same methods for the same particle are compared in Figure 2.16. To examine in details the problem of scattering in the rainbow regions, we zoom the scattering diagrams in the range from 124° to 142°. We find, both for perpendicular and parallel polarization, GO and Mie theory are matched very well except for the Alexander zone (the region between primary rainbow and secondary rainbows). Apart from the rainbow regions, we observe also a clear difference near the region 71° – 116° between LMT and GO. It is probably caused by Brewster angles of $p = 0$ and $p = 3$ and abrupt end rays of $p = 1$ and $p = 3$ (see Figure 2.11), this problem being beyond the study of this thesis.

The GO permits to isolate the contributions of different orders. To illustrate scattering near rainbow angles, we compare of the GO and Debye theory in Figures 2.17 and 2.18 by considering only the contributions of the rays of orders $p = 2,3$. The Debye theory is a rigorous method that can also isolate the contributions of different

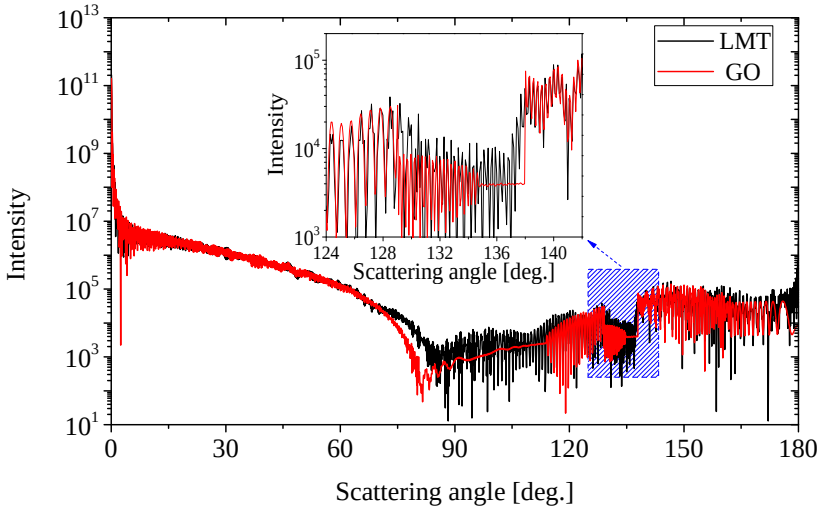

Figure 2.16 – The parameters are the same as in Figure 2.15 except for parallel polarization.

orders [65]. The difference is significant only in the vicinity of the GO rainbow angles and in the Alexander zone. Out of this region, the GO gives very precise results. Airy proposed a method to solve this problem [3], which works very well in in the vicinity of the GO rainbow angles and in the Alexander zone, but not as well out of this region. Airy theory will be revisited in Chapter 4.

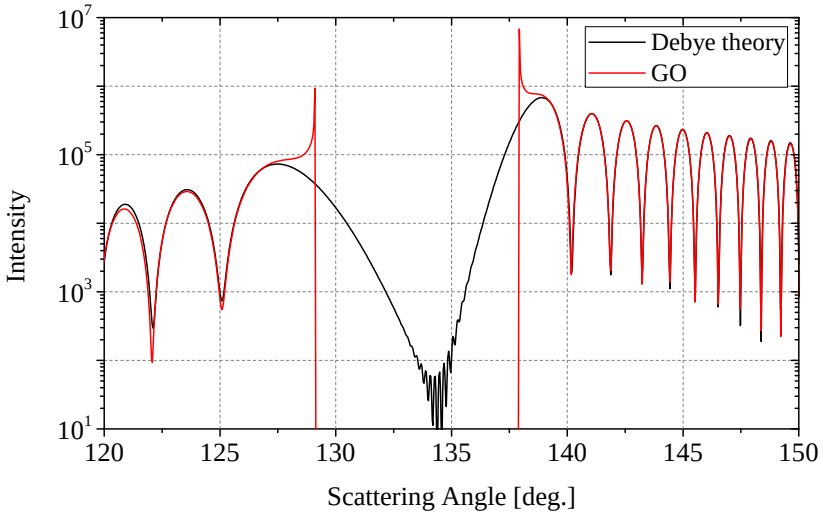

Figure 2.17 – Scattering diagrams of $p = 2$ and $p = 3$ for a sphere in perpendicular polarization by Debye theory and GO. The incident plane wave with wavelength $\lambda = 0.6328$ μm is in perpendicular polarization. The radius of particle and its refractive index are $a = 100$ μm and $m = 1.333$.

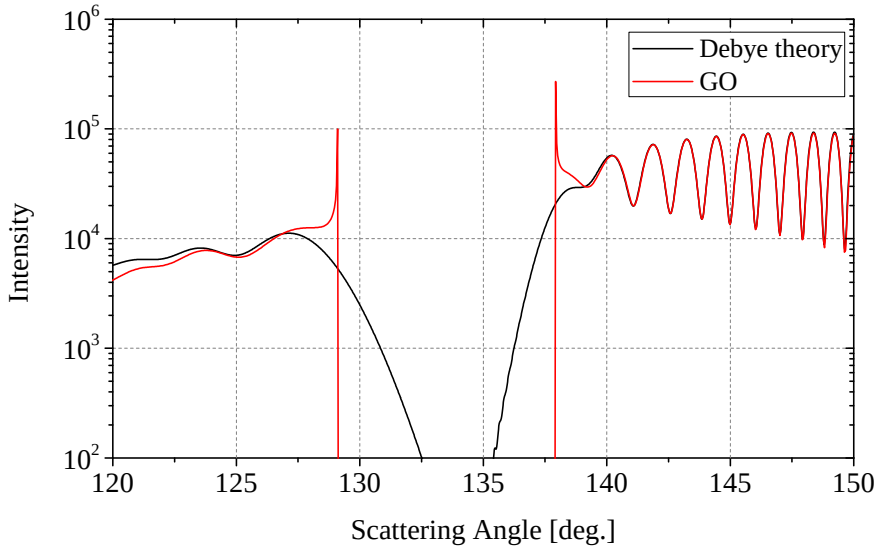

Figure 2.18 – Same parameters as Figure 2.17 except for parallel polarization.

2.3 Summary

The fundamental concepts and laws of the geometrical optics (GO) and the physical (PO) are introduced from the point view of their application to the light scattering by particles. Then, the scattering of plane wave by an infinite circular cylinder and a sphere is taken as examples to illustrate the applicability and the limitations of these two approximate models. By comparison of the scattering patterns with the rigorous Lorenz-Mie theory, it is shown that GO permits to calculate the amplitude and the phase of all the emergent rays in far field but it fails in prediction of the scattering in forward direction and near the rainbow angles. PO can remedy the scattering in the forward direction by considering the particle as a disk but the rectification of the scattering near the rainbow angles has been an arduous topic since a long time. The essential concepts presented in this chapter serve as a base to the understanding of the Vectorial Complex Ray Models and its application in the following chapters.

Chapter 3

Vectorial complex ray model for light scattering

The geometrical optics (GO) for light scattering described in the previous Chapter can only be applied to the spherical particles and the infinite circular cylinders, because in these special cases, the direction, the amplitude and the phase of all the emergent rays can be given in analytical form. If a particle has not such circular symmetry, it will be very difficult, as for a ellipsoidal particle [32, 33], or impossible (for a particle of arbitrary shape). To deal with this problem, the Vectorial Complex Ray Model (VCRM) has been developed.

We will present in this Chapter the fundamentals of the VCRM and apply it to the scattering of a infinite elliptical cylinder and an ellipsoidal particle. In the case of the scattering by an elliptical cylinder, we will limit ourselves to the normal incidence and we observe the scattering in the plane perpendicular to the cylinder axis, so call VCRM2D, since this is a pure 2D scattering problem. For the scattering of an ellipsoidal particle, only the scattering in a symmetric plane will be considered. This will be called VCRM2D+ because the curvature of the ellipsoid in the direction perpendicular to the symmetric plane is taken into account. In both cases, the incident wave will be a plane wave.

3.1 Fundamentals of VCRM

In the GO, a ray is characterized with four properties (as seen in the last Chapter): the direction, the amplitude, the phase and the polarization. In the VCRM [53], a new property of the *wavefront curvature* is introduced, which describes the curva-

ture property of the wavefront of the wave that the ray represents at the considered point. The variation of the amplitude of the wave along a ray is calculated directly with the wavefront curvature. And the phase due to the focal lines is just a count of the number of the sign changes of the wavefront curvature radii. In this section we will explain how to calculate the wavefront curvature when a ray is refracted or reflected by the particle interface or propagates from one point to the other in the same medium, and how to deduce the variation of the amplitude from the the wavefront curvature radii. All these will be applied to the calculation of the scattering diagrams of an infinite elliptical cylinder and an ellipsoidal particle.

3.1.1 Convention of the sign of curvature radii

In the point view of differential geometry, the curvature property of any smooth surface can be described by a 2×2 curvature matrix in a given base and the matrix is diagonal if the base are the two principal directions. In the latter case, the two diagonal elements of the matrix are the principal curvatures (κ_1, κ_2) of the surface and their inverse values are the principal curvature radii. A surface can be convex or concave, so the values of the curvatures (or principal radii) may be positive or negative. In the VCRM we adopte following convention: *Along the propagation direction of a ray, if the curvature center of the surface locates after the incident point, the sign of curvature radius is positive, otherwise, it is negative.* This convention will be applied to both the curvature of the wavefront and the curvature of the particle surface.

Ti illustrate the convention mentioned above, we consider a light ray (red in Figure 3.1 which represent the propagation of a plane wave impinging on a particle surface. The two principal curvatures (κ_1, κ_2) of the wavefront are zero and the curvature radii (R_1, R_2) are infinity. The curvature radius ρ_a of the particle surface at point A in the plane xy is positive since its curvature center O_a is after the interaction point. The curvature radius R_a of the wavefront of the refracted wave at A in the xy plane is also positive because its curvature center F is after the point A. Similarly, the curvature radii of the particle surface ρ_b and the wavefront R_b at point B are both negative. The wavefront curvatures (or curvature radii) change the sign form A to B, so there is a focal line between the two points. Consequently, the calculation of the phase shift due to the focal lines is just a matter of counting the number of the sign changes of the wavefront curvature. If the wavefront curvatures (or curvature radii)

change N_f times of sign from the first interaction point to the observation point, the total phase shift due to the focal lines Φ_f is given as

$$\Phi_f = \frac{\pi}{2} N_f \tag{3.1}$$

The refracted wave at point B in the Figure is divergent, so its wavefront curvature radius is negative and there is not focal line outside of the particle. If the curvature radius of the emergent wave is positive, there will be a supplementary phase shift from the emergent point to the infity.

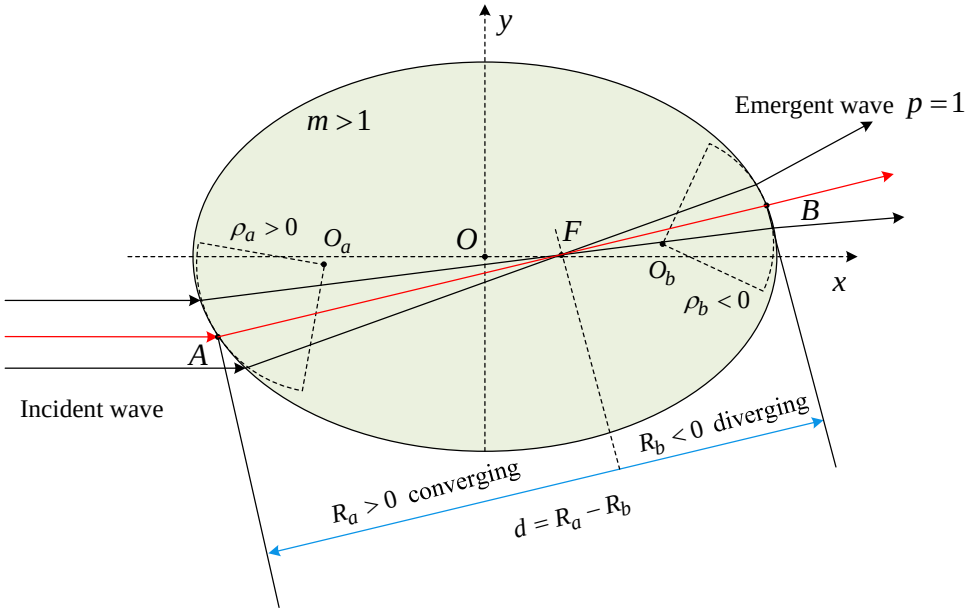

Figure 3.1 – Convention the sign of curvature radii.

The wavefront curvature radii at two successive interaction points are related by the distance between them

$$R_b = R_a - d$$

3.1.2 Wavefront equation

As mentioned above, we are only interested in the scattering in a symmetric plane. In this case, one of the principal directions is always in the symmetric plane and the other is perpendicular to the this plane. The wavefront equation in matrix form [53, 54] is simplified into two scalar equations. The relationship between the curvature radii of the particle, the incident wavefront and the refraction wavefront are given

as

$$\frac{k_r}{\mathrm{R}'_1} = \frac{k_i}{\mathrm{R}_1} + \frac{k_{rn} - k_{in}}{\rho_1} \tag{3.2}$$

$$\frac{k_{rn}^2}{k_r \mathrm{R}'_2} = \frac{k_{in}^2}{k_i \mathrm{R}_2} + \frac{k_{rn} - k_{in}}{\rho_2} \tag{3.3}$$

where k_r and k_i are the wave numbers of the refracted and the incident waves. R'_ν and R_ν are the principal wavefront curvature radii of the refracted and incident wave, the subscripts $\nu = 1$ and 2 denote respectively the plane in the incident plane and that perpendicular to the incident plane. The ρ_ν is the curvature radius of the particle surface in the plane ν. The wavefront equations (3.2) and (3.3) are also applicable to the reflected wave [53] by taking $k_r = k_i$ and $k_{rn} = -k_{in}$.

For the scattering by a infinite cylinder illuminated perpendicularly by a plane wave, only Eq. (3.3) is necessary.

3.1.3 Divergence factor

When a wave propagates, its amplitude decreases or increases along the optical path according to its convergence or divergence. This property can be described by the so called divergence factor D. We will derivate the relation of the amplitudes between two points by the energy balance in a bundle of rays and then generalize it to obtain the definition of the divergence factor in the VCRM.

Bundle of rays in 2D

A bundle of rays in a 2D wave is shown in Figure 3.2. Suppose that the intensity on the wavefront $\mathrm{A_1A_2A_3A_4}$ is I_i and that on the wavefront $\mathrm{B_1B_2B_3B_4}$ is I_e. R_i and R_e represent the value of their curvature radii of the wavefront. The superscript e or i stands for the emergent or the incident wave. According to the energy balance, we have

$$\mathrm{I}_i \mathrm{R}_i h d\theta = \mathrm{I}_e \mathrm{R}_e h d\theta \tag{3.4}$$

where h is the height of the elements. It is ready to deduce that the amplitudes of the wave at the two points are related by

$$\frac{\mathrm{E}_e}{\mathrm{E}_i} = \sqrt{\frac{\mathrm{I}_e}{\mathrm{I}_i}} = \sqrt{\left|\frac{\mathrm{R}_i}{\mathrm{R}_e}\right|} \tag{3.5}$$

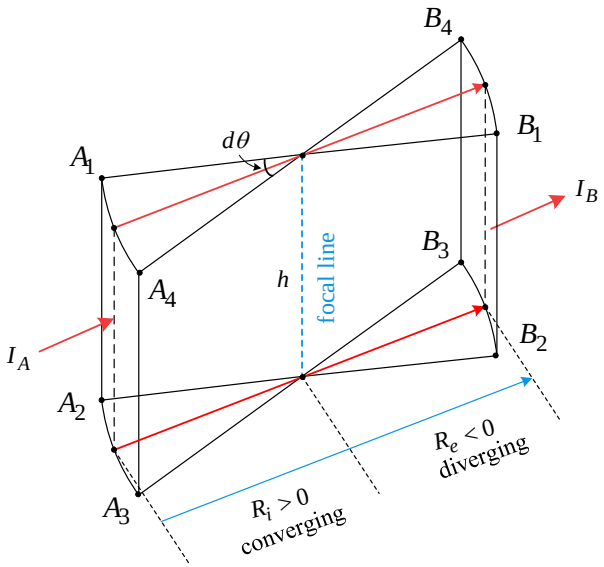

Figure 3.2 – Ray model in a homogeneous medium for 2D.

Bundle of rays in 3D

Figure 3.3 shows a bundle of rays in 3D. f_1 and f_2 are two focal lines in the perpendicular and parallel planes. Same as in 2D problems, according to the energy balance, the energy flux crosses area of $S(A) = |d\alpha_1 R_{1,i} d\alpha_2 R_{2,i}|$ and $S(B) = |d\alpha_1 R_{1,e} d\alpha_2 R_{2,e}|$ are equal. So, $I_A S(A) = I_B S(B)$, this is rewritten as,

$$\frac{I_B}{I_A} = \left| \frac{R_{1,i} R_{2,i}}{R_{1,e} R_{2,e}} \right| \tag{3.6}$$

where I_A and I_B are the intensity on the surfaces $S(A)$ and $S(B)$ respectively.

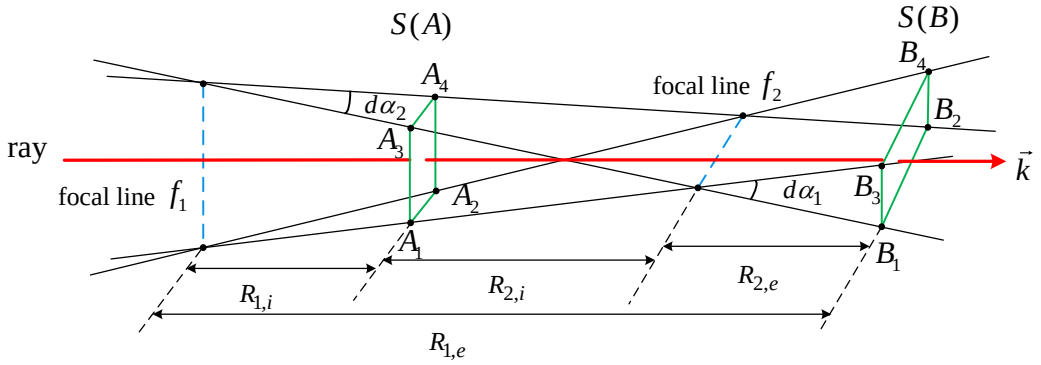

Figure 3.3 – Ray model in a homogeneous medium for 3D.

Therefore, the relationship of the amplitudes at two points A and B is given as

$$\frac{\mathrm{E}_e}{\mathrm{E}_i} = \sqrt{\left|\frac{\mathrm{R}_{1,i}\mathrm{R}_{2,i}}{\mathrm{R}_{1,e}\mathrm{R}_{2,e}}\right|} \tag{3.7}$$

In the light scattering by a particle, a ray interacts successively with the particle surface, we can apply the relation Eq. (3.7) repeatedly and define the divergence factor as the ratio of the intensity of the emergent wave to that of the incident one.

As an example, we show in Figure (3.4) the trajectory of a ray in a symmetric plane of a particle. The curvature radius of the wavefront of the reflected wave $p = 0$ in the scattering plane at point A is noted by $\mathrm{R}^e_{2,1}$ (the curvature radius in the perpendicular plane $\mathrm{R}^e_{1,1}$ is omitted for clarity). The curvature radius of the emergent ray at a distance d from A is $\mathrm{R}^e_{2,1} - d$. So the divergence factor of the reflected ray is $\mathrm{D}_{2,d} = \left|\frac{\mathrm{R}^e_{2,1}}{\mathrm{R}^e_{2,1}-d}\right|$.

The curvature radius of the wavefront of the refracted wave at point A is noted by $\mathrm{R}'_{2,1}$. The distant from point A to the next interaction point B is d_{12}. The curvature radius of the incident wave at point B is then $\mathrm{R}_{2,2} = \mathrm{R}'_{2,1} - d_{12}$. The ratio of the intensity between the two points due to the variation of the curvature radii is then $\left|\frac{\mathrm{R}^e_{2,1}}{\mathrm{R}'_{2,1}-d_{12}}\right|$. The curvature radius of the wavefront of the first refracted wave $p = 1$ is noted by $\mathrm{R}^e_{2,2}$. The divergence factor of the emergent ray $p = 1$ at an observation distance d from B is calculated therefore by $\mathrm{D}_{2,d} = \left|\frac{\mathrm{R}'_{2,1}}{\mathrm{R}_{2,2}}\frac{\mathrm{R}^e_{2,2}}{\mathrm{R}^e_{2,2}-d}\right|$.

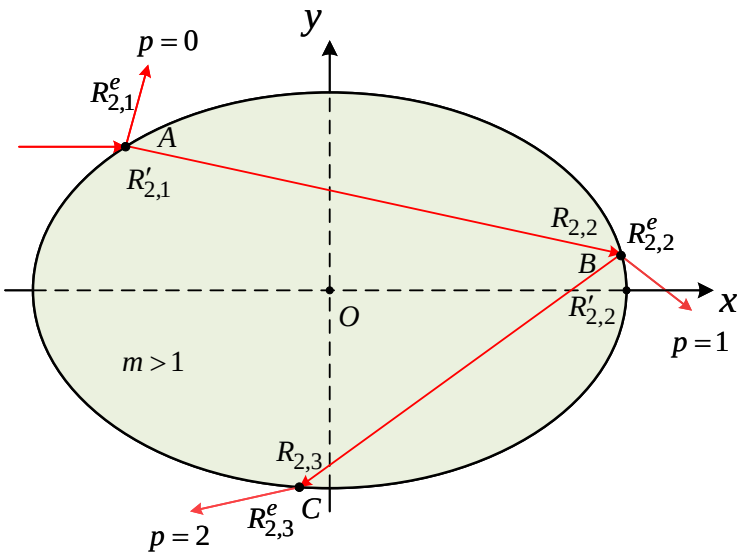

Figure 3.4 – Divergence factor in an elliptical cylinder.

We can continue this procedure to any order p and apply the same principle to the divergence factor due to the variation of the curvature radii in the direction perpendicular to the scattering plane. The divergence factor D_d is given as

$$\mathrm{D}_d = \left| \frac{\mathrm{R}'_{1,1}\mathrm{R}'_{2,1}}{\mathrm{R}_{1,2}\mathrm{R}_{2,2}} \cdot \frac{\mathrm{R}'_{1,2}\mathrm{R}'_{2,2}}{\mathrm{R}_{1,3}\mathrm{R}_{2,3}} \cdots \frac{\mathrm{R}'_{1,p}\mathrm{R}'_{2,p}}{\mathrm{R}_{1,q}\mathrm{R}_{2,q}} \cdot \frac{\mathrm{R}^e_{1,q}\mathrm{R}^e_{2,q}}{(\mathrm{R}^e_{1,q}-d)(\mathrm{R}^e_{2,q}-d)} \right| \tag{3.8}$$

where $q = p+1$ is the number of interactions of the ray with the particle surface. The relation between the wavefront curvature radii $\mathrm{R}'_{\mathrm{v},q}$ and $\mathrm{R}_{\mathrm{v},q+1}$ of two successive interaction points is given as their distance $d_{q,q+1}$

$$\mathrm{R}_{\mathrm{v},q+1} = \mathrm{R}'_{\mathrm{v},q} - d_{q,q+1} \tag{3.9}$$

In fact, Eq. (3.8) is valid for the interaction of a ray with a particle of any shape whether the ray trajectory remains in the same plane or not since only the curvature radii of the wavefront between two successive points intervene step by step (see Figure 3.3 and Eq. (3.7)).

Complex amplitude

In far field, the distance $d \approx r \to \infty$. The intensity of an emergent ray can be written as

$$\mathrm{I}_{\mathrm{X},p} = \frac{|\mathrm{E}_{\mathrm{X},p}|^2}{(kr)^2} \tag{3.10}$$

By consideration of the Fresnel factor $\epsilon_{\mathrm{X},p}$ and the phase of the ray, omitting the spherical wave factor $1/(kr)^2$ as the convention, the complex amplitude of the ray is given as

$$\mathrm{E}_{\mathrm{X},p} = k\sqrt{\mathcal{D}_p}|\epsilon_{\mathrm{X},p}|\exp(i\Phi_{\mathrm{T}}) \tag{3.11}$$

where $\epsilon_{\mathrm{X},p}$ is Fresnel factor given as

$$\epsilon_{\mathrm{X},p} = \begin{cases} r_{\mathrm{X},0}, & p = 0 \\ t_{\mathrm{X},0}\, t_{\mathrm{X},p} \prod_{j=1}^{p-1} r_{\mathrm{X},j}, & p \geq 1 \end{cases}, \tag{3.12}$$

$t_{\mathrm{X},0}$ and $t_{\mathrm{X},p}$ are the Fresnel transmission coefficients at the incident point and emergent point, $r_{\mathrm{X},j}$ the Fresnel reflection coefficient at j^{th} internal reflection. In the case of spherical particle, $t_{\mathrm{X},0} = t_{\mathrm{X},p}$ and $r_{\mathrm{X},j}$ is a constant. Eq. (3.12) is simplied to the equation given in the Chapter 2.

$\mathcal{D}_p$ is given as

$$\mathcal{D}_p = \lim_{r\to\infty}(r^2 \mathrm{D}_r) = \left|\frac{\mathrm{R}'_{11}\mathrm{R}'_{21}}{\mathrm{R}_{12}\mathrm{R}_{22}} \cdot \frac{\mathrm{R}'_{12}\mathrm{R}'_{22}}{\mathrm{R}_{13}\mathrm{R}_{23}} \cdots \frac{\mathrm{R}_{1p}\mathrm{R}'_{2p}}{\mathrm{R}_{1q}\mathrm{R}_{2q}} \cdot \mathrm{R}^e_{1q}\mathrm{R}^e_{2q}\right| \tag{3.13}$$

Notice, in the case of a sphere, the complex amplitude Eq. (3.11) is the same as Eq. (2.49). This will be proved in Appendix C.

For the 2D scattering, such as the scattering of an infinite elliptical cylinder, only the divergence in the symmetric plane is considered. The divergence factor is simplified to

$$\mathrm{D}_d = \left|\frac{\mathrm{R}'_{2,1}}{\mathrm{R}_{2,2}} \cdot \frac{\mathrm{R}'_{2,2}}{\mathrm{R}_{2,3}} \cdots \frac{\mathrm{R}'_{2,p}}{\mathrm{R}_{2,q}} \cdot \frac{\mathrm{R}^e_{2,q}}{\mathrm{R}^e_{2,q} - d}\right| \tag{3.14}$$

So, the complex amplitude in VCRM2D is given as

$$\mathrm{E}_{\mathrm{X},p} = |\epsilon_{\mathrm{X},p}|\sqrt{\frac{\pi}{2}k\mathcal{D}_p}\exp(i\Phi_\mathrm{T}) \tag{3.15}$$

where $\mathcal{D}_{2,p}$

$$\mathcal{D}_p = \lim_{r\to\infty}(r\mathcal{D}_{2,r}) = \left|\frac{\mathrm{R}'_{21}}{\mathrm{R}_{22}} \cdot \frac{\mathrm{R}'_{22}}{\mathrm{R}_{23}} \cdots \frac{\mathrm{R}'_{2p}}{\mathrm{R}_{2q}} \cdot \mathrm{R}^e_{2q}\right| \tag{3.16}$$

The presence of the factor $\pi/2$ in Eq. (3.15) has been explained in Chapter 2, see also [119].

The total phase Φ_T is given in the same form as in the GO (Eq. (2.35)), but the calculation of all the terms are not the same. The initial phase Φ_i depends only on the incident wave, so independent of the particle. But the phase shift of the Fresnel coefficients Φ_F must be calculated step by step, especially the total reflection may occurs in a non-spherical particle. The phase shift of the focal lines Φ_f is just a count of the number of the sign changes of the curvature radii in VCRM (Eq. (3.1)). The phase of the optical path Φ_P is also to be calculated step by step since the optical path between two successive interaction points changes each time in a non-spherical particle.

3.2 VCRM for an infinite elliptical cylinder and an ellipsoid

In this section, we will apply the VCRM to the study of the scattering of a plane wave by an infinite elliptical cylinder and an ellipsoidal particle.

3.2.1 Description of the particle surface

An infinite elliptical cylinder:

The cross section of an infinite elliptical cylinder is described by

$$\frac{x^2}{a^2}+\frac{y^2}{b^2}=1 \tag{3.17}$$

where a and b are the semi-axes along x and y respectively.

The unit normal vector $\hat{n}$ and the unit tangent vector $\hat{\tau}$ at a given point (x,y) on the particle surface are given as

$$\hat{n} = (n_x,n_y)=\left(\frac{b^2x}{\sqrt{b^4x^2+a^4y^2}},\frac{a^2y}{\sqrt{b^4x^2+a^4y^2}}\right) \tag{3.18}$$

$$\hat{\tau} = (\tau_x,\tau_y)=(-n_y,n_x) \tag{3.19}$$

In the calculation, $-\hat{n}$ will be used for the first incident point, so that the wave vector $\vec{k}$ makes an acete angle with the normal of the particle surface.

The curvature radius ρ of the particle surface is

$$\rho=a^2b^2\left(\frac{x^2}{a^4}+\frac{y^2}{b^4}\right)^{\frac{3}{2}} \tag{3.20}$$

Eqs. (3.18) - (3.20) are applicable to any interaction point of a ray with the particle surface.

An ellipsoid:

The surface of an ellipsoid is described by

$$\frac{x^2}{a^2}+\frac{y^2}{b^2}+\frac{z^2}{c^2}=1 \tag{3.21}$$

We consider the scattering in the xy plane (so $z = 0$). The coordinates of the incident points (x_i, y_i), the unit normal vector $\hat{n}$, the unit tangent vector $\hat{\tau}$ are all the same as for an infinite elliptical cylinder. But we have now two curvature radii, one is in the symmetrical plane and the other in the perpendicular direction. The two principal curvature radiis of an ellipsoidal particle surface ρ_1 and ρ_2 at point (x_i, y_i) are

$$\rho_1 = \frac{c^2}{a}\left[1 + (a^2/b^2 - 1)\, y_i^2/b^2\right]^{1/2} \tag{3.22}$$

$$\rho_2 = \frac{b^2}{a}\left[1 + (a^2/b^2 - 1)\, y_i^2/b^2\right]^{3/2} \tag{3.23}$$

3.2.2 Ray tracing

We present now the ray tracing procedure in the framework of the VCRM and the calculations of all the properties of the emergent rays. Since the cross section of an infinite elliptical cylinder is the same as the symmetric plane of an ellipsoid of the same axes. The ray tracing process for the two particles are the same except the calculation of the curvature radii in the perpendicular direction of an ellipsoid.

Interaction of rays with particle surface

We suppose that the incident plane wave propagates along x axis and is discretized as N equal distant rays along y axis. The coordinates of the incident points on the particle surface are

$$(x_i, y_i) = \left(-a\sqrt{1 - (y_i/b)^2}, (2t+1)b/\mathrm{N} - b\right) \tag{3.24}$$

where $t = 0, 1, 2 \ldots (\mathrm{N} - 1)$.

The incident wave vector can be projected in two bases (Figure 3.5):

In the base $(\hat{n}, \hat{\tau})$:

$$\vec{k}_i = k_{in}\hat{n} + k_{i\tau}\hat{\tau} \tag{3.25}$$

where $k_{in} = \vec{k}_i \cdot \hat{n}$ and $k_{i\tau} = \vec{k}_i \cdot \hat{\tau}$. According to the Snell laws ($k_{i\tau} = k_{l\tau} = k_{r\tau}$), the wave vectors of the reflected ray and the refracted ray are

$$\vec{k}_l = -k_{in}\hat{n} + k_{i\tau}\hat{\tau} \tag{3.26}$$

$$\vec{k}_r = k_{rn}\hat{n} + k_{i\tau}\hat{\tau} \tag{3.27}$$

where $k_{rn} = \sqrt{k_r^2 - k_{i\tau}^2}$. These components are used to determine the directions of the reflected and refracted rays, and to calculate the Fresnel coefficients at each interaction point.

The refracted ray at the first interaction point is the incident ray of the second interaction point (Figure (3.5)), and the reflected ray at the second point is the incident ray of the next point, etc. So we can use Eqs. (3.26) and (3.27) repeatedly to determine the wave vectors of all the emergent rays.

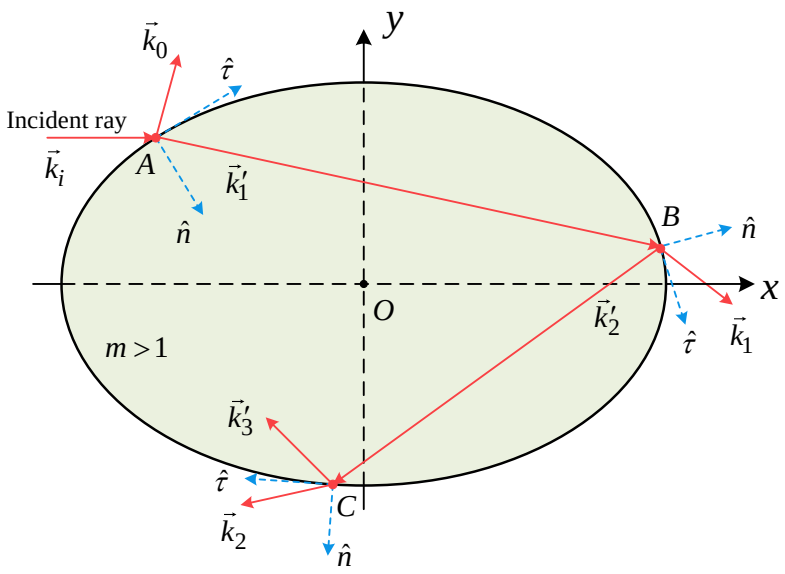

Figure 3.5 – Ray tracing in an ellipse.

In the base ($\hat{e}_x$ and $\hat{e}_y$) To determine the coordinates at the next interaction point after the previous interaction point we need the direction parameters of the ray, which are the two components of the wave vector of the refracted ray. Let $\vec{k}$ the wave vector between two successive points and (k_n, k_τ) its components in the base $(\hat{n}, \hat{\tau})$. Then

$$\vec{k} = k_x\hat{e}_x + k_y\hat{e}_y \tag{3.28}$$

where $\hat{e}_x$ and $\hat{e}_y$ are two unit vectors in x and y direction for Cartesian coordinate system. k_x and k_y are given as

$$\begin{aligned} k_x &= k_n n_x + k_\tau \tau_x \\ k_y &= k_n n_y + k_\tau \tau_y \end{aligned} \tag{3.29}$$

The equation of the ray is given as

$$y = \kappa x + b_0 \tag{3.30}$$

where κ and b_0 is given as

$$\kappa = \frac{k_y}{k_x} \tag{3.31}$$

$$b_0 = y_0 - \kappa x_0 \tag{3.32}$$

where (x_0, y_0) are the coordinates of the previous point. The combination of Eq. (3.17) and (3.30) yields

$$(b^2 + a^2\kappa^2)x^2 + 2\kappa b_0 a^2 x + (b_0^2 - b^2)a^2 = 0 \tag{3.33}$$

The coordinates of the next interaction point (x_1, y_1) are then the solution of Eq. (3.30) given as

$$\begin{aligned} x_c &= \frac{-\mathrm{B} \pm \sqrt{\mathrm{B}^2 - 4\mathrm{AC}}}{2\mathrm{A}} \\ y_c &= \kappa x_c + b_0 \end{aligned} \tag{3.34}$$

where

$$\begin{aligned} \mathrm{A} &= (b^2 + a^2\kappa^2) \\ \mathrm{B} &= 2\kappa b_0 a^2 \\ \mathrm{C} &= ({b_0}^2 - b^2)a^2 \end{aligned} \tag{3.35}$$

The sign $\pm$ in Eq. (3.34) take that of k_x.

The distance between the two points is

$$d = \sqrt{(x_c - x_0)^2 + (y_c - y_0)^2} \tag{3.36}$$

Phase due to optical path

The schema for the calculation of phase due to optical path is shown in Figure 3.6. We define first the reference ray as a ray arriving at O from the same direction as the incident ray and goes out as the emergent ray as if there is no particle.

The phase for $p = 0$ relative to the reference is given as

$$\Phi_P = -\vec{k}_i \cdot \overrightarrow{OC} + \vec{k}_0 \cdot \overrightarrow{OC} \tag{3.37}$$

The phase of $p = 1$ is given as

$$\Phi_P = -\vec{k}_i \cdot \overrightarrow{OC} + \vec{k}_1 \cdot \overrightarrow{OE} - mk\overline{CE} \tag{3.38}$$

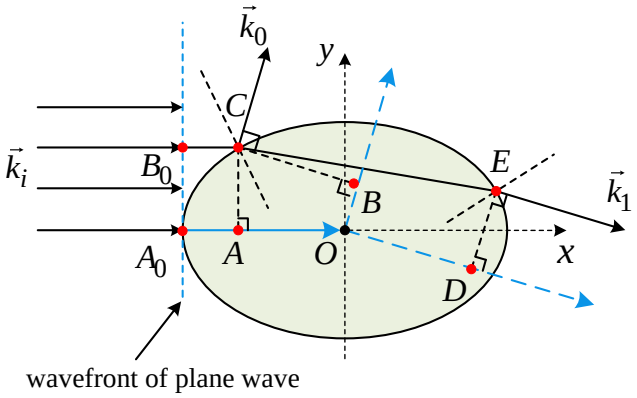

Figure 3.6 – Calculation of the phase of the optical path in a non-spherical particle.

In general, we deduce that the phase due to optical path of order p is given by

$$\Phi_P = (\vec{k}_p \cdot \vec{r}_p - \vec{k}_i \cdot \vec{r}_0) - \sum_{q=1}^{p} \vec{k}'_q \cdot (\vec{r}_q - \vec{r}_{q-1}) \tag{3.39}$$

where $\vec{r}_0$ is the position vector of the incident point, $\vec{k}_p$ is the wave vector of the emergent ray of order p, $\vec{r}_p$ the position vector of the emergent point, $\vec{k}'_q$ is the wave vector from the $(q-1)^{th}$ to the q^{th} interaction points inside the particle. In the special case of a spherical particle, Eq. (3.39) reduces to Eq. (2.38).

Amplitude and phase of emergent rays

The wavefront curvatures at each interaction point can be calculated by Eq. (3.3) for the infinite elliptical cylinder and by Eqs. (3.2) and (3.3) for the ellipsoidal particle. The phase due to focal lines, the phase of Fresnel coefficients, the Fresnel factor and the divergence factor are calculated with formulas given in the previous section without difficulty. Therefore, we can calculate the complex amplitudes of all the

emergent rays. But in practice, the directions of the emergent rays are irregular, we cannot calculate directly the total field by their summation. The interpolation is necessary to calculate the amplitudes and the phases of the all the emergent rays at the given direction. The total field at the that direction is the summation of the interpolated complex amplitudes.

3.2.3 Scattering diagrams of an infinite elliptical cylinder

According to Eqs. (3.15) and (2.55), the scattering diagrams of an infinite elliptical cylinder for the perpendicular and parallel polarizations are calculated. We shown in the following some examples.

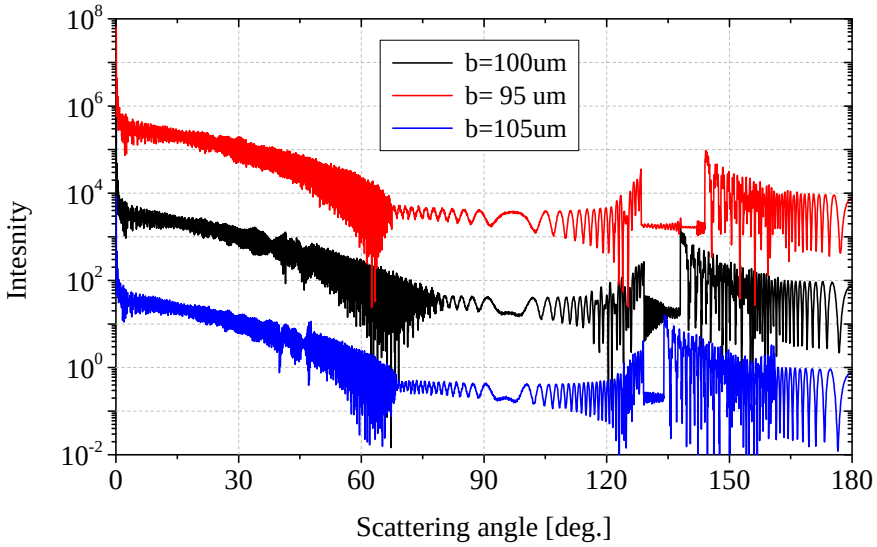

Figure 3.7 – Scattering diagrams of an infinite elliptical cylinder. The incident wavelength is 0.6328 µm and in perpendicular polarization. The other parameters of the particles are $a = 100$ µm and the relative refraction index $m = 1.333$. For clarity, the scattering diagrams are offset by 10^{-2} and 10^{2}.

We find, in Figures 3.7 and 3.8, that the intensity in the rainbow region is sensitive to the parameter b. In other regions such as in the region $[90°, 110°]$ in perpendicular polarization, this obvious discrepancies is due to the effect of parameters b to their optical path and divergence factor for $p = 0$ and $p = 3$. In the region of $[65°, 82°]$ in parallel polarization, the intensity varies strongly as function of b, this is due to the effect of b to order $p = 1$, the edge ray of $b = 100$ is in $\theta = 80°$, but the edge rays of the particles $b = 95$ and $b = 105$ are in $\theta = 67°$ and $\theta = 68°$ respectively. So, the small variation of b can affect the scattering diagrams obviously.

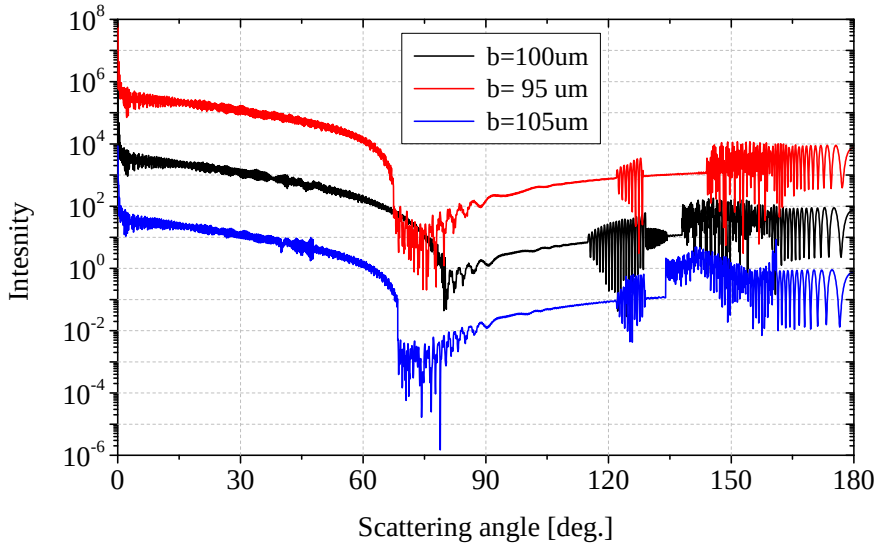

Figure 3.8 – Scattering diagrams of an infinite elliptical cylinder. Same parameters as Figure 3.7 except for parallel polarization.

3.2.4 Scattering diagrams of an ellipsoid

According to Eqs. (3.11) and (2.55), the scattering diagrams of an ellipsoid on their equatorial plane are shown in Figures 3.9- 3.11. The forward diffraction of an ellipsoid is

$$\mathrm{E}_d(\theta) = k^2 bc \frac{\mathrm{J}_1(kb\theta)}{kb\theta} \tag{3.40}$$

The infinite elliptical cylinder can be seen as a special condition of an ellipsoid when its c (that is the semi-axes perpendicular to incident plane) is much larger than the parameters a and b. So, compare the Figures 3.7, 3.9 and 3.10 or 3.8 and 3.11, we can analyse the effect of different c to scattering diagrams. From these Figures, we can find the curvature radii in perpendicular plane of the particle can affect the scattering diagrams in equatorial plane.

For the scattering diagrams in perpendicular, in Figures 3.7 and 3.9, the hyperbolic umbilic (HU) phenomenon caused by parameter c (c is smaller than a and b [101]) is obvious and its direction is also affected by the ratio of b/a. According to Figures 3.7 and 3.10, we also find c (c is bigger than a and b [101]) can cause another kind caustics by the rays of $p = 3$. Its position is affected also by the ratio of b/a. Besides, the scattering diagrams of these three ellipsoid also keep similarly trends as as Figure 3.7 because of same shape in incident plane. For the scattering diagrams in parallel polarization, in Figures 3.8 and 3.11, the parameters c still has the similar

effects for the scattering diagrams in parallel polarization. The scattering diagrams for the particle with b = 95 and b = 105 are offset by 10^4 and 10^{-4} respective for clarity.

Therefore, for the scattering of an ellipsoid in its equatorial plane, the parameters c still has the effect to the trend of scattering diagrams both in perpendicular and parallel polarization.

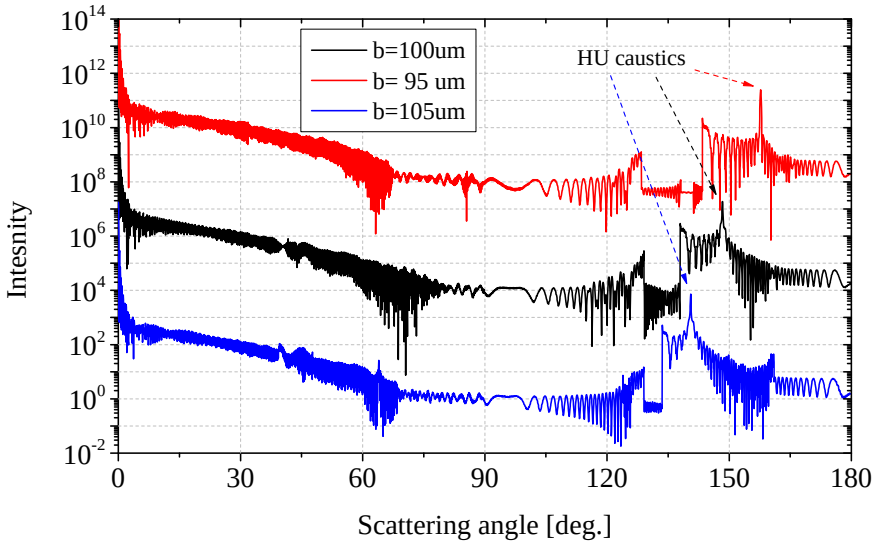

Figure 3.9 – Scattering diagrams of an ellipsoid. For the particle, parameters of a = 100 µm, c = 85 µm, the other parameters are the same as Figure 3.7.

In Table 3.1, the computation time for light scattering by non-spherical particles are shown in Figure 3.9. The number of incident ray and scattering angle is 4000. Their simulation time is near 0.469 s. For other simulations in this Chapter, their time are close to Table 3.1. We can find VCRM is quilt efficient compared with numerical methods.

Table 3.1 – Computation time for light scattering by non-spherical particles in the Figure 3.9.

b(µm)	CPU time of Simulation (s)
95	0.468
100	0.469
105	0.469

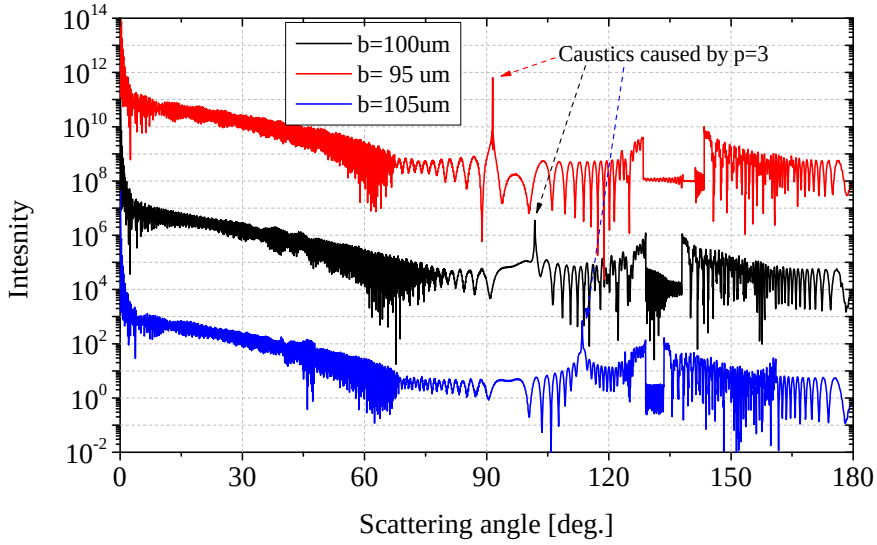

Figure 3.10 – Scattering diagrams of an ellipsoid of a = 100 µm, c = 135 µm, the other parameters are the same as Figure 3.7.

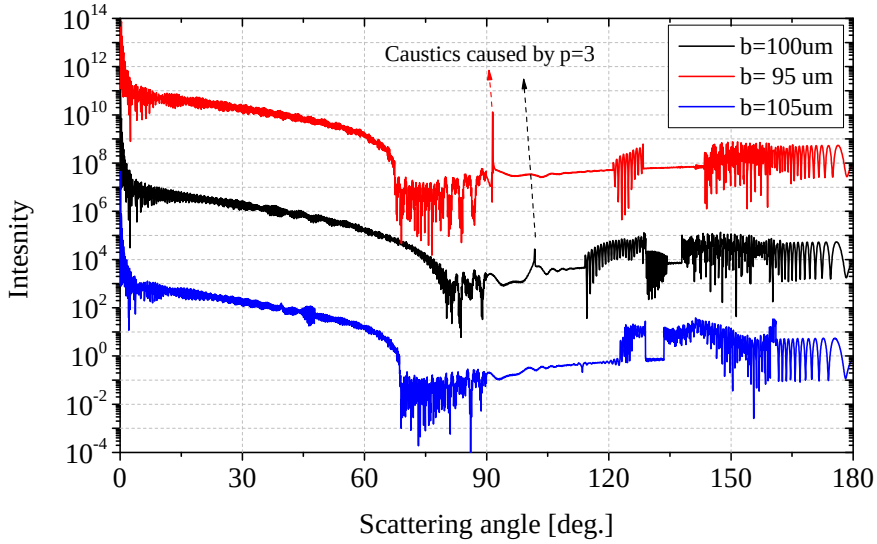

Figure 3.11 – Scattering diagrams of an ellipsoid with the same parameters as Figure 3.10 except that the incident wave is in the parallel polarization

3.3 Summary

The Vectorial Complex Ray Model (VCRM) developed in the CORIA laboratory permits to predict the amplitude and the phase of a ray at any position for a particle of any shape of smooth surface. The essentials of this model are presented and applied to the scattering of an infinite elliptical cylinder and an ellipsoid. The relation of the scattering patterns, especially the geometrical rainbow angles as function of the shape of the particle has been studied. Since VCRM is still a ray model the flaw of the intensity discontinuity at the rainbow angle persists. This problem is to be undertaken in the next chapter by the combination of VCRM with the PO.

Chapter 4

Rainbow theory based on VCRM and PO

The geometrical optics (GO) and the Vectorial complex ray model (VCRM) for light scattering presented in the two previous chapters are pure ray models. Because of the high symmetry of a sphere, the scattering angle, the phase and the amplitude in far field of each emergent ray can be calculated analytically in the framework of the GO. On the other hand, thanks to the new property of rays – the wavefront curvature — in the VCRM, we can predict further the phase and amplitude of each ray at any position along a ray for a particle of any shape of smooth surface. The simulations have demonstrated that both the GO and the VCRM can predict well the scattering diagrams in almost all directions. However both fail in the vicinity of the geometrical rainbow angles. In fact, this is at the same time a troublesome and a fruitful subject to the physicians since longtime. And it has not been completely solved until nowadays, even for a spherical particle. We will address this problem in this chapter by combining the VCRM and the physics optics.

The rainbow is one of the most beautiful phenomena in nature. Research on its formation attracts curious minds and great scientists [1, 4, 49]. Descartes gave the first satisfactory explanation of a rainbow by numerical simulation based on his new discovered refraction law. He considered the rainbow as the extreme deviation angles of the emergent rays [R. Descartes, Oeuvres complètes, III. Discours de la méthode et essais, pp355-361]. Evidently the intensity is not continuous at these angles, this fact does not agree with the reality because no physical quantity can be discontinuous in the real world.

In fact, this geometrical rainbow angle θ_R can be determined analytically using

the deviation angle Eq. (2.32), or by setting the divergence factor to infinite of Eqs. 2.33 and 2.45. Here again, the infinite intensity is not realistic neither.

To address this problem, Airy provided a formula [3, 4] – integration of the field on a virtual line perpendicular to the rainbow ray. For nearly two centuries this theory has been studied by mathematicians and physicists from different points of view. For example, several authors [12, 64, 86] have shown that the intensity maxima in the scattering patterns of a spherical drop should be corrected by a factor. However, the comparison with the rigorous Debye theory illustrated clearly that the discrepancy between the improved Airy theory and the rigorous theory is still evident [65], and this increases as a function of the order p and the angle difference $\theta - \theta_R$. On the other hand, it is known also that Airy theory failed to predict correctly the scattering patterns for the parallel polarization [49, 81, 84]. So it is necessary to examine if these discrepancies are an intrinsic flaw of the ray model or just due to the approximation in Airy theory.

4.1 Airy theory

To address the problem of the intensity discontinuity in the rainbow angles, Airy calculated the phases of the emergent rays in the neighbourhood of rainbow angle by expanding the relations obtained in the geometrical optics in the vicinity of the rainbow angle. The amplitude of the emergent wave near rainbow angle is assumed as constant amplitude along a virtual line. We recall first the Airy theory and its improvements.

4.1.1 Airy approximations for the phase and amplitude

When a ray impinges on a spherical particle of relative refractive index m (see Figure 4.1), the incident angle θ_i and the refraction angle θ_r are related by Snell's law Eqs. (2.2) and (2.3). The deviation angle of the emergent ray of order p is given by Eq. (2.25). In the geometrical optics point of view, the rainbows occur when the deviation angle reaches the extremum value θ_R. By setting $d\theta_p/d\tau = 0$ in Eq. (2.24) and using Eq. (2.3), we have

$$\sin\tau_R = \sqrt{\frac{m^2-1}{p^2-1}}, \tag{4.1}$$

Though θ_R can locate the position of the rainbow, the GO cannot predict correctly the intensity near the rainbow angle. To remedy this problem, Airy applied diffraction theory [4] to calculate the scattering intensity in the neighborhood of the rainbow angle by integration of the complex amplitude on the virtual line v perpendicular to the rainbow ray. To obtain the phase function on this line, Airy developed θ_p as a function of τ near the rainbow angle θ_R as

$$\theta - \theta_R \approx \frac{d\theta}{d\tau}(\tau - \tau_R) + \frac{1}{2}\frac{d^2\theta}{d\tau^2}(\tau - \tau_R)^2, \tag{4.2}$$

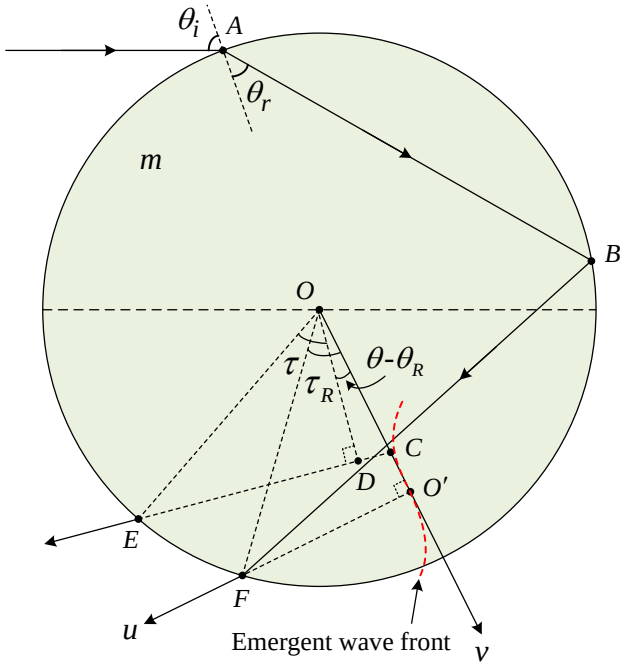

Figure 4.1 – The emergent rays in the neighbourhood of the rainbow angle.

According to Eqs. (2.3), (2.24) and the condition $d\theta/d\tau = 0$ [4], we have

$$\frac{d^2\theta}{d\tau^2} = \frac{2}{\tan\tau_R}\left(1 - \frac{1}{p^2}\right) \tag{4.3}$$

So, Eq. (4.2) is given as

$$\theta - \theta_R = \frac{1}{\tan\tau_R}\left(1 - \frac{1}{p^2}\right)(\tau - \tau_R)^2 \tag{4.4}$$

On the other hand, the coordinate v is defined as (see geometrical means in Figure

4.1)

$$v = a\cos\tau - a\cos\tau_R \tag{4.5}$$

Again, in the vicinity of the rainbow angle θ_R, v can be approximated to

$$v \approx -a(\tau - \tau_R)\sin\tau_R. \tag{4.6}$$

We define the orthogonal coordinates $(O' : u, v)$ with u along the rainbow ray and v passing by the particle center. The tangent of the wavefront curve

$$\frac{du}{dv} = \tan(\theta - \theta_R) \approx \theta - \theta_R, \tag{4.7}$$

By combining Eqs. (4.4) and (4.6), we obtain finally

$$\frac{du}{dv} = \frac{v^2}{a^2\sin^2\tau_R\tan\tau_R}\left(1 - \frac{1}{p^2}\right) \tag{4.8}$$

By integration on v, we find the cubic phase function

$$u = \frac{h}{3a^2}v^3 \tag{4.9}$$

where h is a constant [7] given as

$$h = \frac{(p^2-1)^2}{p^2}\frac{(p^2-m^2)^{1/2}}{(m^2-1)^{3/2}} \tag{4.10}$$

We would note that in obtaining this cubic phase function, the approximation $\theta - \theta_R \sim 0$ is used in Eqs. (4.2), (4.5) and (4.7). So, the cubic phase function is valid only in the vicinity of the rainbow angle θ_R.

4.1.2 Scattered field in the neighbourhood of rainbow angle

To obtain the amplitude of the scattered field in the neighbourhood of rainbow angle, Airy assumed further that the amplitude of the emergent rays on the v line is constant and "omit entirely the integration for the ordinate perpendicular to the plane of x, y, because it would only introduce a factor common to every part, and therefore would not modify the proportion of intensity at different points." [3]. So the amplitude of the scattered field ("whole disturbance" of Airy) in the angle θ can be calculated by an integral in the form

$$\int_{z'} \exp\left[-ik(\theta-\theta_R)v + iku(v)\right] dv \tag{4.11}$$

He argued further [3] that the limits through which the integration is to be performed are from z' a sensible quantity negative to z' a sensible quantity positive, and on account of the minuteness of the divisor λ (wavelength), this will be the same as taking it between the limits $-\infty$, $+\infty$". Finally, the amplitude of the scattered field is calculated by

$$E(\theta) = C\int_{-\infty}^{\infty} \exp\left[-ik(\theta-\theta_R)v + ik\frac{h}{3a^2}v^3\right] dv \tag{4.12}$$

The constant C has no influence on the profile of the scattering diagram but depends on the shape and refractive index (so the Fresnel factor) of the particle. Several authors have investigated it [12, 64, 86, 107].

The constant C for the infinite circular cylinder is given as

$$C = \frac{k}{2}|\epsilon_{X,p}| \tag{4.13}$$

where $\epsilon_{X,p}$ is the Fresnel coefficient of the rainbow ray. By using the simple change of variable $t^3 = \frac{kh}{a^2}v^3$, the Eq. (4.12) is rewritten as

$$E(\theta) = C\left(\frac{kh}{a^2}\right)^{-1/3}\int_{-\infty}^{\infty} \exp\left[-i\frac{\alpha^{2/3}}{h^{1/3}}(\theta-\theta_R)t + i\frac{t^3}{3}\right] dt \tag{4.14}$$

we define ξ

$$\xi = -\left(\frac{\alpha^2}{h}\right)^{1/3}(\theta-\theta_R) \tag{4.15}$$

where $\alpha = ka$ is the size parameter. According to the definition of the Airy function in appendix A.1, the scattered field of an infinite circle cylinder in the rainbow region is eventually given as

$$E(\theta) = \frac{\pi|\epsilon_{X,p}|\alpha^{2/3}}{h^{1/3}}\mathrm{Ai}(\xi) \tag{4.16}$$

If the particle is spherical, the divergence factor of the wave in the direction perpendicular to the scattering plane must be considered. Tricker [12] has shown that the factor should be multiplied by a size- and wavelength-dependent factor $\sqrt{a/\lambda}$. On the other hand, the factor C should take into account the ratio of the divergence factor of a sphere to that of a circular cylinder $(\sin\theta_{iR}/\sin\theta_R)^{1/2}$ (θ_{iR} being the inci-

dent angle corresponding to θ_R)[3]. The constant C in Eq. (4.12) is therefore

$$C = k|\epsilon_{X,p}|\left(\frac{\sin\theta_{iR}}{\sin\theta_R}\frac{a}{\lambda}\right)^{1/2} \tag{4.17}$$

Similar deduction to the case of the infinite circular cylinder, the scattered field of a sphere in the neighbourhood of the rainbow angle is given by

$$E(\theta) = |\epsilon_{X,p}|\frac{\alpha^{7/6}}{h^{1/3}}\left(\frac{2\pi\sin\theta_{iR}}{\sin\theta_R}\right)^{1/2}\mathrm{Ai}(\xi) \tag{4.18}$$

This equation is consistent with those of Nussenzveig, and Wang and van de Hulst [64, 86] both of them concluding that a factor $\alpha^{1/3}$ should be added to the intensity but for different reasons.

To evaluate the precision of the Airy theory, we compare in the following its results with the scattering diagrams calculated by the rigorous Debye theory for both the infinite circular cylinder and the sphere.

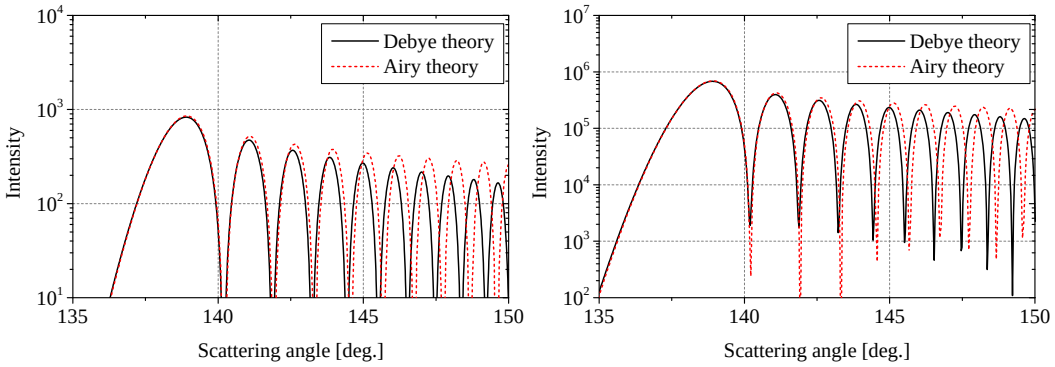

(a) Infinite circular cylinder (b) Sphere

Figure 4.2 – Scattering diagrams of an infinite circle cylinder (left) and a sphere (right) of $p = 2$ in the rainbow region. The polarization of the incident wave ($\lambda = 0.6328$ μm) is perpendicular to the scattering plane. The radius of the particle is $a = 100$ μm and its relative refraction index $m = 1.333$.

The scattering diagrams calculated by Eq. (4.16) for an infinite circular cylinder and by Eq. (4.18) for a sphere are compared, respectively, to those predicted by the Debye theory in Figures 4.2 and 4.3 for the perpendicular and parallel polarizations.

We find that for the perpendicular polarization (Figure 4.2) Airy theory is in good agreement with the Debye theory for the main supernumerary bow, but the discrepancy increases gradually as function of the angle difference $(\theta - \theta_R)$. And the positions of the intensity maximum and the minimum of the Airy theory around 150°

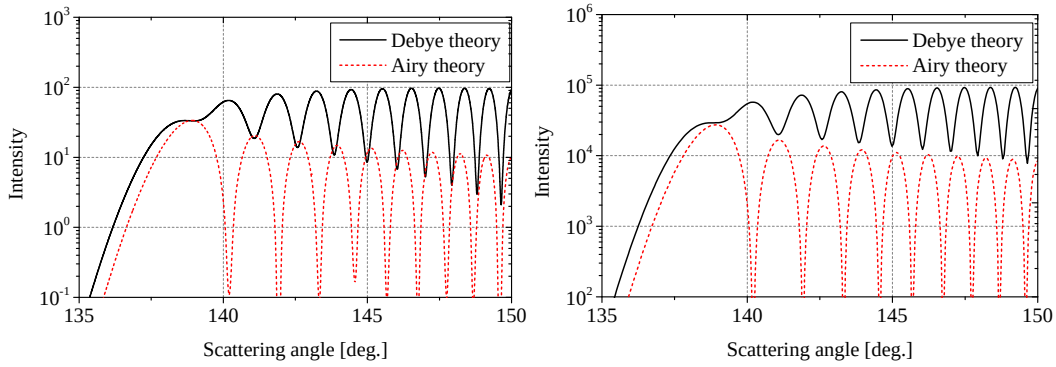

(a) Infinite circular cylinder (b) Sphere

Figure 4.3 – Same parameters as Figure (4.2) except that the polarization of the incident wave is in parallel scattering plane.

are opposite to those of Debye theory.

In the case of the parallel polarization (Figure 4.3), Airy theory fails completely to predict the scattering diagrams. Its maximum and minimum positions are inverse to those of the Debye theory near the geometrical rainbow angles. The profile of the scattering diagram of the Debye theory for parallel polarization is completely different from that of the perpendicular polarization with the plateau after the rainbow angle while the Airy theory predicts always the similar profile.

The similar results have been reported by several authors for the spherical particle [65, 84, 86]. For discrepancies of perpendicular polarization, its is mainly caused by its approximations on phase (cubic function) and amplitude (constant). These approximations is accurate in the rainbow angle. For a discrepancies of parallel polarization, apart from in perpendicular polarization, the phase shift π at Brewster's angle is omitted. The results of the Airy theory for a spherical particle will be given and examined in details in Section 4.3.

4.2 Phase and amplitude calculated by VCRM

In fact, the precision of the Airy theory has been always wondered by researchers [1, 111]. Several authors intended to take into account the amplitude variation, other try to extend the expansion order of the phase function. For example, Tanakadate expanded in 1907 both the amplitude and the phase functions in the vicinity of rainbow angle until the fifth order [122], but his work has been completely forgotten (no citation found in the literature). In the 1979s, Können and de Boer [84]

took into account the strong variation of the amplitude around Brewster's angle by expanding the Fresnel coefficient in the neighborhood of this angle to improve the result, but they have not given a quantitative comparison with the rigorous theory. This is due probably to the difficulty in the integration with high order phase function [64, 65, 111].

Here, we use a completely new strategy: The amplitude and the phase of all the emergent rays along the v line are calculated rigorously in the sense of ray model by the VCRM. Then, the scattered amplitude in the far field is calculated by the interference of the emergent rays or by the diffraction integration according to their angular position relative to the geometrical rainbow angle.

The coordinate v of an emergent ray CE (Figure 4.1) is given as its angle τ and the deviation angle θ by

$$v = \frac{a\cos\tau}{\cos(\theta-\theta_R)} - a\cos\tau_R \tag{4.19}$$

The origins O′ of the axis v is the intersection of the geometrical rainbow ray Fu and the axis v. The phase $\Phi(v)$ of an emergent ray having the intersection point with v-axis at v is calculated by

$$\Phi(v) = \Phi_P + \Phi_F + \Phi_f + \Delta\Phi_{vir} - \Phi_R, \tag{4.20}$$

where Φ_R is the phase of the geometrical rainbow ray, $\Delta\Phi_{vir}$ is the phase shift due to the suplementary distance $\overline{CD}$ from the virtual line given as

$$\Delta\Phi_{vir} = ka\cos\tau\tan(\theta-\theta_R) \tag{4.21}$$

Φ_P, Φ_F and Φ_f are the phase of optical path, Fresnel coefficient, and focal line, respectively, as given in Chapter 2.

The amplitude of an emergent ray on the virtual line v is determined by the Fresnel factor and the divergence factor. The former remains unchanged and the latter is to be revised because that given in Chapter 2 is for the far field.

In the VCRM, the intensity variation due to the divergence is calculated directly by the ratios of the wavefront curvatures. The divergence factor of the ray on the virtual line v due to the divergence on the scattering plane is given by

$$\mathcal{D}_{2,vir} = \frac{R'_{21}}{R_{22}}\frac{R'_{22}}{R_{23}}\cdots\frac{R_e}{R_e+d_{vir}} \tag{4.22}$$

where d_{vir} is the distance between the emergent point $\mathrm{E}(x_e, y_e)$ and the point on the v line $\mathrm{C}(x_v, y_v)$ given as

$$d_{vir} = \sqrt{(x_v - x_e)^2 + (y_v - y_e)^2} \tag{4.23}$$

In order to compute d_{vir}, we need to determine the coordinates of the emergent point (x_e, y_e). The angular position of the emergent ray of order p is (Figure 4.4)

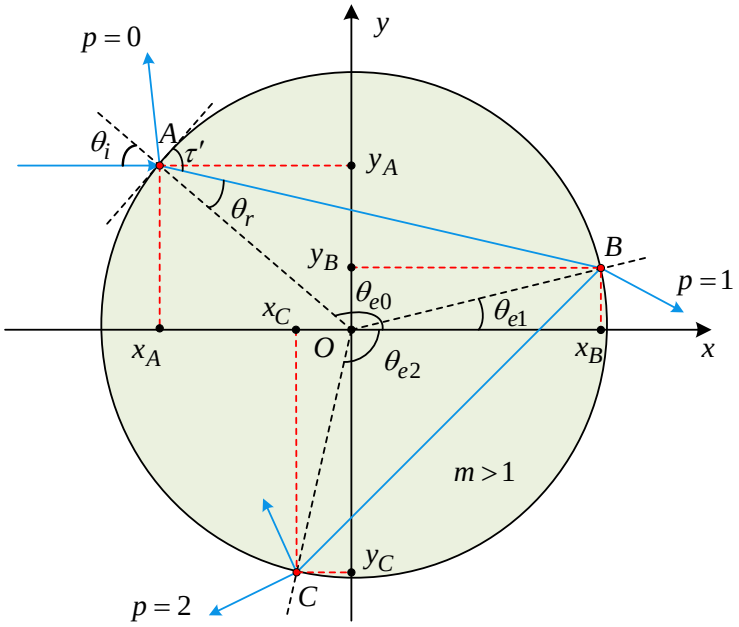

Figure 4.4 – Incident point and emergent point of a ray.

$$\theta_e = \theta_{e0} - 2p\tau' \tag{4.24}$$

θ_{e0} is the angle position of the incident point given by

$$\theta_{e0} = \mathrm{atan2}(y_i, x_i) \tag{4.25}$$

where (x_i, y_i) are the coordinates of the incident point. Therefore, the coordinates of the emergent point (x_e, y_e) are given as

$$(x_e, y_e) = (a\cos\theta_e, a\sin\theta_e) \tag{4.26}$$

and the equation of the emergent ray is given as

$$y = \tan\theta(x - a\cos\theta_e) + a\sin\theta_e \tag{4.27}$$

Know that the equation of the virtual line v is

$$y = -\frac{x}{\tan\theta_R} \tag{4.28}$$

by solving the two above Eqs. (4.27) and (4.28) for x, y, we find the coordinates (x_v, y_v) as

$$(x_v, y_v) = \left(a\tan\theta_R \frac{\tan\theta\cos\theta_e - \sin\theta_e}{\tan\theta\tan\theta_R + 1}, \frac{-x_v}{\tan\theta_R}\right) \tag{4.29}$$

Thus, the distance d_{vir} and the divergence factor can be calculated by Eq. (4.23) and (4.22) respectively.

Now we can examine the precision of the phase and the amplitude in the Airy theory. We compare in Figures 4.5-4.8 the phase and amplitude of the Airy theory Eq. (4.9) with those calculated by Eqs. (4.20) and (4.22).

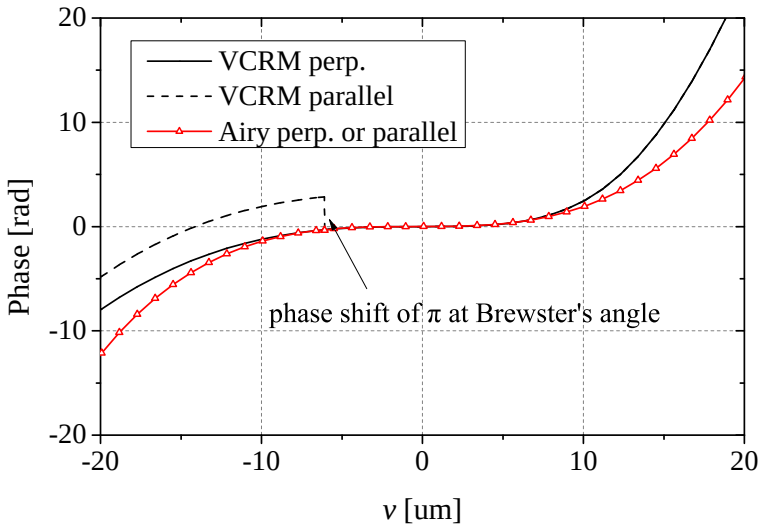

Figure 4.5 – Phase on the virtual line of $p = 2$. The polarization of the incident wave ($\lambda = 0.6328$ μm) is perpendicular to the scattering plane. The radius of the particle is $a = 100$ μm and its relative refraction index $m = 1.333$.

The phases of the two polarizations for the rays of order $p = 2$ are compared in Figure 4.5. We find that the phase of the Airy cubic phase function is in good agreement with that of the VCRM in the vicinity of the geometrical rainbow angle, i.e. for $v \sim 0$, but the discrepancy increases with v and attains π when v is about

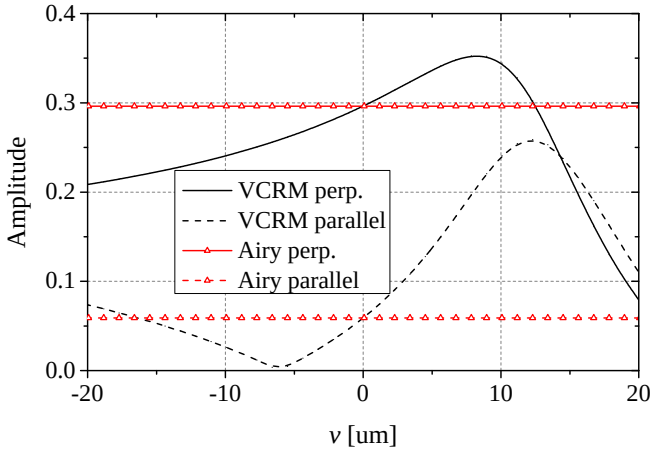

Figure 4.6 – Amplitude on the virtual line of $p = 2$. Same other parameters as in Figure 4.5.

-18 µm and 15 µm for the perpendicular polarization. In the case of the parallel polarization, there is a supplementary phase jump of π at the Brewster's angle which is not considered in the Airy theory.

The amplitude of the rays of order $p = 2$ for the two polarizations are compared in Figure 4.6. Airy assumed that the amplitude is constant. However, we find that it varies clearly as function of v according to the VCRM. At $v = 0$, the amplitudes of Airy and VCRM are the same because that is the reference point ($\mathcal{D}_{2,r} = 1$ and the same Fresnel factor). Out of this point, the amplitude varies as function of v in a different manner for the two polarizations. This variation is caused by two factors: the Fresnel factor $\varepsilon(v)$ and the divergence factor $D_{vir}(v)$. To examine precisely the influence of the two factors, we compare some numerical results of the divergence factor and the Fresnel factor in Table 4.1 and 4.2

In the first column of Table 4.1, the scattering angles of the emergent rays are presented. They are not regular because in the calculation, we take 2000 incident rays with a constant step along y in Eq. (3.24) of incident point and the scattering angles of the emergent rays are calculated by the Snell's law Eqs. (2.10)-(2.13). The corresponding coordinates v of these emergent rays are given in the second column. The wavefront curvature radii at different interaction points calculated by the wavefront equation (3.3) are given in the columns 3 to 7. They are, respectively, the refracted rays at the first interaction point $R'_{2,1}$, the incident rays at the second interaction point $R_{2,2}$, the reflected rays at the second interaction point $R'_{2,2}$, the incident rays at the third intersection point $R_{2,3}$ and the refracted/emergent rays at the third intersection point $R^e_{2,3}$. The distance between the emergent position and the coor-

Table 4.1 – Curvature radii (μm) in the scattering plane for the rays of order $p = 2$ near the rainbow angle. The incident wavelength is λ = 0.6328 μm, the relative refraction index m = 1.333, the radius of the particle is a = 100 μm. The number of the incident ray is N = 2000.

Angles(°)	v(μm)	$R'_{2,1}$	$R_{2,2}$	$R'_{2,2}$	$R_{2,3}$	$R^e_{2,3}$	d_{vir}	D_{vir}
...	...	...	...	...	...	...	...	
158.1180	20.23	72.10	−60.57	73.31	−59.36	−2.86	43.76	0.1028
156.8913	19.32	73.34	−59.49	75.17	−57.67	−3.21	42.61	0.1308
155.8650	18.58	74.46	−58.54	76.97	−56.04	−3.45	41.71	0.1575
...	...	...	...	...	...	...	...	...
137.9227	0.20	151.86	−0.63	−0.64	−153.14	6010	50.61	1.000
137.9220	0.10	152.37	−0.25	−0.25	−152.87	15228	50.78	1.000
137.9219	0.00	152.87	0.13	0.13	−152.62	−30580	50.95	1.000
137.9224	−0.10	153.38	0.51	0.50	−152.37	−7765	51.11	1.000
137.9234	−0.20	153.89	0.89	0.87	−152.13	−4492	51.28	1.000
...	...	...	...	...	...	...	...	...
138.7257	−6.00	182.68	22.76	14.50	−145.42	−300.47	61.06	1.005
138.7496	−6.09	183.17	23.13	14.66	−145.38	−297.87	61.22	1.005
138.7739	−6.19	183.65	23.51	14.81	−145.34	−295.37	61.39	1.005
...	...	...	...	...	...	...	...	...
143.9108	−19.74	247.52	73.71	27.34	−146.47	−201.38	82.09	1.058
143.9562	−19.84	247.95	74.06	27.39	−146.50	−201.24	82.22	1.058
144.0017	−19.93	248.38	74.40	27.45	−146.53	−201.11	82.35	1.059
...	...	...	...	...	...	...	...	...

dinate v of the ray as well as the divergence factor deduced from Eq. 4.22 are given in the last two columns. We find that the divergence factor is almost constant for the rays of coordinate v near zero or negative, but it decreases until about tenth at $v = 20$ μm.

For a particle of circular section, the angles of the rays relative to the normal of the particle surface are constant for all orders of rays. The influence of the Fresnel factor can be calculated simply by Eq. (2.10) and (2.13). The values of these factor for the same case as in Table 4.1 are given in Table 4.2 for the two polarizations. The final amplitude of the emergent rays on the virtual line v are then calculated by $E_X = \epsilon_X \sqrt{D_{dir}}$ and given in the last two columns. It is found that the final amplitude of the perpendicular polarization is influenced mainly by the divergence factor while that of the parallel polarization by the Fresnel coefficient, which has a strong variation around the Brewster's angle.

The curvature radii and the Fresnel factor of the rays of order $p = 3$ near the

Table 4.2 – Fresnel factor $\epsilon_X(v)$ and the amplitudes of the emergent rays on the virtual line v. The parameters are the same as in Table 4.1.

Angles(°)	v(μm)	$\epsilon_{\perp,2}(v)$	$\epsilon_{\parallel,2}(v)$	$\sqrt{D_{vir}}$	$E_{\perp,2}(v)$	$E_{\parallel,2}(v)$
...	...	...	...	...	...	
158.1180	20.23	0.23354	0.32722	0.32062	0.07489	0.10493
156.8913	19.32	0.26091	0.35071	0.36166	0.09435	0.12682
155.8650	18.58	0.28158	0.36527	0.39686	0.11175	0.14496
...	...	...	...	...	...	...
137.9227	0.20	0.29753	0.06093	1.00000	0.29753	0.06093
137.9220	0.10	0.29679	0.05969	1.00000	0.29679	0.05969
137.9219	0.00	0.29605	0.05846	1.00000	0.29605	0.05846
137.9224	−0.10	0.29531	0.05724	1.00000	0.29531	0.05723
137.9234	−0.20	0.29458	0.05603	1.00000	0.29458	0.05603
...	...	...	...	...	...	...
138.7257	−6.00	0.25818	0.00044	1.00235	0.25878	0.00044
138.7496	−6.09	0.25764	0.00032	1.00244	0.25827	0.00033
138.7739	−6.19	0.25711	0.00108	1.00253	0.25776	0.00108
...	...	...	...	...	...	...
143.9108	−19.74	0.20327	0.07072	1.02856	0.20909	0.07274
143.9562	−19.84	0.20300	0.07105	1.02883	0.20885	0.07310
144.0017	−19.93	0.20272	0.07138	1.02902	0.20861	0.07345
...	...	...	...	...	...	...

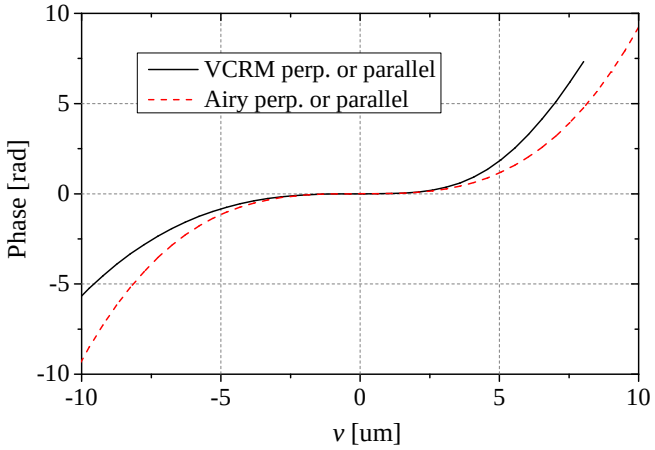

Figure 4.7 – Phase on the virtual line of $p = 3$ with the same parameters as in Figure 4.5.

rainbow angles are similar to those of the rays of order $p = 2$. The phase and the amplitude on the virtual line are shown Figures 4.7 and 4.8. However, three remarks are worth noting. Because the rays of order $p = 3$ are far from the Brewster's angle, there is no longer the jump of phase and the amplitude variation is more smooth for

the parallel polarization. Furthermore, the scale of v is limited in a smaller region because the edge ray is limited in the geometrical optics by

$$\theta_{p,edge} = 2p\cos^{-1}(1/m)$$

which corresponds to the ray at tangent incidence ($\theta_i = 90°$ and $\tau = 0$). The value of $v_{p,edge}$ can be calculated by Eq. (4.19). For a water drop we have $v_{2,edge} = 0.268a$ and $v_{3,edge} = 0.098a$. The variation of the phases and the amplitudes are therefore almost doubled. All these facts explain why the Airy theory works better for the lower orders and much better for the perpendicular polarization than for the parallel polarization.

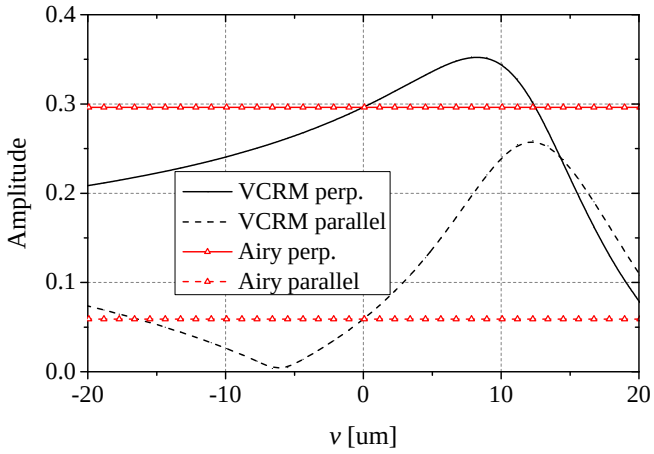

Figure 4.8 – Amplitude on the virtual line of $p = 3$. The parameters are the same as in Figure 4.5

4.3 Diffraction effect near rainbow angle

When the phase and the amplitude are calculated with VCRM, the scattering diagram in the neighbourhood of rainbow angle can be evaluated according to the Huygens-Fresnel principle (Eq. (2.14)) by integration with a manner similar to that used in the Airy theory. But the integration will be done numerically by using the Hopkins' algorithm because the phase and the amplitude are not in an analytical form, so the Airy function for a cubic polynomial function is not applicable according to Appendix B.

As in the last section, we will limit our discussion on the symmetric plane of the

particle when the scattering is concerned. The algorithm described in this section is applicable to the scattering in a symmetric plane by a particle of a circular or elliptical section. (In principle, it can be applied to a particle of arbitrary shape in the plane perpendicular to a caustics line).

Similar to Eq. (4.11) in the case of the Airy theory, the scattered amplitude in the neighbourhood of the rainbow angle can be calculated rigorously in the sense of ray model by the amplitude $\mathrm{A}_{\mathrm{X},p}(v)$ and the phase $\Phi_{\mathrm{T}}(v)$ on the virtual line according to

$$\mathrm{E}(\theta) = c_{\mathrm{D}} \int_{v_0}^{v_1} \mathrm{A}_{\mathrm{X},p}(v) \exp\left[i\Phi_{\mathrm{T}}(v)\right] dv \tag{4.30}$$

where c_{D} is a dimension dependent constant given as

$$c_{\mathrm{D}} = \begin{cases} \frac{k}{2} & \text{2D scattering: circular or elliptical cylinder, ...} \\ k & \text{3D scattering: sphere, ellipsoid, ...} \end{cases} \tag{4.31}$$

The integration boundary v_0 and v_1 are taken to be $v_0 = -2v_e$ and $v_1 = v_e$ with v_e the value of v of the edge ray because there is no ray outside this limit.

The total phase is calculated by

$$\Phi_{\mathrm{T}}(v) = -kv\sin(\theta - \theta_{\mathrm{R}}) + \Phi(v) \tag{4.32}$$

The amplitude is the product of the Fresnel factor $\epsilon_{\mathrm{X},p}$ and the divergence factor

$$\mathrm{A}_{\mathrm{X},p}(v) = |\epsilon_{\mathrm{X},p}| \sqrt{\mathrm{D}_{p,vir}}$$

The former is the same for the 2D and 3D scattering. The latter is given for the 2D scattering (an infinite cylinder) by

$$\mathrm{D}_{p,vir} = \left| \frac{\mathrm{R}'_{2,1}}{\mathrm{R}_{2,2}} \cdot \frac{\mathrm{R}'_{2,2}}{\mathrm{R}_{2,3}} \cdots \frac{\mathrm{R}^e_{2,p+1}}{(\mathrm{R}^e_{2,p+1} + d_{vir})} \right|$$

and for the 3D scattering (sphere, ellipsoid, ...) by

$$\begin{aligned} \mathrm{D}_{p,vir} =& \mathrm{D}_{1,p}\mathrm{D}_{2,p} \\ =& \left| k \frac{\mathrm{R}'_{1,1}}{\mathrm{R}_{1,2}} \cdot \frac{\mathrm{R}'_{1,2}}{\mathrm{R}_{1,3}} \cdots \frac{\mathrm{R}'_{1,p}}{\mathrm{R}_{1,p+1}} \mathrm{R}^e_{1,p+1} \right| \cdot \left| \frac{\mathrm{R}'_{2,1}}{\mathrm{R}_{2,2}} \cdot \frac{\mathrm{R}'_{2,2}}{\mathrm{R}_{2,3}} \cdots \frac{\mathrm{R}^e_{2,p+1}}{(\mathrm{R}^e_{2,p+1} + d_{vir})} \right| \end{aligned} \tag{4.33}$$

The first term is the divergence factor of the wavefront perpendicular to the scattering plane in infinity with the factor kr omitted as a convention for the same reason as in the Airy theory (section 4.1.2). The second term is due to the divergence of the wave in the scattering plane.

In the following sections we will examine by numerical calculation the influence of different factors in the scattering diagrams in the neighbourhood of the rainbow angle calculated by three methods: (1) Rigorous Debye theory, (2) Airy theory and (3) our method of VCRM with the PO.

4.4 Rainbow diagrams of an infinite circular cylinder

In order to isolate the influence of the diffraction effect from that of the divergence factor on the scattering diagram, we limit in this section to a 2D scattering problem – the scattering of a plane wave by an infinite circular cylinder of refractive index $m = 1.333$ illuminated by a plane wave of wavelength $\lambda = 0.6328$ μm at normal incidence. The geometrical optics rainbow angle is $\theta_R = 137.92°$, the incident wave is divided into N = 4000 rays with a constant step. The amplitude and the phase of each order of emergent wave are sampled with 300 points obtained from the those of the emergent rays. The complex amplitude of the scattered field at each given angle is then calculated by the integration with Hopkin's algorithm (see appendix B).

We begin by the most classical and common case: the scattering diagrams for the perpendicular polarization. This is also the most successful case of the Airy theory. In a series of figures bellow, we will compare the scattering diagrams in the rainbow region calculated by four methods: the Debye theory as reference, the Airy theory, the VCRM and the VCRM combined with PO.

In order to simplify the analysis, we anticipate two important points: The first is that the results of the VCRM with PO are in very good agreement with the Debye theory in all the cases presented here. The second is that the results of the VCRM agree well with those of the VCRM+PO except the main bow. We will therefore concentrate to the comparison of the Airy theory with the Debye theory – a rigorous method to be convincing. The difference between the VCRM and the VCRM+PO will be discussed when necessary.

For a particle of radius $a = 100$ μm (Figure 4.9), the peak position of the main supernumerary bow predicted by the Airy theory is at 138.92°, about 1.00° larger

than the geometrical rainbow position and in a very good agreement with the Debye theory. But the discrepancy of the peak positions predicted by the Airy theory increases with the angle difference $\Delta = \theta - \theta_R$ between the scattering angle θ and the geometrical rainbow angle θ_R. This amounts to about 1.3° around $\theta = 160°$, i.e. with about a shift of two peaks. The intensity predicted by the Airy theory is also in very good agreement with Debye for the first peak but different more and more when θ increases.

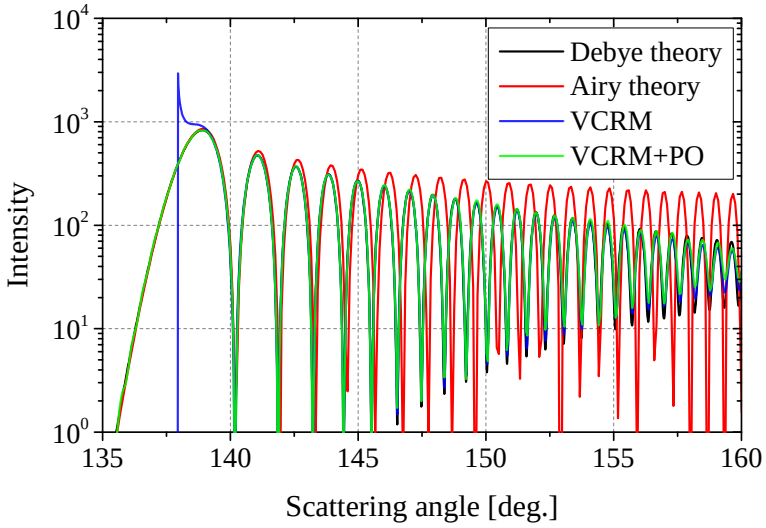

Figure 4.9 – Scattering diagrams of the primary rainbow of an infinite circular cylinder of refractive index $m = 1.333$ and radius $a = 100$ µm. The incident plane wave $\lambda = 0.6328$ µm is normal to the cylinder and polarized perpendicular to the scattering plane.

To investigate the precision of the Airy theory and our method, we compare in Figures 4.10 and 4.11 the scattering diagrams for a particles of radius $a = 1000$ µm and $a = 10$ µm respectively calculated in the same conditions.

We find that whatever the size of the particle ($a = 1000$ µm or $a = 10$ µm), the intensities and the angle positions of the first supernumerary bows of the Airy theory are in a good agreement with those of the Debye theory and of the VCRM+PO. We would note however that for a large particle, $a = 1000$ µm for example (Figure 4.10), the supernumerary bows are narrow, the angle difference Δ for several bows near the main peak is small, the intensities and the peak positions agree very well with those of the Debye theory. But for a small particle, say $a = 10$ µm, the angle difference Δ is already relatively large for the first peak, the difference between the results of the Airy theory and the Debye theory is clearly discernible even in the main peak. We note also that the intensity variation around 160° predicted by

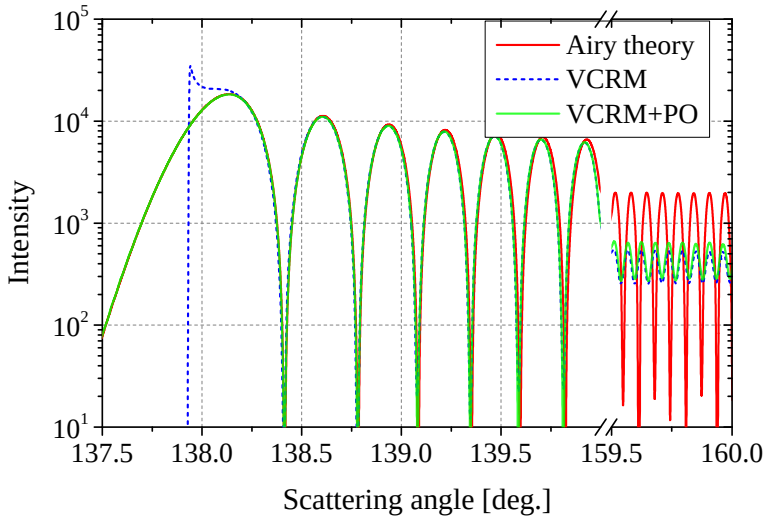

Figure 4.10 – Same parameters as Figure 4.9 except for $a = 1000$ μm.

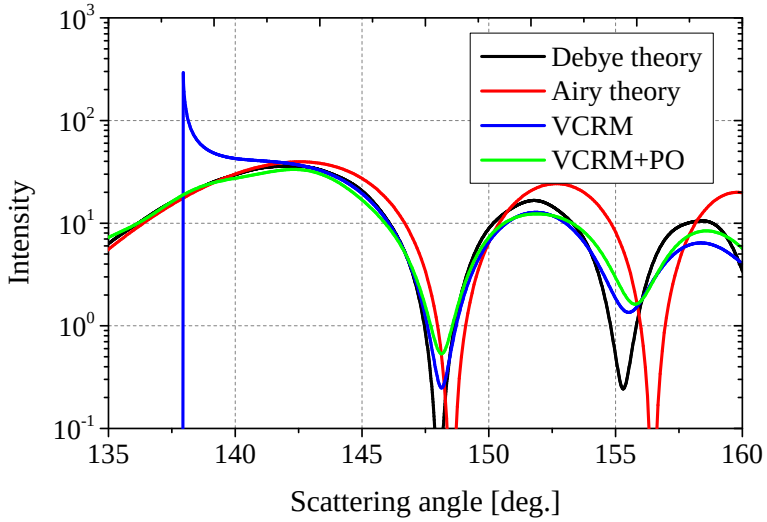

Figure 4.11 – Same parameters as Fig. 4.9 except for $a = 10$ μm.

VCRM, VCRM+PO, and the Debye theory are in good agreement and they are all much smaller than that of Airy theory.

In Figure 4.10 are shown also the supernumerary bows near 160°, but we must note that the supernumerary peak position of the Airy theory is about 1.3° larger than that predicted by the three other methods. The same case is found as that for a particle of 100 μm shown in Figure 4.9. Furthermore, the calculation of different particle sizes has shown that the peak position difference between the Airy theory and the other three methods is almost independent of the particle radius. So we may conclude that *the precision of the Airy theory is independent of the particle size*

(at least for the perpendicular polarization).

Now, we examine the precision of the scattering diagrams predicted by the four methods for the same particles but illuminated by a plane wave polarized in the scattering plane, i.e. parallel polarization case.

The scattering diagrams in the rainbow region of the cylinders of radius a = 100 µm, a = 1000 µm, a = 10 µm are compared respectively in Figures 4.12 , 4.13 and 4.14. We would note firstly that the results of VCRM+PO are in very good agreement with Debye theory in all the region for the three particles of very different sizes. And the results of the VCRM agree also very well with the Debye theory and the VCRM+PO except the main bow.

We find, as revealed by several authors [84, 86] and our results in the previous section (Figure 4.3), that the Airy theory fails to predict correctly the scattering diagrams for the parallel polarization. The difference between the Airy theory and the VCRM+PO for a cylinder of 100 µm (Figure 4.12) in the first three or four supernumerary bows is similar as that indicated by Khare and Nussenzveig [81] and analyzed already in the section 4.1. We can note also that if we compare the results in a large range we find that the distance between the supernumerary bows predicted by the Airy theory is larger than those predicted by the Debye theory and VCRM+PO.

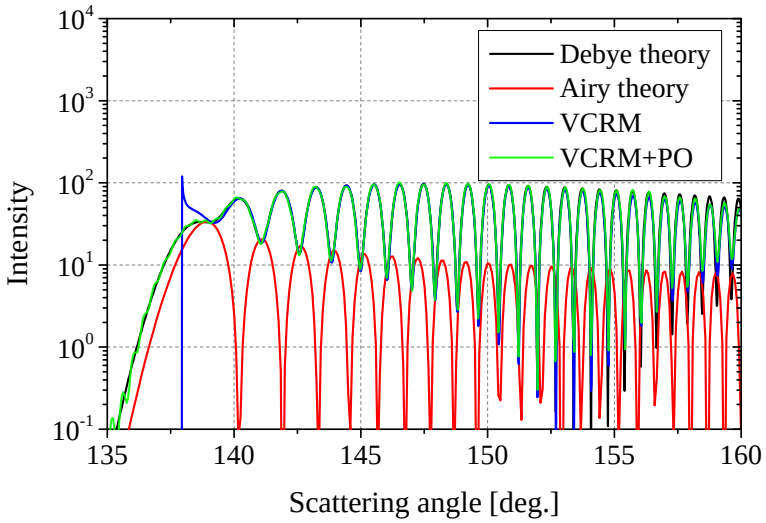

Figure 4.12 – Scattering diagrams of the primary rainbow of an infinite circular cylinder of refractive index m = 1.333 and radius a = 100 µm. The incident plane wave λ = 0.6328 µm is normal to the cylinder and polarized parallel to the scattering plane (along the axis of the cylinder).

For a very large particle (a = 1000 µm in Figure 4.13) the intensity predicted by

the VCRM+PO is almost constant near the geometrical rainbow angle so that the effect of the phase shift of π in Brewster angle (opposite of minima and maxima) is not so visible in the first three bows as for the particle of $a = 100$ μm. In the large scattering angle, the shift of the peak positions is similar as in the case of perpendicular polarization.

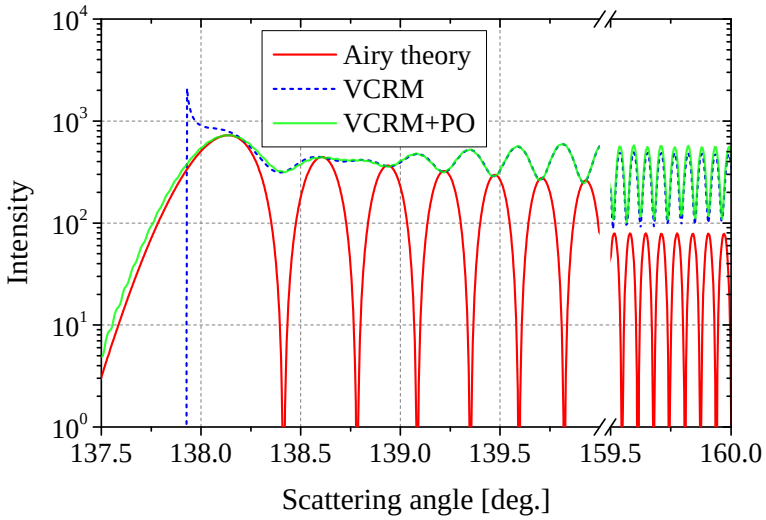

Figure 4.13 – Same parameters as Figure 4.12 except for the radius $a = 1000$ μm.

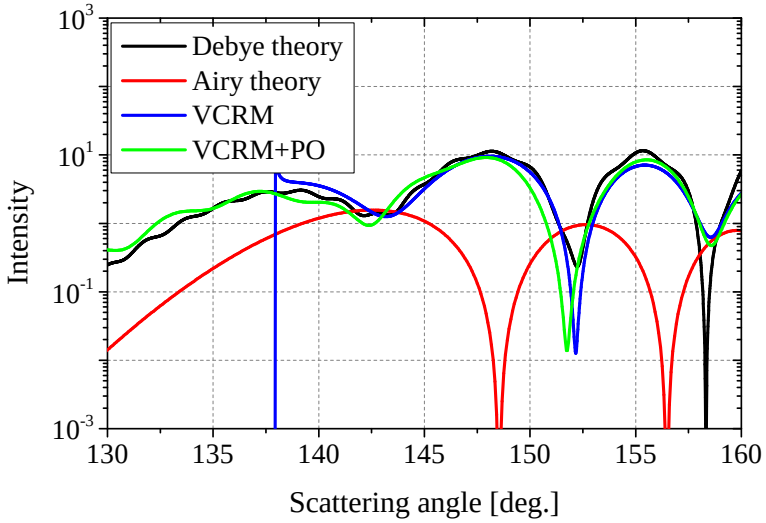

Figure 4.14 – Same parameters as Figure 4.12 except for the radius $a = 10$ μm.

When the particle is very small ($a = 10$ μm in Figure 4.14) the agreement between the Debye theory and the VCRM+PO is still very good and the effect opposite phase is also clear.

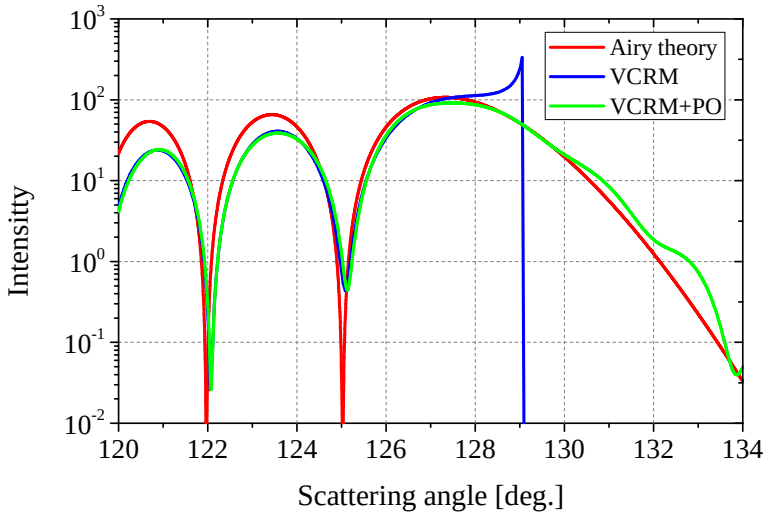

Figure 4.15 – Same parameters as Figure 4.9 except for $p = 3$.

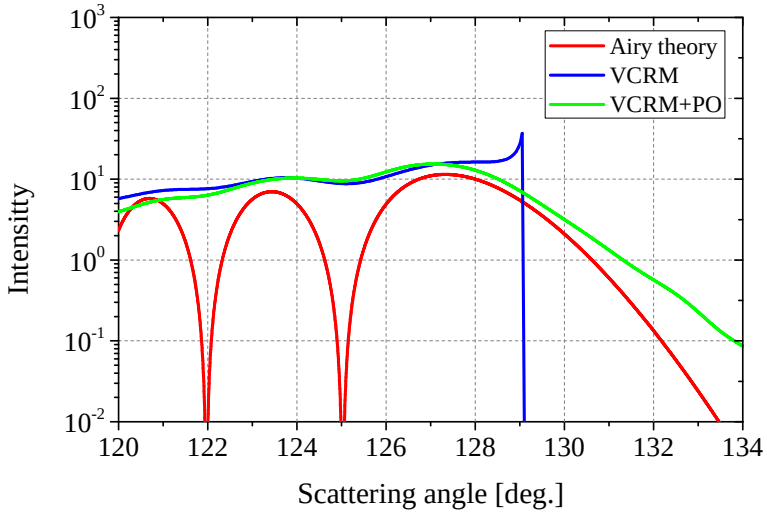

Figure 4.16 – Same parameters as Figure 4.12 except for $p = 3$.

Figures 4.15 and 4.16 present the scattering diagrams of the second order rainbow of a particle a = 100 µm for perpendicular and parallel polarization respectively.

4.5 Detailed examination of Airy theory with VCRM+PO

The precision of the Airy theory has been wondered and examined by researchers since long time [4, 89, 111, 123]. We have shown in the previous sections that for the perpendicular polarization, the discrepancy of the Airy theory from the rigorous theory increases as the angle difference between the scattering angle relative to the geometrical rainbow angle $\Delta = \theta - \theta_R$ due to the cubic phase function approximation.

But the problem for the parallel polarization is more complicated and less clear. Several authors agreed that the inverse of the maxima and the minima is due to the phase shift of π in the Brewster angle and some of them [84, 122] have proposed to develop the phase function and the Fresnel factor ϵ in Taylor series of higher orders, including the shift jump of π but not numerical comparisons are reported. The improvement of the precision is unknown/unclear.

Since the VCRM permits to calculate the phase and the amplitudes rigorously in the sense of ray model, we can examine in details the influence of each factors on the precision of the Airy theory.

We consider first the phase shift of π in the Airy theory. That is to calculate the scattering amplitude of an infinite circular cylinder near the rainbow angle by

$$E(\theta) = \frac{k}{2}|\epsilon_{X,p}| \int_{-\infty}^{+\infty} \exp\left[-ik\nu\Delta + \Phi_B(\nu)\right] d\nu \tag{4.34}$$

where the phase $\Phi_B(\nu)$ is calculated by considering the phase shift

$$\Phi_B(\nu) = \begin{cases} ik\frac{h}{3a^2}\nu^3 + \pi, & \nu \leq \nu_B \\ ik\frac{h}{3a^2}\nu^3, & \nu > \nu_B \end{cases} \tag{4.35}$$

ν_B is calculated by

$$\nu_B = \frac{a\cos\tau_B}{\cos(\theta_B - \theta_R)} - a\cos\tau_R \tag{4.36}$$

θ_B is the scattering angle where Brewster effect occurs, $\tau_B = \pi/2 - \theta_{i,B}$, with $\theta_{i,B}$ the corresponding incident angle given as

$$\theta_{i,B} = \arctan(m) \tag{4.37}$$

Because there is no rigorous solution of Eq. (4.34), we propose another numerical method in Appendix A.

The magenta curve in Figure 4.17 shows the numerical result calculated with Eq. (4.34). The black and red curves are for those of the Debye and Airy theory respectively. We see clearly that scattering diagrams calculated by the Airy theory with and without the phase at the Brewster angle of π are shifted a half period. These results demonstrate therefore that the inverse the minima and maxima of the supernumerary bows is well caused by the phase shift of π. But the intensity of the Airy theory with Φ_B remains the same and is still less than that of the Debye theory.

Konnen et al argued that the Fresnel coefficient for parallel polarization [84] is zero and this angle is near the rainbow angle for the primary rainbow, so the discrepancy of the Airy theory from the Debye theory is due to the Fresnel factor. They expanded the Fresnel factor in Taylor series to intend to improve the precision of the Airy theory. Here we can use directly the Fresnel factor ϵ calculated by ray tracing, i.e. the scattered amplitude is calculated by

$$E(\theta) = \frac{k}{2}\int_{v_0}^{v_e} |\epsilon_{2,2}| \exp\left[-ik\Delta v + \Phi_B(v)\right] dv \tag{4.38}$$

The boundary for the above integral v_0 is its real numerical results rather than $-2v_e$.

The cyan curve in Figure 4.17 is calculated with the above integral. It is evident that the intensity is improved considerably compared to those with constant amplitude (magenta curve). But compared to the Debye theory (black curve), the amplitudes are about one order of magnitude lower and the peak positions shift more and more as the supernumerary order.

In fact, Φ_B Eq. (4.38) takes into account only the phase jump of π in the cubic function, but the real phase differs from this function more and more as v increases. With VCRM we can calculated precisely the real phase variation $\Phi(v)$ as function of v and replace Φ_B in Eq. (4.38) by $\Phi(v)$ as shown in Figure (4.39). The result (blue curve) is evidently improved compared with cyan curve. Finally, we take into account the amplitude variation due to the divergence factor by Eq. (4.30), The result of this full version of the VCRM+PO is presented by the green curve in Figure 4.17. Now the result agrees perfectly with the Debye theory.

$$E(\theta) = \frac{k}{2}\int_{v_0}^{v_e} |\epsilon_{2,2}| \exp\left[-ik\Delta v + i\Phi_T(v)\right] dv \tag{4.39}$$

The integrals for the Airy theory with Φ_B, with $\Phi_B + A_F$ and the VCRM+PO are all

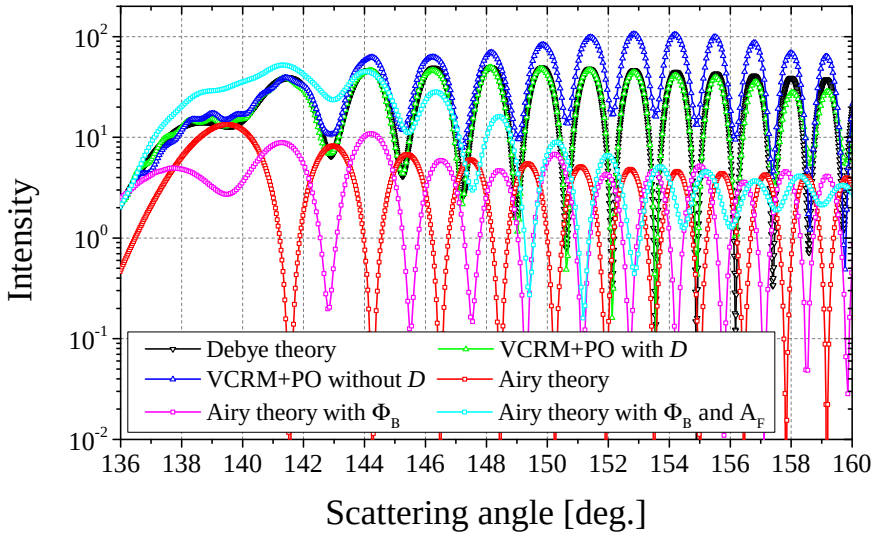

Figure 4.17 – Scattering diagrams of a circular cylinder near the primary rainbow angle in parallel polarization. The incident wave is a plane wave of wavelength with $\lambda = 0.6328$ μm. The particle size is $a = 50$ μm with refraction index $m = 1.333$.

evaluated by Hopkin's algorithm (see Appendix B). The number of the incident rays is 4000. The number of interpolation point for the scattering angle is 4000. The number of interpolation point for phase and amplitude is 300.

4.6 Rainbow diagrams of a spherical particle

We have discussed in Chapter 2 that the complex amplitude of an emergent ray from an infinite circular cylinder differs from that of a spherical particle in three points:

1 divergence factor: the ratio of the divergence factors of a sphere to that of an infinite cylinder is

$$\left(\frac{\sin\theta}{\sin\theta_R}\right)^{1/2}$$

2 phase due to the focal line: the spherical particle has a supplementary phase due to the focal line because of the cross of the rays on the symmetric plane given by Eq. (2.47)

3 divergence effect due to the cylindrical and the spherical waves.

Among these factors, the first two vary as function of the scattering angle and are to be considered in the calculation of the scattering diagram while the third varies

as function of the particle size parameter and independent of the scattering angle does not influence the profile of the scattering diagrams.

Though the scattering by a spherical particle is in three dimensions, the scattered complex amplitude calculated by the ray model is continuous in the direction perpendicular to the scattering plane (as pointed by Airy 1838). The diffraction effect is only necessary in one direction - in the scattering plane as done for the infinite cylinder in the two previous sections. The profiles of the scattering diagrams and the precision of different methods are similar to those of an infinite cylinder. On the other hand, a comparison of two typical scattering diagrams of an infinite cylinder and a sphere has been given in Chapter 2. We will hereby focus our attention to the examination of the scattering diagrams in the rainbow region of particle of different parameters, mainly the refractive index.

Table 4.3 – Angular positions of the primary θ_{R2} and secondary geometrical θ_{R3} rainbows, and the scattering angle corresponding to the Brewster angle for a spherical particle as function of the refractive index m (calculated by VCRMEll2D).

m	$\theta_{R3}(^\circ)$	$\theta_{R2}(^\circ)$	$\theta_B(^\circ)$
1.30	138.158	132.868	134.579
1.31	135.327	134.455	135.891
1.32	132.576	135.993	137.125
1.33	129.898	137.484	138.377
1.333	129.108	137.922	138.740
1.34	127.290	138.928	139.593
1.35	124.750	140.330	140.820

In Table 4.3, the rainbow angles θ_{R3} and θ_{R2} and Brewster's angle θ_B are calculated by the software VCRM2D+ [88]. We can find that the rainbow angles and Brewster's angle are sensitive to the refractive index m.

In Figures 4.18 and 4.19, the scattering diagrams in the rainbow region for perpendicular and parallel polarized wave of a sphere are shown by Debye theory, Airy theory, VCRM and VCRM+PO. In order to illustrate the contribution of every rays, the intensity of every rays are simulated by VCRM rather than its interference diagrams as it for an infinite circular cylinder.

For their accuracy of the different models for the sphere scattering with refractive index $m = 1.333$, similarly for an infinite circular cylinder in Figures 4.9 and 4.12, the scattering diagrams calculated by VCRM+PO are still more accurate than Airy theory and are in agreement with Debye theory both for primary rainbow and

secondary rainbow. In Figure 4.19 for the parallel polarization, we can further find the effect of Brewster's angle ($\theta_{R2} = 138.740°$) for primary rainbow as calculated in Table 4.3 that makes the opposite positions for the maximum and minimum compared with the perpendicular polarization. For the secondary rainbow, there is no effect of Brewster's angle near, which makes Airy theory still has a good accuracy of the peaks position [124].

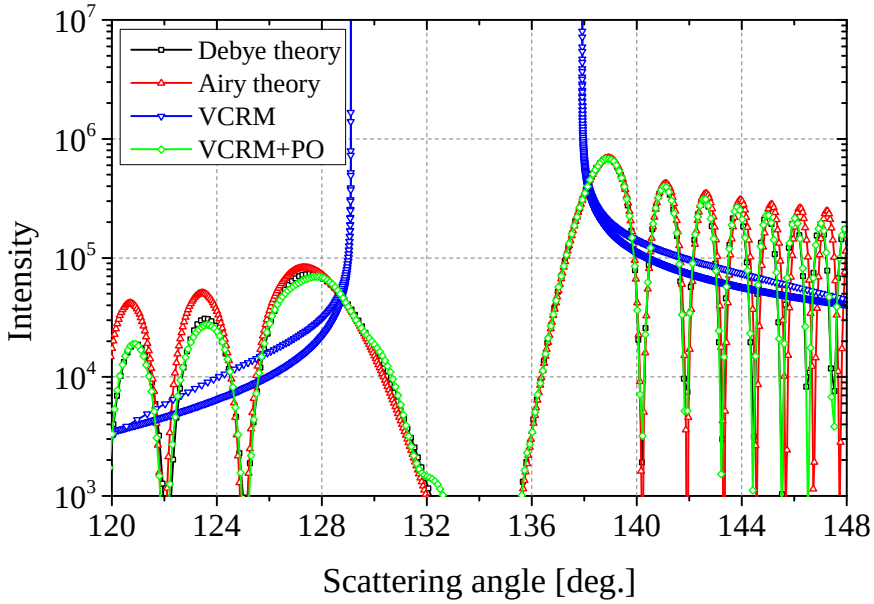

Figure 4.18 – Scattering diagrams of a sphere near the primary and secondary rainbows ($p = 2,3$) angle in perpendicular polarization. The incident wave is a plane wave of wavelength $\lambda = 0.6328$ μm. The particle size is $a = 100$ μm with refraction index $m = 1.333$.

For the light scattering by sphere with refractive index $m = 1.35$, their scattering diagrams are shown in Figures 4.20 and 4.21, similarly trends as the sphere with refractive index $m = 1.333$, but there is more long distance between the primary rainbow and secondary rainbow for the sphere with $m = 1.35$ compared with it in the scattering diagrams of the sphere with $m = 1.333$.

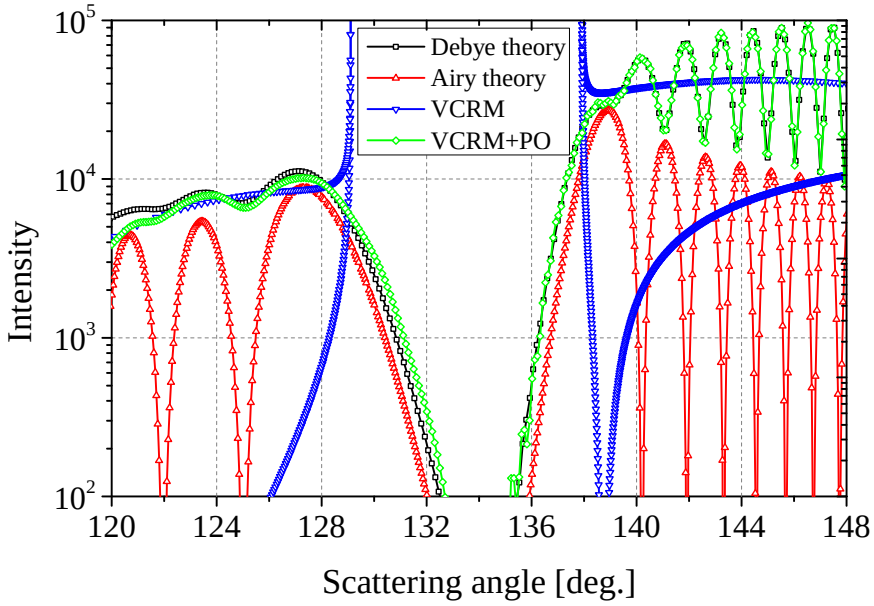

Figure 4.19 – Same parameters as Figure 4.18 but for the parallel polarization.

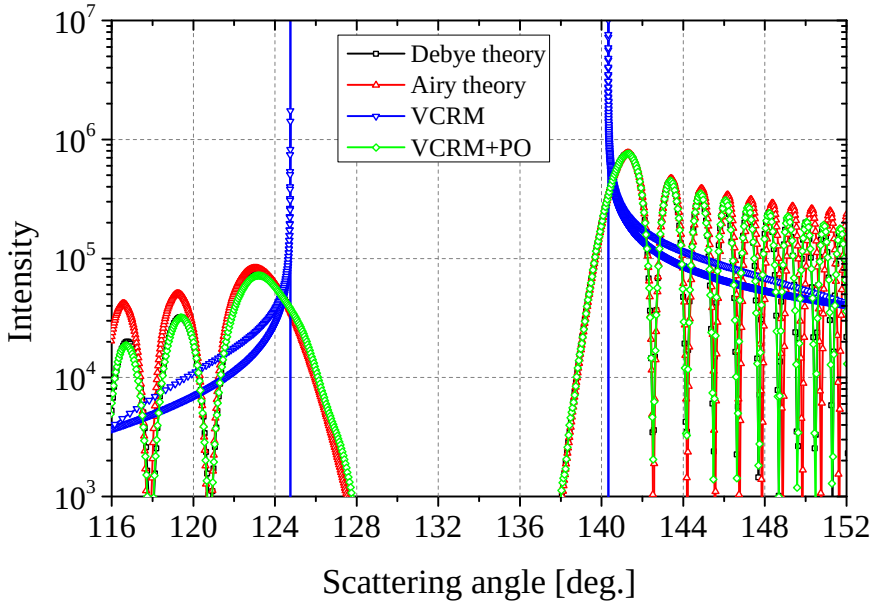

Figure 4.20 – Scattering diagrams of a sphere near the primary and secondary rainbows (p = 2,3) angle in perpendicular polarization. The incident wave is a plane wave of wavelength $\lambda = 0.6328$ μm. The particle size is $a = 100$ μm with refraction index $m = 1.35$.

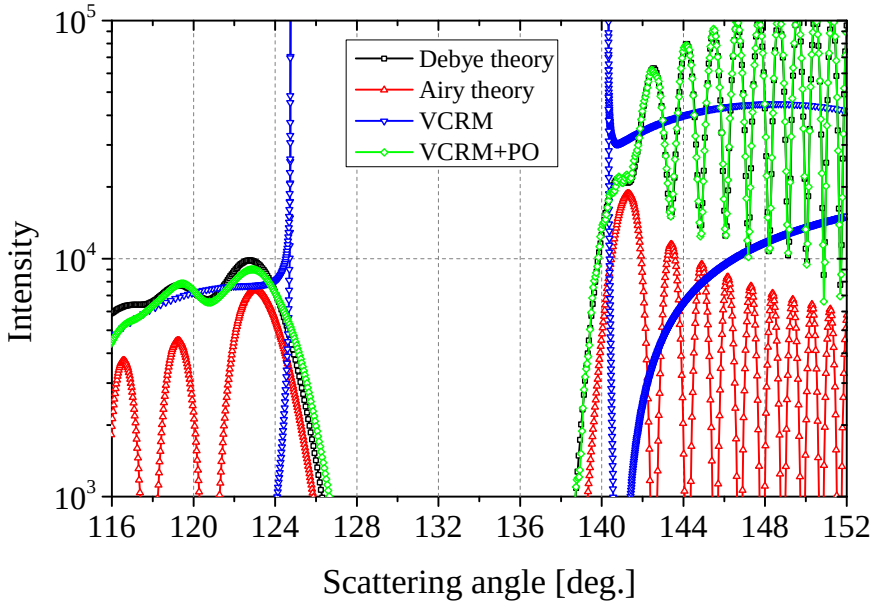

Figure 4.21 – Same parameters as Figure 4.20 but for the parallel polarization.

4.7 Summary

The Airy theory of rainbow has been reexamined in this chapter. We have shown that the size/wavelength dependent factor of the scattered intensity in Airy theory can be deduced rigorously. Then, by comparison with the scattering patterns of the rigorous Debye theory, we have examined in detail the influence of each factor in the calculation of the amplitude and the phase and their precision on prediction of the scattering patterns in the rainbow region. By replacing the constant amplitude and the cubic phase function in Airy theory by the those calculated with VCRM, our method can predict very precisely the scattering patterns in the neighborhood of rainbow in perpendicular or parallel polarization for a spherical particle from 10 μm to 1 mm (illuminated by visible light).

Chapter 5

Rainbow of a non-spherical particle

In Chapter 4, our method VCRM + PO has been developed for the study of the rainbow of a cylindrical and spherical particles. Thanks to the flexibility of the VCRM and PO, this method can be applied directly to a non-spherical particle. In this Chapter, we will demonstrate the applicability using an infinite elliptical cylinder and an ellipsoid as examples. The cases under study are limited to the scattering in the symmetric plane. So, the basic steps are similar to the circular cylinder and spherical particles scattering.

5.1 Rainbow of an infinite elliptical cylinder

For an infinite elliptical cylinder, the rainbow angle depends not only on the refractive index but also the ellipticity and the incident angle relative to a symmetric axis. In any case, the infinite intensity exists at the geometrical optics rainbow angle as shown in Figure 3.7. To solve this problem, the same approach VCRM + PO will be used. But the geometrical rainbow angle, the phase and the amplitude are calculated differently.

5.1.1 Rainbow angle and local orthogonal coordinate

For a non-spherical particle, such as an infinite elliptical cylinder, there is no analytical expression for the geometrical optics rainbow angle θ_R. So, it is calculated by numerically in looking for the extreme deviation angle by ray tracing.

As soon as θ_R is known, we define a local orthogonal coordinate $(O' : u, v)$. Similar to the Airy theory for a spherical particle, we define the axis u along the rainbow

ray and the coordinate v perpendicular to the rainbow ray and passing by the particle center O as shown in Figure 5.1. The complex amplitude of the emergent wave on this line will be calculated by using the VCRM and the scattering diagram in the rainbow region is calculated by the PO according to the field on the v line.

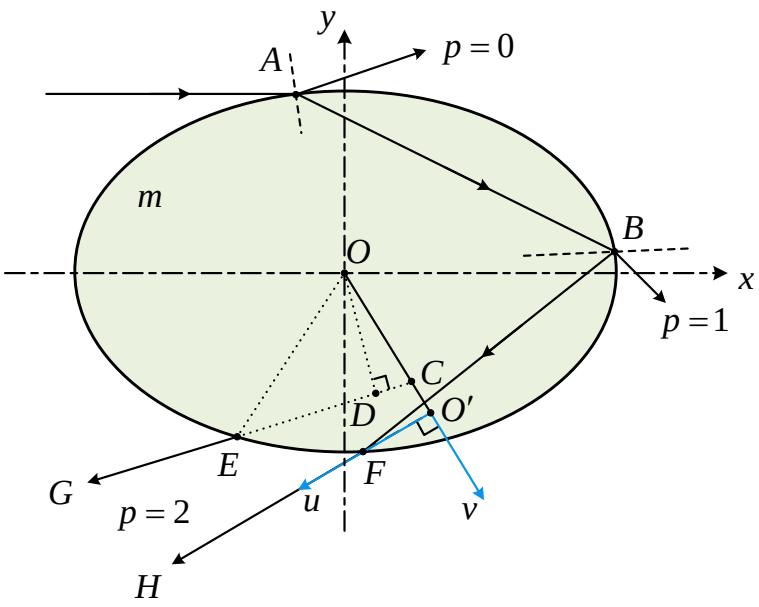

Figure 5.1 – The local orthogonal coordinate (O′ : u, v) in the rainbow region of an elliptical cylinder.

5.1.2 Amplitude and phase of emergent rays

In the local coordinate, the value v of an emergent ray is

$$v = \overline{\mathrm{OC}} - \overline{\mathrm{OO'}} \tag{5.1}$$

where $\overline{\mathrm{OC}}$ is

$$\overline{\mathrm{OC}} = \sqrt{x_v^2 + y_v^2} \tag{5.2}$$

The point C (x_v, y_v) is the intersection point of the emergent ray with the virtual line v. Its coordinates are calculated by

$$x_v = \frac{(x_e \tan\theta - y_e)\tan\theta_{\mathrm{R}}}{\tan\theta\tan\theta_{\mathrm{R}} - 1} \tag{5.3}$$

$$y_v = \frac{-x_v}{\tan\theta_{\mathrm{R}}} \tag{5.4}$$

The point E(x_e, y_e) is the emergent point of the ray and its coordinates are calculated in ray tracing by Eqs. (3.34).

When $\theta = \theta_R$, the point C is located at O′. So, the coordinate v of every emergent ray can be calculated by Eq. (5.1).

The phase on the virtual line v of an emergent ray is calculated by

$$\Phi(v) = \Phi_P + \Phi_F + \Phi_f + \Delta\Phi_{vir} - \Phi_R, \tag{5.5}$$

where Φ_P is the phase of optical path, Φ_F is the phase shift due to the Fresnel reflection coefficients and Φ_f the phase shift of focal lines while Φ_R is phase of the geometrical rainbow ray. $\Delta\Phi_{vir}$ is the supplementary phase due to the deviation the emergent ray relative to the geometrical rainbow ray and calculated by

$$\Delta\Phi_{vir} = k\overline{CD} \tag{5.6}$$

where the point D is the intersection point of the emergent ray $\overline{EG}$ and the virtual line $\overline{OD}$ which is perpendicular to $\overline{EG}$. According to the geometrical relationship, the coordinates of the point (x_D, y_D) are

$$x_D = \frac{(x_e \tan\theta - y_e)\tan\theta}{\tan^2\theta - 1} \tag{5.7}$$

$$y_D = \frac{-x_D}{\tan\theta} \tag{5.8}$$

So,

$$\overline{CD} = \sqrt{(x_v - x_D)^2 + (y_v - y_D)^2} \tag{5.9}$$

The amplitude on the virtual line is calculated by Eq. (4.22). Therefore, Eqs. (5.5) and (4.22) permit to calculate the complex amplitude (amplitude and the phase) of all the emergent rays.

In Figure 5.2, the phase of the rays $p = 2$ near the rainbow angle of an infinite elliptical cylinders are shown for three different aspect ratios. These phases are affected obviously by particle shape. Compared to the circular cylinder $a/b = 1.0$, the phase of the particle with $a/b = 0.95$ increases slowly and the phase of the particle $a/b = 1.05$ is increase rapidly as v increases. The difference in the shape of its wavefront will affect the angular spacing between two successive peeks as addressed in reference [64].

The amplitudes on the virtual line of the same particles are shown in Figure 5.3.

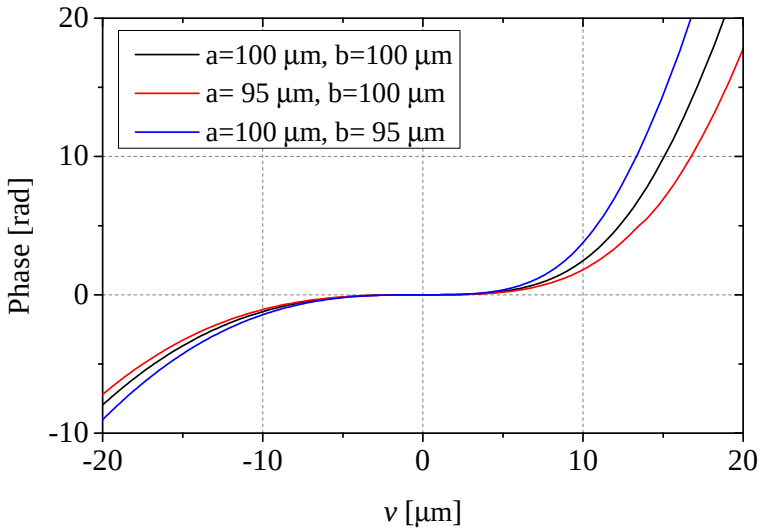

Figure 5.2 – Phase the rays $p = 2$ on the virtual line of an elliptical cylinder illuminated by a plane wave of wavelength $\lambda = 0.6328$ µm in perpendicular polarization. The relative refraction index of the particle is $m = 1.333$.

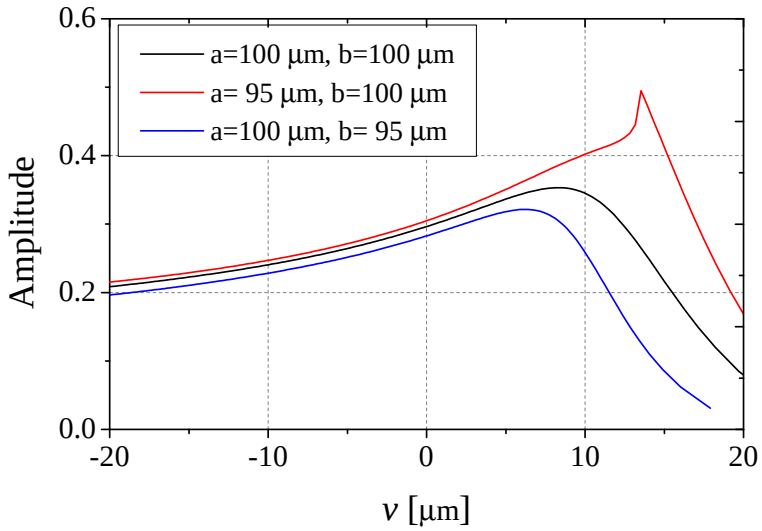

Figure 5.3 – Amplitude on the virtual line of an elliptical cylinder with the same parameters as Figure 5.2.

Compared to the circular cylinder $a/c = 1.0$, the amplitude of the particle $a/b = 0.95$ is bigger and the amplitude of the particle $a/b \approx 1.05$ is smaller. Besides, for the particle $a/b = 0.95$, there is a peak near $v = 13.5$ µm, this peak is caused by total reflection according to Figure 2.3 . At the same point, a phase shift Φ_F occurs according to Figure 2.5, so, there is a small variation in Figure 5.2 in the region $v >$ 13.5 µm. This phenomenon also occurs in parallel polarization in Figure 5.4 and it

is more easy to observed.

The phases near the rainbow angle for the parallel polarization are shown in Figure 5.4. The most important difference from the perpendicular polarization is the phase jump of π in the Brewster angle. The point moves because the Brewster angle varies as function of the particle shape. Similar to the circular cylinder, the scattering diagram for the parallel polarization will be very different from that for the perpendicular polarization due to the phase jump.

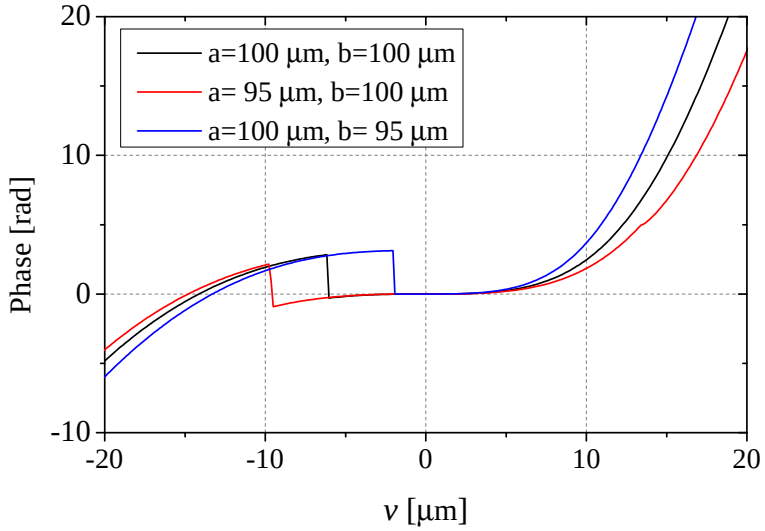

Figure 5.4 – Phase on the virtual line of an elliptical cylinder with same parameters as Figure 5.2 but the incident wave is in the parallel polarization.

The amplitude on the virtual line for the parallel polarization are shown in Figure 5.5. For the particle $a/b = 0.95$, there is a peak near $v = 13.5$ µm, same as the perpendicular polarization. At Brewster angles θ_B, the amplitude on the virtual line equals zero. These points are of course located at the same positions where the phase jump of π occurs in Figure 5.4.

5.1.3 Scattering diagrams of an elliptical cylinder

After the phase and the amplitude are computed on the virtual line, the diffraction field is calculated by Eq. (4.30). We rewrite it here for a cylinder as

$$\mathrm{E}(\theta) = \frac{k}{2}\int_{v_0}^{v_1} |\epsilon_{X,p}|\sqrt{\mathcal{D}_{2,vir}}\exp\left[i\Phi_T(v)\right]dv \tag{5.10}$$

The scattering diagrams in the neighborhood of the primary rainbow angle of

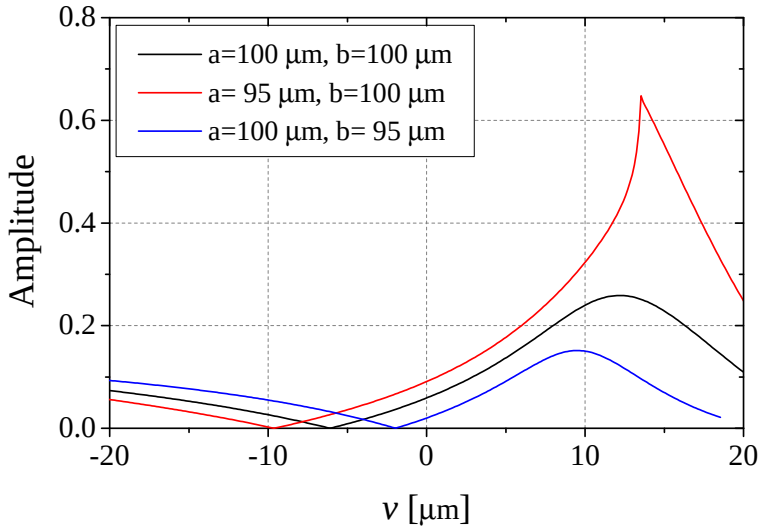

Figure 5.5 – Same parameters as Figure 5.2 but incident wave is in parallel polarization.

two infinite elliptical cylinders calculated by Eq. (5.10) are shown in Figures 5.6 to 5.9, of which Figures 5.6 and 5.7 are for the perpendicular polarization and 5.8 are 5.9 for the parallel polarization.

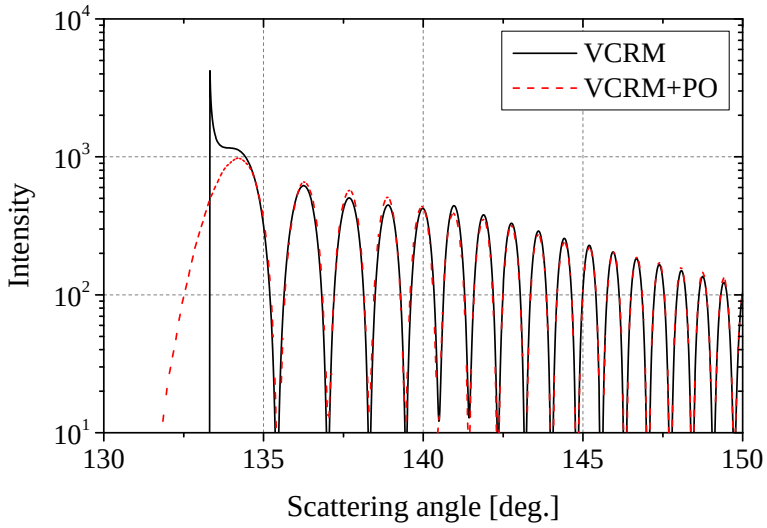

Figure 5.6 – Scatting diagrams of an infinite elliptical cylinder near rainbow region with particle size in $a = 95$ μm, $b = 100$ μm and wave in perpendicular polarization for $p = 2$.

We find that in the perpendicular polarization, the intensity calculated by the VCRM is in good agreement with tat calculated by VCRM+PO except in the main supernumerary bow. But for the parallel polarization, the infinite elliptical cylinder particle with $a/b = 0.95$, this agreement can only be found after about 143° in Fig-

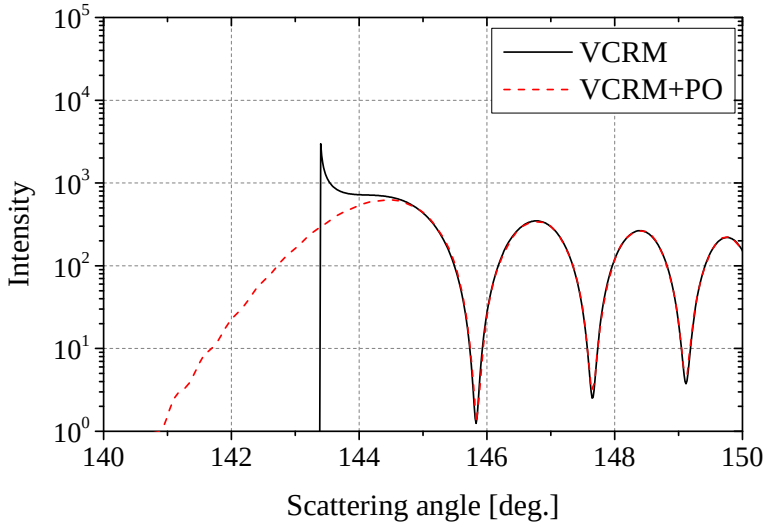

Figure 5.7 – Scatting diagrams of an infinite elliptical cylinder in the rainbow region, same parameters with Figure (5.6) except $a = 100$ μm, $b = 95$ μm.

ure 5.8 because the amplitude varies rapidly increasing near the rainbow angle and rapidly decreasing near the Brewster angle. So the diffraction effect is important.

In Figure 5.9, still as previous scattering diagrams in parallel polarization, VCRM and VCRM+PO are in agreement except that VCRM fails at rainbow angle, and it has opposite positions for maximum and minimum compared with perpendicular polarization.

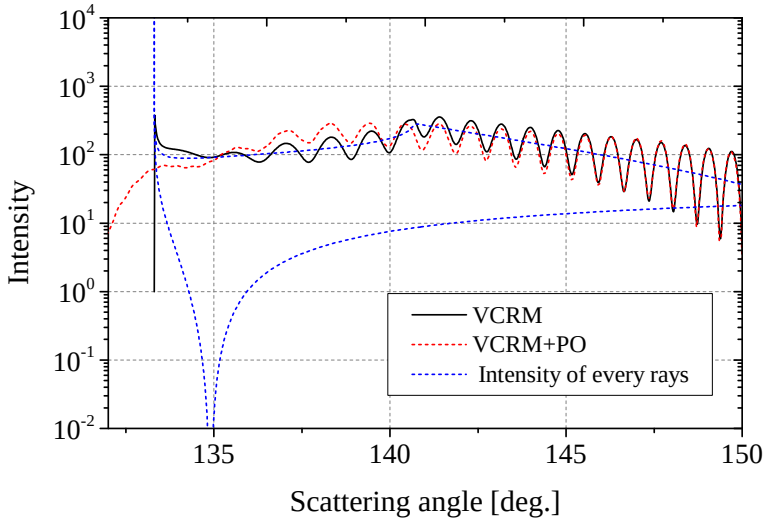

Figure 5.8 – Scatting diagrams of an elliptical cylinder near rainbow region with particle size in $a = 95$ μm, $b = 100$ μm and wave in parallel polarization for $p = 2$.

Further, we find that the distance between the supernumerary bows are very

sensible to the particle shape, the for particle $a/b = 0.95$ (Figures 5.6 and 5.8) has much more supernumerary bows than the particle $a/b = 0.95$ (Figures 5.7 and 5.9). This can be understood according to the variation of the shape for wavefront given in Figures 5.2.

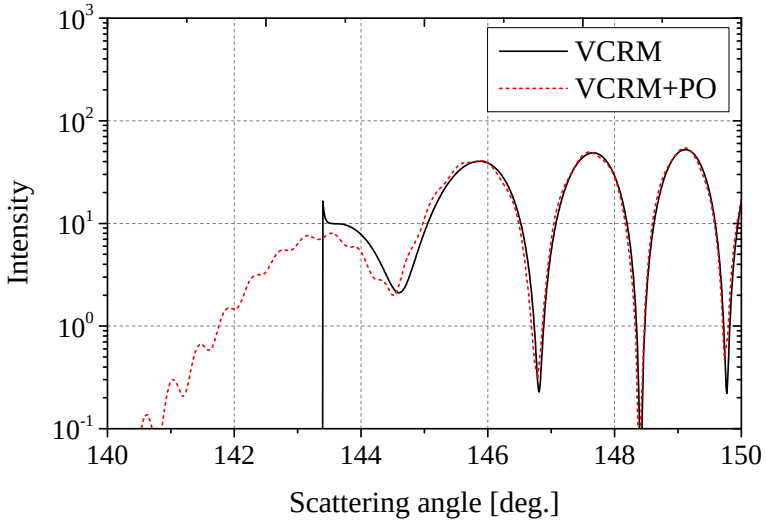

Figure 5.9 – Scatting diagrams of an elliptical cylinder near rainbow region, same parameters with Figure (5.8) except $a = 100\mu m, b = 95\mu m$.

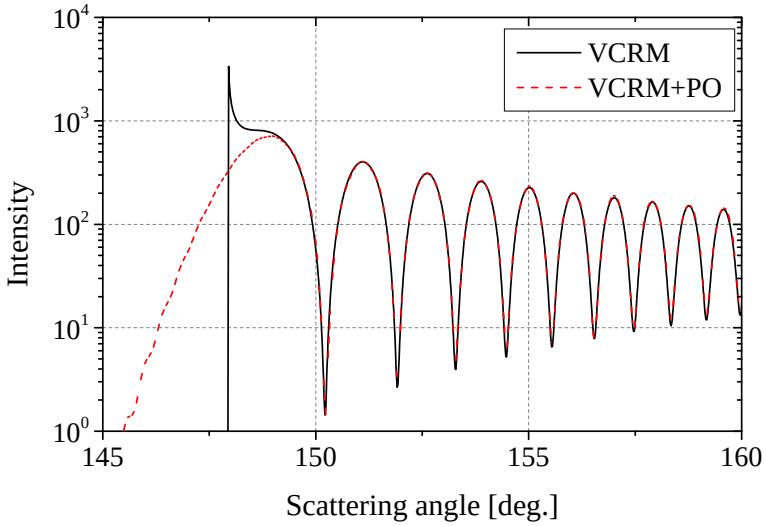

Figure 5.10 – Scattering diagrams of an infinite elliptical cylinder. The parameters are the same as Figure 5.7 but the refractive index $m = 1.362$.

To illustrate the influence of the refractive index on the scattering diagram of an infinite elliptical particle, we show in Figure 5.10 scattering diagram calculated by

VCRM and VCRM+PO for the same particle as in Figure 5.7 with refraction index $m = 1.362$. We find that the spacing between the supernumerary bows are smaller for a higher refractive index. This conclusion is also true for the parallel polarization.

5.2 Scattering diagrams of an ellipsoid

The light scattering diagrams in rainbow region of an ellipsoid – a 3D particle, are still calculated by Eq. (4.30), we rewrite it here as

$$\begin{aligned} \mathrm{E}(\theta) = & k^{3/2} \int_{v_0}^{v_1} |\epsilon_{\mathrm{X},p}| \sqrt{\left| \frac{\mathrm{R}'_{1,1}}{\mathrm{R}_{1,2}} \cdot \frac{\mathrm{R}'_{1,2}}{\mathrm{R}_{1,3}} \cdots \frac{\mathrm{R}'_{1,p}}{\mathrm{R}_{1,p+1}} \mathrm{R}^{e}_{1,p+1} \right|} \\ & \sqrt{\left| \frac{\mathrm{R}'_{2,1}}{\mathrm{R}_{2,2}} \cdot \frac{\mathrm{R}'_{2,2}}{\mathrm{R}_{2,3}} \cdots \frac{\mathrm{R}^{e}_{2,p+1}}{(\mathrm{R}^{e}_{2,p+1} + d_{vir})} \right|} \exp\left[i\Phi_{\mathrm{T}}(v) \right] dv, \end{aligned} \tag{5.11}$$

But different from it in Eq. (4.30), the Fresnel factor $\epsilon_{\mathrm{X},p}$ and phase $\Phi_{\mathrm{T}}(v)$ are calculated with the same rules as for an infinite elliptical cylinder in the previous section.

Since the reflection, the refraction, the divergence due to the curvature of the particle surface on the the equatorial plane of an ellipsoidal particle are the same as those of an elliptical cylinder of the same cross section, we will focus our analyse on the effect of the value of c – the axis along z (perpendicular to the scattering plane). So, we consider two categories of ellipsoids: prolate and oblate ellipsoids.

5.2.1 Scattering diagrams of a prolate ellipsoid

The comparisons of the scattering diagrams in perpendicular and parallel polarizations for a propate ellipsoid are shown in Figures 5.11 and 5.12, we can find that VCRM+PO and VCRM are in agreement except that VCRM fails near the rainbow angle same as in spherical particles.

In order to further study the effect of the parameter c to the scattering diagrams, the scattering diagrams in the rainbow region of three prolate ellipsoids for the perpendicular and the parallel polarizations are shown in Figures 5.13 and 5.14. We find that the scattering diagrams are similar trend to those of an circular cylinder due to the same cross section, i.e. same a and b since Φ_{P} and $\epsilon_{\mathrm{X},p}$ are the same. As the c increases from 110 μm to 200 μm, the intensity decrease initially and then increases. In order to explain this phenomenon, the amplitude of every individual

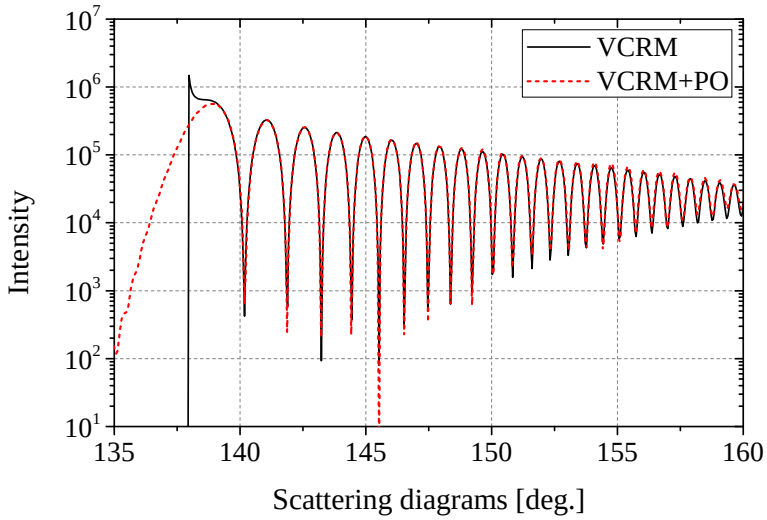

Figure 5.11 – The scattering diagrams of three prolate ellipsoid in the perpendicular polarization. The axes of the ellipsoid are $a = b = 100$ μm, and $c = 120$ μm. The refractive index is $m = 1.333$. The wavelength the incident plane wave is $\lambda = 0.6328$ μm.

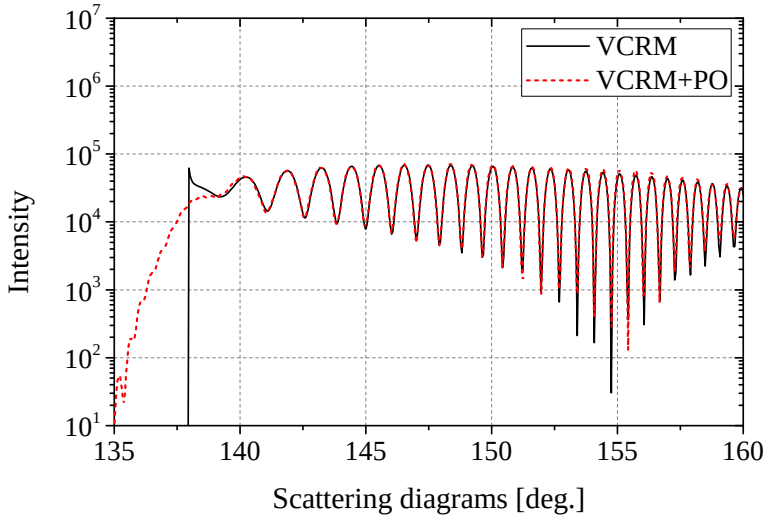

Figure 5.12 – The scattering diagrams of the prolate ellipsoid. Same parameters as in Figure 5.11 except in parallel polarization.

rays near rainbow angle are shown in Figures 5.15 and 5.16 for 5 different values of c and zoomed in angle ranges [140°, 141°] and [149°, 150°] respectively.

In Figure 5.15, we find that in the range of $\theta \in [140°, 141°]$ as c increases from 110 μm, the amplitude of its bigger branch decreases until near $c = 130$ μm, its small branch decreases until near $c = 120$ μm. While in Figure 5.16, in the range $\theta \in [149.0, 150.0]$, as c increases from 110 μm, the amplitude of its bigger branch

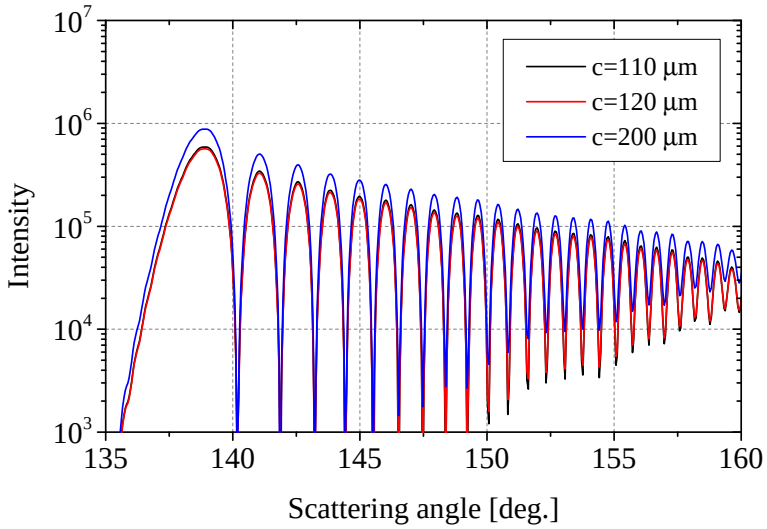

Figure 5.13 – The scattering diagrams of three prolate ellipsoids for the perpendicular polarization. The axes of the ellipsoid are $a = b = 100$ μm, and $c = 110$ μm, $c = 120$ μm and $c = 200$ μm. The refractive index is $m = 1.333$. The wavelength the incident plane wave is $\lambda = 0.6328$ μm.

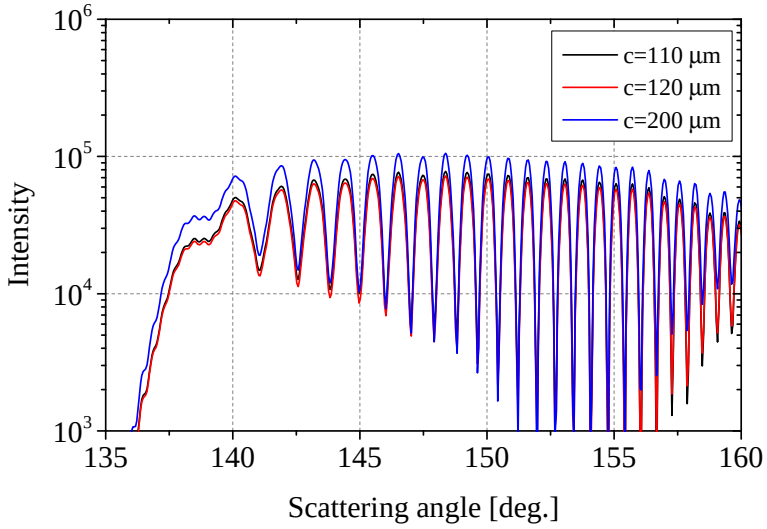

Figure 5.14 – Scattering diagrams of a prolate ellipsoid near rainbow region. Same parameters as in Figure 5.13 but in parallel polarization.

(This bigger branch is the small branch in $\theta \in [140.0, 141.0]$) decreases until near $c = 120$ μm, its smaller branch (This smaller branch is the bigger branch in $\theta \in [140.0, 141.0]$) decreases until near $c = 130$ μm.

So, according to the trends of the amplitude of every ray in the two branches, the scattering intensity decreases and reaches a minimum near $c \in [120\ \mu m, 130\ \mu m]$(an

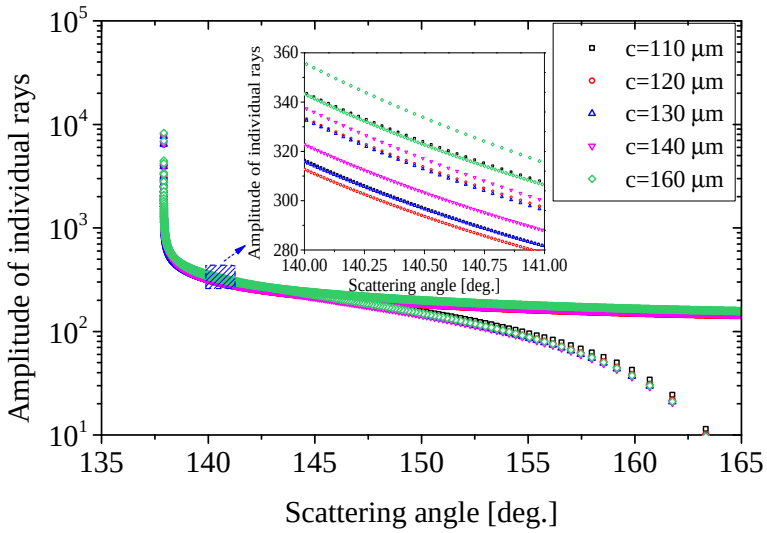

Figure 5.15 – Amplitude of the individual rays $p = 2$ of an prolate ellipsoid near rainbow. Same parameters as in Figure 5.13.

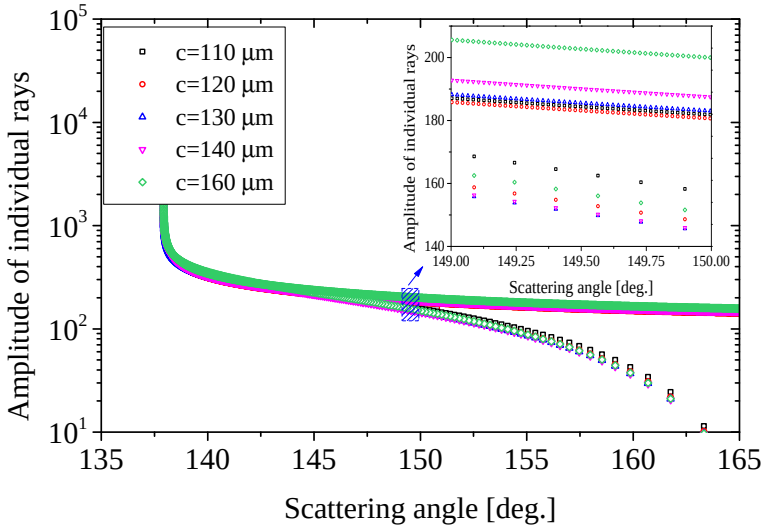

Figure 5.16 – Amplitude of the individual rays $p = 2$ of an prolate ellipsoid near rainbow. Same parameters as in Figure 5.13.

approximation region). This makes the decrease of intensity as c increase. As c bigger than 130 μm, the intensity of all the rays in two branches increases. So, in Figures 5.13 and 5.14, the intensity of the prolate ellipsoid $c = 110$ μm is bigger than $c = 120$ μm and smaller than $c = 200$ μm on the whole.

5.2.2 Scattering diagrams of an oblate ellipsoid

The scattering diagrams in the perpendicular polarization of two oblate spheroidal particles ($a = b = 100$ μm, $c = 90$ μm and 87 μm) calculated by VCRM+PO and VCRM are shown in Figure 5.17. The other parameters are the same as in Figure 5.13.

When $c = 90$ μm, there are obvious differences between VCRM and VCRM + PO near rainbow angle and in the range $\theta \in [153°, 160°]$. It becomes more obvious for $c = 87$ μm. In Figure 5.18, the scattering diagrams of the same particles for the parallel polarization are shown. Similar to the perpendicular polarization, there are obvious discrepancies between VCRM and VCRM + PO.

In order to find the reason of these differences, the amplitude of the individual rays calculated by VCRM are shown in Figure 5.19. As c decrease from 90 μm to

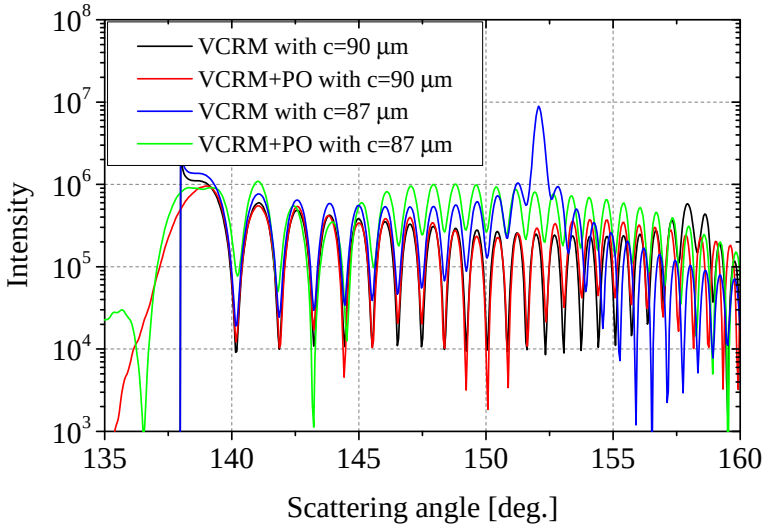

Figure 5.17 – The scattering diagrams of an oblate spheroid in perpendicular polarization near rainbow region, same parameters as in Figure 5.13 but different in $c = 87$ μm and $c = 90$ μm.

87 μm, there is another caustics caused by the curvature radii of the wavefront in perpendicular plane. As $c = 90$ μm, there is a caustic near $\theta = 158°$, as c becomes smaller, a caustics removes gradually to the rainbow angle. In order to find out what happened at these caustics directions detailed, part of data for the curvature radii of the wavefront in perpendicular plane are shown in Table 5.1.

As $c = 80$ μm, we can find that the caustics direction in perpendicular plane is between $\theta \in [140.5195°, 140.5372°]$ (see Table 5.1 and Figure 5.19), its divergence factor $D^e_{1,2}$ at its emergent point is the constant 1. The emergent curvature radii $R^e_{1,3}$

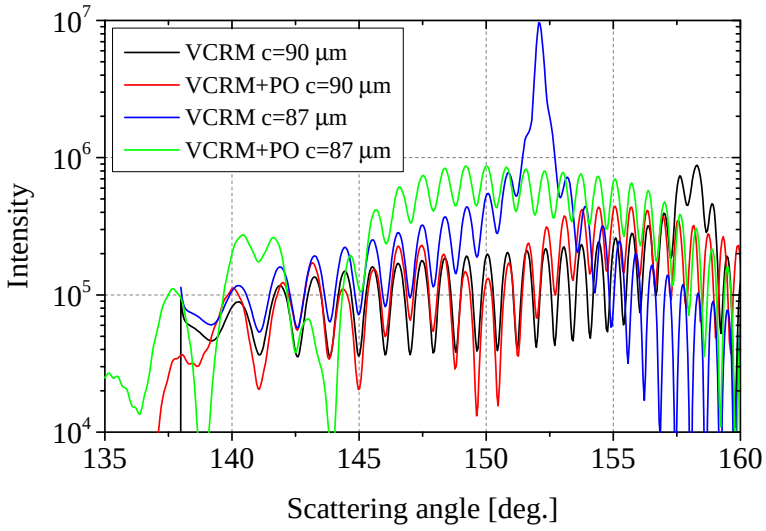

Figure 5.18 – The scattering field of an oblate spheroid in parallel polarization near rainbow region. Same other parameters as in Figure 5.17.

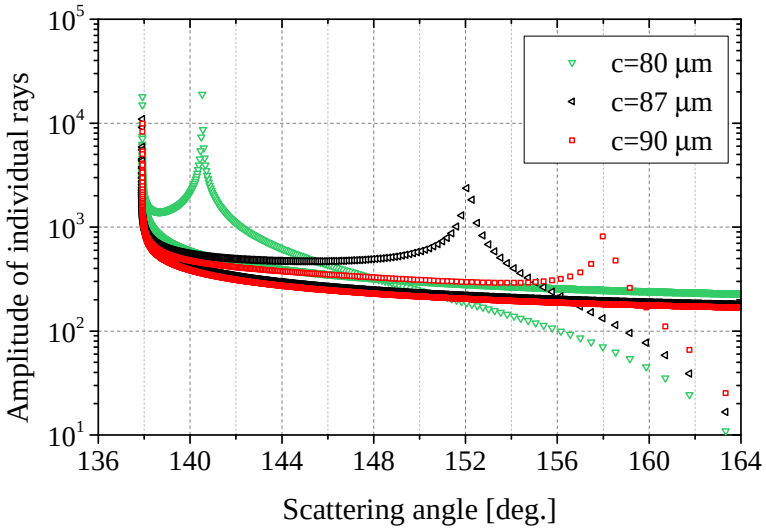

Figure 5.19 – The scattering field of an oblate spheroid near rainbow region, same parameters as in Figure 5.17.

reaches to ∞ (or $-\infty$). These characters are same with Table 4.1 for the caustic in spherical particles in parallel plane. So, according to Table 5.1 and the Figure 5.19, we can conclude that the infinite emergent curvature radii at caustics directions makes VCRM and VCRM + PO failed by the Eq. (5.11). Therefore, for the light scattering of oblate ellipsoid near its rainbow region, the another method to combining VCRM and PO should be studied further to avoid the infinite emergent curvature in perpendicular plane.

Table 5.1 – Curvature radius in perpendicular plane of $p = 2$ for the particle $a = b = 100$ µm, $c = 80$ µm near the caustics. The relative refraction index of the particle is $m = 1.333$, the number of incident ray is 10000 here.

Angles	$R'_{1,1}$ (µm)	$R_{1,2}$ (µm)	$R'_{1,2}$ (µm)	$R_{1,3}$ (µm)	$R^e_{1,3}$ (µm)	$\mathcal{D}^e_{1,2}$
140.5549°	142.0302	-0.059164	-0.059239	-142.1486	127919.9	1.000433
140.5372°	142.1114	-0.007698	-0.007699	-142.1268	984039.6	1.000039
140.5195°	142.1924	0.043663	0.043621	-142.1052	-173668.9	0.999651
140.5020°	142.2734	0.094923	0.094723	-142.0837	-79963.7	0.999225

5.3 Summary

The method VCRM+PO has been applied in this chapter to the prediction of the scattering patterns in the rainbow region of a non-spherical particles like infinite elliptical cylinder and ellipsoid. The convergence effect and the cusp position as function of the vertical radius of the particle have been highlighted. However, the effective rays near the rainbow angle depend on the shape of the particle, the integral limits used for the spherical particle are to be adjusted. Therefore, VCRM+PO is a powerful method for light scattering by large spherical or non-spherical particles. It can also be used in the scattering of an electromagnetic wave or an acoustics wave.

Chapter 6

Conclusions and Perspectives

This thesis is devoted to combining the Vectorial Complex Ray Model (VCRM) with the Physical Optics (PO) for the calculation of the scattering diagrams of a large particle with smooth surface in the rainbow region. This chapter draws the conclusions of this thesis and gives perspectives in the following studies.

6.1 Conclusions

For light scattering by a large non-spherical particle, there is no rigorous solution like Lorenz-Mie Theory for spherical particles. The numerical methods such as DDA, FDTD, MLFMA and T-matrix can deal with this problem, but they are time consuming and require huge computer memory. The particle size is also limited. The approximate models are feasible ways owning to its efficiency and flexibility.

The geometrical optics (GO) is based on ray model. Usually it does not take into account the variation of the amplitude and phase along the optical path, except in the special case of scattering of a plane wave by a sphere or an infinite circular cylinder. To extend the ray model to light scattering by a large particle, especially when it is non-spherical particle with smooth surface, the VCRM has been developed in the laboratory. After more than a decade in development, it has been validated numerically and experimentally and applied to the light scattering by an infinite cylinder (VCRM2D), the scattering in a symmetric plane of a 3D particle (VCRM2D+) such as ellipsoidal particle or a pendant drop in the horizontal plane and the scattering in all space by a 3D particle (VCRM3D).

However, as an intrinsic flaw of the ray model, the VCRM fails to predict correctly the scattering in the neighborhood of a singular point, i.e. where the intensity

or the derivative of the intensity is not continuous, for example in forward direction, near rainbow angles or critical angles. To remedy this problem, the Physical Optics (PO) can be applied. The Airy theory is a typical, well known and perhaps the most successful example in this spirit of combining GO and PO. It does work well in predicting the scattered intensity in the first supernumerary bows of a spherical water drop in the perpendicular polarization. But the peak positions and the scattered intensity differ more and more from those of the rigorous Debye theory when the scattering angle is far from the geometrical rainbow angle. Furthermore, the Airy theory fails completely in the prediction of the scattered intensity for the parallel polarization. To understand the reason, the Airy theory has been reexamined in details and it is found that the flaws of the Airy theory mentioned above are due to its approximations in the calculation of the phase and the amplitude.

The VCRM has been applied to calculate the amplitude and the phase on the v line used in the Airy theory for a spherical particle. It is found that the amplitude on the v line is affected by both the Fresnel factor and the divergence factor, and the cubic function of phase is approximately true in the neighborhood of the geometrical rainbow angle. The strong amplitude variation and the phase jump of π at the Brewster angle for the primary rainbow are the main cause of the failure of the Airy theory in the case of the parallel polarization. Since the amplitude and the phase can be calculated rigorously by VCRM, the influences of all the factors mentioned above on the scattering diagrams have been studied in details. It is proved that the combination VCRM and PO can predict very precisely the scattering diagrams in both perpendicular and parallel polarizations when compared with Debye theory. The numerical results are exemplified by the scattering diagrams in the rainbow region for an infinite circular cylinder and a sphere of radius from 10 μm to 1 mm (illuminated by visible light).

VCRM being flexible to particle shape, the developed VCRM+PO method has been applied to the scattering of an infinite elliptical cylinder and an ellipsoidal particle. The scattering patterns in the rainbow region of the elliptical cylinder are similar to those of the circular cylinder while the rainbow positions are very sensible to the ellipticity of the cylinder. The effect of the aspect ratio of a prolate spheroid on the intensity ratio of the two first rainbows have been studied. However, it seems that the actual version of VCRM+PO is not robust enough predict the scattering diagram near the peak caused by the focusing effect of the short axis.

6.2 Perspectives

This thesis is the first attempt to include the diffraction effect in the VCRM in order to correct the scattering diagram in the neighborhood of the rainbow angle (caustics). Only the light scattering in a symmetric plane is considered. The interpolation of the amplitude and the phase of the emergent rays as well as the diffraction integration are all in one dimension. This simple case permit us to focus our attention on the understanding the physical mechanism. But the scattering problems in the real world are usually in three dimensions. So it is necessary to extend the VCRM+PO to three dimension scattering. To this end, the first work to be undertaken should be the development of ray tracing process [125] and interpolation algorithm of the VCRM for the scattering of a particle of any shape described by an analytical mathematical equations or by discrete data. The 3D structure of the caustics and the their diffraction effect are then to be studied.

In this thesis, our attention is limited to light region which is part of electromagnetic wave. In fact, our models can be extended to other regions like Terahertz region, microwave region [126–128]. Further, our models might be applicable to the acoustic wave scattering, similar applications are deserved to research further.

The freeform optics is an emerging technology for imaging and non-imaging [129], the VCRM+PO is a useful tool to find a better curve surface for controlling of light propagation, because they are applicable to interaction of light with any smooth surfaces.

The incident wave is limited to the plane wave in this thesis. In fact, our models can be applied directly to non-plane waves like Gaussian beams, or the beams carrying orbital angular momentum [28, 130–132]. The scattering diagrams of these shape beams can provide more information about the scatters. Our method can also be applied to time domain as shown in [133, 134]. Therefore, the VCRM and the combining model VCRM+PO will have more applications in the future [56, 124].

Appendix A

Evaluation of Airy function

The Airy function Ai had been introduced by Airy for the calculation of the scattering intensity in the neighborhood of a caustic (rainbow angle) [3]. It is defined as [77]

$$\mathrm{A}i(x) = \frac{1}{\pi}\int_0^\infty \cos\left(\frac{t^3}{3} + xt\right) dt \tag{A.1}$$

Its properties and the numerical calculation have been largely studied by physicians and mathematicians. A typical variation of the function is shown in Figure A.1 (black solid line).

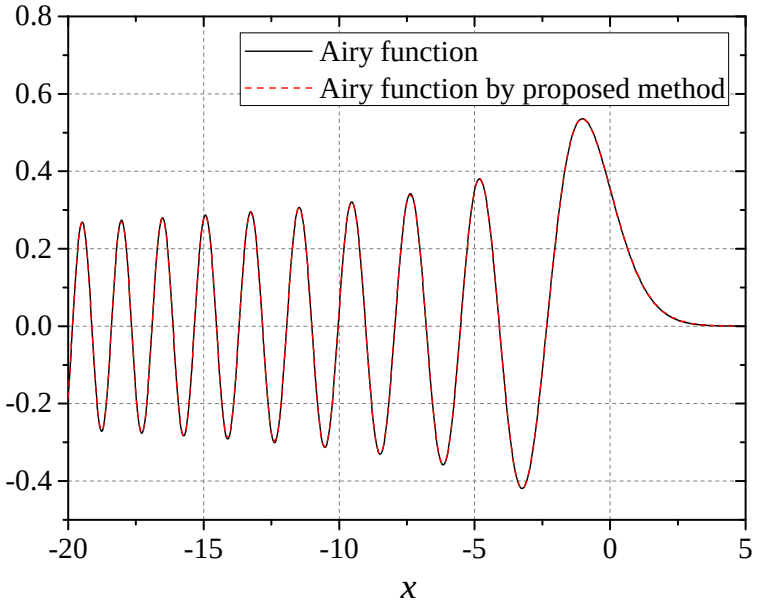

Figure A.1 – The plot of Airy function.

However, the numerical evaluation of this integration is not a easy task, espe-

cially when the variable x is large. Furthermore, this function can only be applied to the case where the phase along the virtual line (see Eq. (4.11)) is a cubic function. Even the constant phase jump of π in the Brewster angle for parallel polarization in Eq. (4.34) can not be dealt with directly.

On the other hand, we have shown in Chapter 4 that the cubic function is valid only in the region very near the GO rainbow angle. In our study, we need to evaluate the integration for a phase different from a cubic function; As a first step, we consider the integration little more general than the Airy function, i.e.

$$\mathrm{A}(x) = \frac{1}{\pi}\int_a^y \cos\left(\frac{t^3}{3} + c_0 + xt\right) dt \tag{A.2}$$

where a and c_0 are two constants. In the case of Airy function, we have $a = 0$, $c_0 = 0$ and $y = \infty$. For the phase given as a piece function (Eq. (4.35)), a corresponds to v_B, $c_0 = 0$, or π according to the piece under consideration.

To evaluate numerically the integration, we consider firstly that the contribution in the range of large value t is small because of the strong oscillation of the integrand. So we do not need to integrate to infinity. Instead, we choose the upper limit of integration as as a multiple number of 2π, i.e.

$$\Phi(t) = 2\mathrm{N}\pi = \frac{t^3}{3} + xt + c_0. \tag{A.3}$$

Eq. (A.3) may be rewritten as

$$y^3 + py + q = 0 \tag{A.4}$$

where $p = 3x$ and $q = 3c_0 - 6\mathrm{N}\pi$, N is an integer. This integral calculate the main contribution of the integrand to $\mathrm{A}(x)$. So, the upper limit y is decided by the root of Eq. (A.4) i.e. [135]

$$y = \sqrt[3]{-\frac{q}{2} + \sqrt{\frac{q^2}{4} + \frac{p^3}{27}}} + \sqrt[3]{-\frac{q}{2} - \sqrt{\frac{q^2}{4} + \frac{p^3}{27}}} \tag{A.5}$$

To check the proposed method, we compare in Figure A.1 and in Table A.1 the standard Airy function and that calculated by the proposed method with $a = c_0 = 0$. In our calculation, N = 100 is accurate enough. We find that the errors between Airy theory and proposed method is less than 0.001. So, this proposed method is applicable to our calculation.

Table A.1 – Comparisons of the standard Airy function with the results calculated by the proposed method.

x	-10.00	-5.00	0.00	5.00
Airy function	0.040241	0.350761	0.355028	0.000108
Proposed method	0.040464	0.350927	0.355075	0.000194

This method has been applied to the calculation the scattering diagram in the neighborhood of the rainbow angle by taken into account the phase jump of π in the Brewster angle, i.e. the Airy theory with Φ_B (Eq. (4.35)). The comparison of the Airy theory with and without the phase jump to the Debye theory is given in Figure A.2. It is clear the Airy theory with the phase jump of π permits to correct the minima-maxima inverse of the supernumerary bows in the Airy theory. But the intensity is still about one order of magnitude smaller than the Debye theory and the peak position differs more and more with the scattering angle: the last minimum of Debye theory is at 149° but 149.4° for the corrected Airy theory. To address these problems, the precise calculations of the amplitude and the phase are necessary (see Chapter 4).

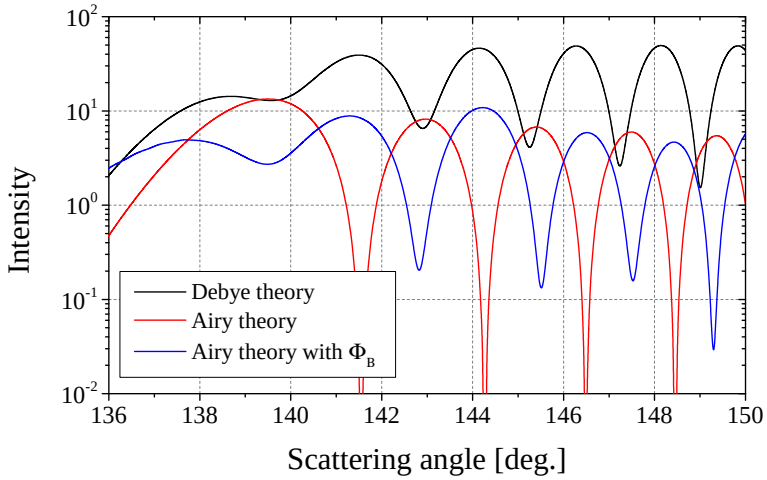

Figure A.2 – Comparison of the scattering diagrams in the neighborhood of the primary rainbow ($p = 2$) with the parallel polarization calculated by the Debye theory, the Airy theory and the the Airy theory with phase jump. The particle is an infinite circular cylinder of radius $a = 50$ μm, refractive index $m = 1.333$ illuminated normally by a plane wave of wavelength $\lambda = 0.6328$ μm.

But this method can not be applied to the phase function in other form (different from the cubic function). An algorithm for more general case – Hopkins' algorithm will be presented in Appendix B.

Appendix B

Hopkins' integral method

Consider the integral given by

$$\mathrm{I} = \int_{x_a}^{x_b} g(x)\exp[if(x)]dx \tag{B.1}$$

where x_a and x_b are the lower and upper integral limits, $g(x)$ and $f(x)$ are two slowly varying functions, and can be considered respectively as the amplitude and the phase function in the scattering problem. When $f(x)$ is relatively large, the integrand is a strongly oscillation function and the direct numerical evaluation of the integral is very difficult, even impossible.

Hopkins [136] proposed to linearize the phase function $f(x)$ in each subdivision, such that Eq. (B.1) is written in the form

$$\begin{aligned}\mathrm{I} &\approx \sum_{m=1}^{\mathrm{M}} g(x_m) \int_{x_m-\frac{1}{2}\delta_{xm}}^{x_m+\frac{1}{2}\delta_{xm}} \exp\{i[f(x_m)+f_x(x_m)(x-x_m)]\}dx \\ &= \sum_{m=1}^{\mathrm{M}} \delta_{xm} g(x_m)\exp[if(x_m)]\mathrm{sinc}[\frac{1}{2}\delta_{xm}f_x(x_m)]\end{aligned} \tag{B.2}$$

where M is the number of subdivisions, δ_{xm} the width of m^{th} division. f_x is the partial derivative with respect to x. $\mathrm{sinc}(t)$ is the sinc function defined by $\mathrm{sinc}(t) = \frac{\sin(t)}{t}$. x_m is the coordinate of m^{th} division.

Attention should be paid to the definition of x_m (cf Figure B.1):

$$x_m = x_a + mdx - dx/2, \qquad m = 1\ldots\mathrm{M} \tag{B.3}$$

If x_m is chosen as [136]

$$x_m = x_a + mdx, \qquad m = 1 \ldots \mathrm{M} \tag{B.4}$$

or

$$x_m = x_a + mdx, \qquad m = 0 \ldots \mathrm{M} - 1 \tag{B.5}$$

the precision is not good and depends much on the subdivision number.

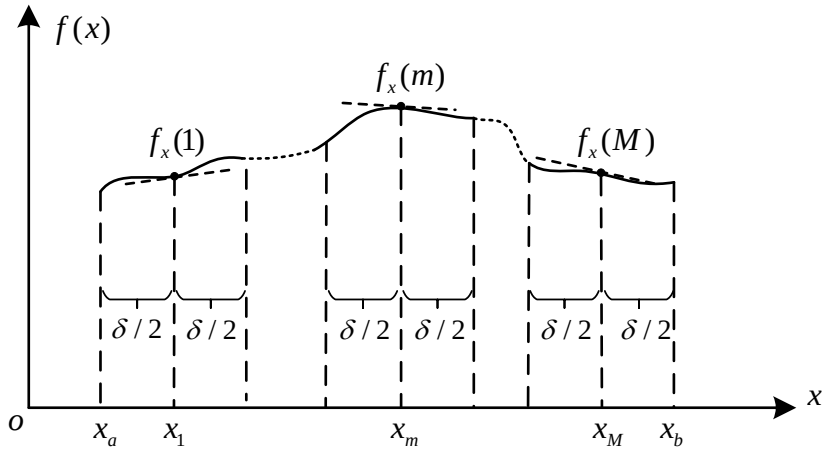

Figure B.1 – Hopkins algorithm principle with a constant step $dx = \delta_{xm} = \frac{x_b - x_a}{\mathrm{M}}$.

Appendix C

Compatibility of VCRM with GO

The Vectorial Complex Ray Model (VCRM) is an extended ray model. In some special cases, the results of the classical geometrical optics are recovered. The study of these special cases may help to understand the principle of the VCRM. In this appendix, I will show that the divergence factors of a circular infinite cylinder and a spherical particle in the VCRM is in strict consistent with those of the GO [4]. This procedure is really intuitive for the understanding of the VCRM.

C.1 Divergence factor for an infinite circular cylinder by VCRM

Consider an infinite circular cylinder of radius a illuminated normally by a plane wave. The curvature of the cylinder is zero in the direction perpendicularly to the scattering plane, so only one equation is necessary to describe the variation of the wavefronts, i.e. Eq. (3.3) is sufficient. In a scalar form, it can be written as a function of the incident angle θ_i and the refraction angle θ_r

$$\frac{k_r \cos^2\theta_r}{\mathrm{R}_2'} = \frac{k_i \cos^2\theta_i}{\mathrm{R}_2} + \frac{k_r \cos\theta_r - k_i \cos\theta_i}{a}. \tag{C.1}$$

The curvature radii of incident plane wave are infinite, so $\mathrm{R}_{2,i} = \infty$. For the reflection wave $p = 0$, $\theta_l = -\theta_i$. We deduce from Eq. (C.1) the curvature radius of emergent wavefront

$$\mathrm{R}_{2,0}^{e} = -\frac{a\cos\theta_i}{2} \tag{C.2}$$

where the sign − indicates that the reflected wave is divergent. According to Eqs. (2.40) and (3.16), the relation between divergence factor $\mathcal{D}_{2,0}$ calculated by VCRM and the divergence factor $\mathrm{D}_{2,0}$ calculated by GO is

$$\frac{\mathcal{D}_{2,0}}{a} = \left|\frac{\mathrm{R}^e_{2,0}}{a}\right| = \frac{\cos\theta_i}{2} = \mathrm{D}_{2,0} \tag{C.3}$$

Then by using Eq. C.1 for the refraction wave at the first interaction point, we find the curvature radius of the emergent wavefront given as

$$\frac{m\cos^2\theta_r}{\mathrm{R}'_{2,1}} = \frac{m\cos\theta_r - \cos\theta_i}{a} \tag{C.4}$$

that is

$$\mathrm{R}'_{2,1} = \frac{ma\cos^2\theta_r}{m\cos\theta_r - \cos\theta_i} \tag{C.5}$$

The curvature radius of the wavefront at next incident point is

$$\mathrm{R}_{2,2} = \mathrm{R}'_{2,1} - d_1 = \frac{a\cos\theta_r(2\cos\theta_i - m\cos\theta_r)}{m\cos\theta_r - \cos\theta_i} \tag{C.6}$$

where $d_1 = 2a\cos\theta_r$ is the distance the two successive interaction points. Again, the application of Eq. (C.1) for the refracted wave at the second point yields

$$\frac{k_i\cos^2\theta_i}{\mathrm{R}^e_{2,2}} = \frac{k_r\cos^2\theta_r}{\mathrm{R}_{2,2}} + \frac{k_i\cos\theta_i - k_r\cos\theta_r}{-a}. \tag{C.7}$$

Thus, $\mathrm{R}^e_{2,2}$ is given as

$$\mathrm{R}^e_{2,2} = \frac{a\cos\theta_i(m\cos\theta_r - 2\cos\theta_i)}{2(m\cos\theta_r - \cos\theta_i)} \tag{C.8}$$

So, for the first refracted wave $p = 1$, the relation between the divergence factor $\mathcal{D}_{2,1}$ calculated by VCRM and the divergence factor $\mathrm{D}_{2,1}$ calculated by GO is

$$\frac{\mathcal{D}_{2,1}}{a} = \left|\frac{\mathrm{R}'_{2,1}}{\mathrm{R}_{2,2}}\frac{\mathrm{R}^e_{2,2}}{a}\right| = \frac{m\cos\theta_i\cos\theta_r}{2\,(\cos\theta_i - m\cos\theta_r)} = \mathrm{D}_{2,1} \tag{C.9}$$

We see for the first two orders of rays (Eqs. (C.3) and (C.9)), the divergence factor of the VCRM is compatible to that of the GO for light scattering by an infinite circle cylinder. In principle, we can continue this procedure for higher order rays, but the calculation is tedious.

C.2 Divergence factor for a sphere by VCRM

When a plane wave is scattered by a spherical particle, the variation of the wavefront curvature in the scattering plane is the same as that of a circular infinite cylinder while the wavefront curvature in the plane perpendicular to the scattering plane varies at each interaction of the ray with the particle surface. So only this wavefront curvature is evaluated to obtain the divergence factor.

According to Eqs. (2.33) and (2.45), the ratio of the divergence factor of a sphere $\mathrm{D}_{sph.}$ and that of a circular cylinder $\mathrm{D}_{cyl.}$ in the GO is

$$\frac{\mathrm{D}_{sph.}}{\mathrm{D}_{cyl.}} = \frac{\sin\theta_i}{\sin\theta} \tag{C.10}$$

so, we only need to prove that the divergence factor due to the variation of the wavefront curvature in perpendicular plane is equal to $\sin\theta_i / \sin\theta$, which is independent of the order of rays.

According to Eq. (3.2), the curvature radii of the wavefronts in the plane perpendicular to the scattering plane before R'_1 and after R_1 the interaction are related to the the particle radius by

$$\frac{k_r}{\mathrm{R}'_1} = \frac{k}{\mathrm{R}_1} + \frac{k_r\cos\theta_r - k_i\cos\theta_i}{a} \tag{C.11}$$

Since the curvature radii of incident plane wave are infinite, ($\mathrm{R}_{1,i} = \infty$), the wavefront curvature radius of the reflected wave ate the first interaction point $p = 0$ is given as

$$\mathrm{R}^e_{1,0} = \frac{-a}{2\cos\theta_i} \tag{C.12}$$

So, the divergence factor in the perpendicular plane is given as

$$\frac{\mathcal{D}_{1,0}}{a} = \left|\frac{\mathrm{R}^e_{1,1}}{a}\right| = \left|\frac{1}{2\cos\theta_i}\right| = \frac{\sin\theta_i}{\sin\theta} \tag{C.13}$$

because the scattering angle $\theta = \pi - 2\theta_i$.

By using again Eq. (C.11), we get the curvature radius of the wavefront of the refracted ray at the first interaction point

$$\mathrm{R}'_{1,1} = \frac{ma}{m\cos\theta - \cos\theta_i} \tag{C.14}$$

The curvature radius at next incident point is given as

$$\mathrm{R}_{1,2} = \mathrm{R}'_{1,1} - d_1 = \mathrm{R}'_{1,1} - 2a\cos\theta_r \tag{C.15}$$

The wavefront of the refracted ray at the second interaction point is as

$$\frac{k}{\mathrm{R}^e_{1,2}} = \frac{k_r}{\mathrm{R}_{1,2}} + \frac{k\cos\theta_i - k_r\cos\theta_r}{-a} \tag{C.16}$$

Therefore, the curvature radii of the emergent wavefront is

$$\mathrm{R}^e_{1,2} = \frac{a\mathrm{R}_{1,2}}{ma - \mathrm{R}_{1,2}(\cos\theta_i - m\cos\theta_r)} \tag{C.17}$$

And finally, we get the divergence factor of $p = 1$

$$\begin{aligned}
\frac{\mathcal{D}_{1,1}}{a} &= \left|\frac{\mathrm{R}'_{1,1}}{\mathrm{R}_{1,2}}\frac{\mathrm{R}^e_{1,2}}{a}\right| \\
&= \frac{1}{a}\left|\frac{\mathrm{R}'_{1,1}\mathrm{R}^e_{1,2}}{\mathrm{R}'_{1,1} - 2a\cos\theta_r}\right| \\
&= \frac{1}{a}\left|\frac{ma}{2(m\cos\theta_r - \cos\theta_i)[m - \cos\theta_r(m\cos\theta_r - \cos\theta_i)]}\right| \\
&= \left|\frac{m\sin\theta_r}{2(\sin\theta_r\cos\theta_i - m\sin\theta_r\cos\theta_r)(\cos\theta_i\cos\theta_r - m\sin^2\theta_r)}\right| \\
&= \left|\frac{\sin\theta_i}{\sin\theta}\right|
\end{aligned} \tag{C.18}$$

where the refraction law $\sin\theta_i = m\sin\theta_r$, the scattering angle $\theta = 2(\theta_r - \theta_i)$ and $\sin^2\theta_r + \cos^2\theta_r = 1$ are used.

Eqs. (C.13) and (C.18) show the same the divergence factor between GO and VCRM in perpendicular plane for $p = 0$ and 1 as expected, the compatibility for VCRM to GO of light scattering by a spherical particle is therefore proved.

Bibliography

[1] C. B. Boyer, *The rainbow, from myth to mathematics*. Princeton University Press, New Jersey, 1987.

[2] O. Darrigol, *A history of optics from Greek antiquity to the nineteenth century*. Oxford University Press, New York, 2012.

[3] G. B. Airy, "On the intensity of light in the neighbourhood of a caustic," *Transactions of the Cambridge Philosophical Society*, vol. 6, pp. 379–402, 1838.

[4] H. C. van de Hulst, *Light scattering by small particles*. Courier Corporation, New York, 1981.

[5] C. F. Bohren and D. R. Huffman, *Absorption and scattering of light by small particles*. John Wiley & Sons, New York, 2008.

[6] J. A. Adam, "The mathematical physics of rainbows and glories," *Physics Reports*, vol. 356, no. 4-5, pp. 229–365, 2002.

[7] P. Laven, "Simulation of rainbows, coronas, and glories by use of Mie theory," *Applied Optics*, vol. 42, no. 3, pp. 436–444, 2003.

[8] D. Bäuerle, *Laser processing and chemistry*. Springer Science & Business Media, 2013.

[9] B. J. Berne and R. Pecora, *Dynamic light scattering: with applications to chemistry, biology, and physics*. General Publishing Company, Toronto, 2000.

[10] S. R. Arridge, "Optical tomography in medical imaging," *Inverse Problems*, vol. 15, no. 2, pp. R41–R93, 1999.

[11] V. Tuchin, *Tissue optics: Light Scattering Methods and Instruments for Medical Diagnosis*. Society of Photo-Optical Instrumentation Engineers (SPIE) Bellingham, WA, USA, 2015.

[12] R. A. R. Tricker, *An introduction to meteorological optics*. Mills & Boon Limited, 1971.

[13] J. A. Coakley Jr and P. Yang, *Atmospheric radiation: a primer with illustrative solutions*. John Wiley & Sons, 2014.

[14] K.-N. Liou and P. Yang, *Light scattering by ice crystals: fundamentals and applications*. Cambridge University Press, Cambridge, 2016.

[15] T. Fujii and T. Fukuchi, *Laser remote sensing*. CRC press, 2005.

[16] C. Tropea, "Optical particle characterization in flows," *Annual Review of Fluid Mechanics*, vol. 43, pp. 399–426, 2011.

[17] T. D. Fansler and S. E. Parrish, "Spray measurement technology: a review," *Measurement Science and Technology*, vol. 26, no. 1, pp. 1–34, 2014.

[18] A. H. Lefebvre and V. G. McDonell, *Atomization and sprays*. CRC press, 2017.

[19] H.-E. Albrecht, N. Damaschke, M. Borys, and C. Tropea, *Laser Doppler and phase Doppler measurement techniques*. Springer Science & Business Media, 2013.

[20] M. N. Sadiku, *Numerical techniques in electromagnetics*. CRC Press, 2000.

[21] A. Ishimaru, *Electromagnetic wave propagation, radiation, and scattering: from fundamentals to applications*. John Wiley & Sons, 2017.

[22] W. C. Chew, E. Michielssen, J. Song, and J.-M. Jin, *Fast and efficient algorithms in computational electromagnetics*. Artech House, Inc., 2001.

[23] L. Lorenz, "Lysbevægelsen i og uden for en af plane lysbølger belyst kugle," *Videnskabernes Selskabs Skrifter*, vol. 6, pp. 1–62, 1890.

[24] G. Mie, "Beiträge zur optik trüber medien, speziell kolloidaler metallösungen," *Annalen der physik*, vol. 330, no. 3, pp. 377–445, 1908.

[25] M. I. Mishchenko, "Gustav Mie and the fundamental concept of electromagnetic scattering by particles: a perspective," *Journal of Quantitative Spectroscopy and Radiative Transfer*, vol. 110, no. 14-16, pp. 1210–1222, 2009.

[26] W. Hergert and T. Wriedt, *The Mie theory: basics and applications*. Springer, 2012.

[27] G. Gouesbet and G. Gréhan, *Generalized Lorenz-Mie theories*. Springer, 2011.

[28] Q. Duan, *On the three-dimensional light scattering by a large nonspherical particle based on vectorial complex ray model*. PhD thesis, Rouen Normandie Université; Xidian University (Xi'an (Chine)), 2020.

[29] P. Debye, "Das elektromagnetische feld um einen zylinder und die theorie des regenbogens," *Phys. Z.*, vol. 9, pp. 775–778, 1908.

[30] Z.-S. Wu and H.-Y. Li, "Debye series of scattering by a multi-layered cylinder in an off-axis 2D gaussian beam," *Chinese Physics Letters*, vol. 25, no. 5, pp. 1672–1675, 2008.

[31] R. Li, H. Jiang, K. F. Ren, *et al.*, "Debye series for light scattering by a multilayered sphere," *Applied Optics*, vol. 45, no. 6, pp. 1260–1270, 2006.

[32] J. A. Lock and F. Xu, "Optical caustics observed in light scattered by an oblate spheroid," *Applied Optics*, vol. 49, no. 8, pp. 1288–1304, 2010.

[33] F. Xu, J. A. Lock, and G. Gouesbet, "Debye series for light scattering by a nonspherical particle," *Physical Review A*, vol. 81, no. 4, p. 043824, 2010.

[34] T. Wriedt, "A review of elastic light scattering theories," *Particle & Particle Systems Characterization*, vol. 15, no. 2, pp. 67–74, 1998.

[35] K. Yee, "Numerical solution of initial boundary value problems involving Maxwell's equations in isotropic media," *IEEE Transactions on Antennas and Propagation*, vol. 14, no. 3, pp. 302–307, 1966.

[36] D. M. Sullivan, *Electromagnetic simulation using the FDTD method*. John Wiley & Sons, 2013.

[37] P. Yang and K. Liou, "Finite-difference time domain method for light scattering by small ice crystals in three-dimensional space," *JOSA A*, vol. 13, no. 10, pp. 2072–2085, 1996.

[38] E. M. Purcell and C. R. Pennypacker, "Scattering and absorption of light by nonspherical dielectric grains," *Astrophysical Journal*, vol. 186, pp. 705–714, 1973.

[39] M. A. Yurkin and A. G. Hoekstra, "The discrete-dipole-approximation code ADDA: capabilities and known limitations," *Journal of Quantitative Spectroscopy and Radiative Transfer*, vol. 112, no. 13, pp. 2234–2247, 2011.

[40] R. F. Harrington, *Field computation by moment methods*. Wiley-IEEE Press, 1993.

[41] J. Song, C.-C. Lu, and W. C. Chew, "Multilevel fast multipole algorithm for electromagnetic scattering by large complex objects," *IEEE transactions on antennas and propagation*, vol. 45, no. 10, pp. 1488–1493, 1997.

[42] M. Yang, Y. Wu, X. Sheng, and K. F. Ren, "Comparison of scattering diagrams of large non-spherical particles calculated by VCRM and MLFMA," *Journal of Quantitative Spectroscopy and Radiative Transfer*, vol. 162, pp. 143–153, 2015.

[43] P. Waterman, "Matrix formulation of electromagnetic scattering," *Proceedings of the IEEE*, vol. 53, no. 8, pp. 805–812, 1965.

[44] P. C. Waterman, "Symmetry, unitarity, and geometry in electromagnetic scattering," *Physical review D*, vol. 3, no. 4, pp. 825–839, 1971.

[45] M. I. Mishchenko, L. D. Travis, and D. W. Mackowski, "T-matrix computations of light scattering by nonspherical particles: A review," *Journal of Quantitative Spectroscopy and Radiative Transfer*, vol. 55, no. 5, pp. 535–575, 1996.

[46] M. Mishchenko and P. Martin, "Peter Waterman and T-matrix methods," *Journal of Quantitative Spectroscopy and Radiative Transfer*, vol. 123, pp. 2–7, 2013.

[47] B. R. Johnson, "Invariant imbedding T matrix approach to electromagnetic scattering," *Applied Optics*, vol. 27, no. 23, pp. 4861–4873, 1988.

[48] L. Bi and P. Yang, "Accurate simulation of the optical properties of atmospheric ice crystals with the invariant imbedding T-matrix method," *Journal of Quantitative Spectroscopy and Radiative Transfer*, vol. 138, pp. 17–35, 2014.

[49] P. L. Marston, *Selected papers on geometrical aspects of scattering*. SPIE, 1994.

[50] M. Born and E. Wolf, *Principles of optics: electromagnetic theory of propagation, interference and diffraction of light*. Cambridge University Press, 1999.

[51] P. L. Marston, "Critical angle scattering by a bubble: physical-optics approximation and observations," *JOSA*, vol. 69, no. 9, pp. 1205–1211, 1979.

[52] H. Yu, J. Shen, and Y. Wei, "Geometrical optics approximation of light scattering by large air bubbles," *Particuology*, vol. 6, no. 5, pp. 340–346, 2008.

[53] K. F. Ren, F. Onofri, C. Rozé, and T. Girasole, "Vectorial complex ray model and application to two-dimensional scattering of plane wave by a spheroidal particle," *Optics letters*, vol. 36, no. 3, pp. 370–372, 2011.

[54] G. A. Deschamps, "Ray techniques in electromagnetics," *Proceedings of the IEEE*, vol. 60, no. 9, pp. 1022–1035, 1972.

[55] F. R. Onofri, K. F. Ren, M. Sentis, Q. Gaubert, and C. Pelcé, "Experimental validation of the vectorial complex ray model on the inter-caustics scattering of oblate droplets," *Optics express*, vol. 23, no. 12, pp. 15768–15773, 2015.

[56] Q. Duan, F. R. Onofri, X. Han, and K. F. Ren, "Generalized rainbow patterns of oblate drops simulated by a ray model in three dimensions," *Optics Letters*, vol. 46, no. 18, pp. 4585–4588, 2021.

[57] K. Ren, C. Rozé, and T. Girasole, "Scattering and transversal divergence of an ellipsoidal particle by using vectorial complex ray model," *Journal of Quantitative Spectroscopy and Radiative Transfer*, vol. 113, no. 18, pp. 2419–2423, 2012.

[58] K. Jiang, X. Han, and K. F. Ren, "Scattering of a gaussian beam by an elliptical cylinder using the vectorial complex ray model," *JOSA A*, vol. 30, no. 8, pp. 1548–1556, 2013.

[59] Q. Duan, R. Zhong, X. Han, and K. F. Ren, "Influence of spatial curvature of a liquid jet on the rainbow positions: Ray tracing and experimental study," *Journal of Quantitative Spectroscopy and Radiative Transfer*, vol. 195, pp. 156–163, 2017.

[60] Q. Duan, X. Han, S. Idlahcen, and K. F. Ren, "Three-dimensional light scattering by a real liquid jet: VCRM simulation and experimental validation," *Journal of Quantitative Spectroscopy and Radiative Transfer*, vol. 239, p. 106677, 2019.

[61] R. Yang, *Numerical simulation of light scattering of a pendent droplet by statistic vectorial complex ray model*. PhD thesis, Rouen Normandie Université, 2019.

[62] Q. Duan, X. Han, and K. F. Ren, "Light scattering by an infinite cylinder of arbitrarily smooth cross section based on vectorial complex ray model," *Optics Communications*, vol. 467, p. 125705, 2020.

[63] B. Sun, P. Yang, G. W. Kattawar, and M. I. Mishchenko, "On Babinet's principle and diffraction associated with an arbitrary particle," *Optics letters*, vol. 42, no. 23, pp. 5026–5029, 2017.

[64] R. T. Wang and H. Van de Hulst, "Rainbows: Mie computations and the Airy approximation," *Applied Optics*, vol. 30, no. 1, pp. 106–117, 1991.

[65] E. A. Hovenac and J. A. Lock, "Assessing the contributions of surface waves and complex rays to far-field mie scattering by use of the debye series," *JOSA A*, vol. 9, no. 5, pp. 781–795, 1992.

[66] M. P. Sentis, F. R. Onofri, L. Méès, and S. Radev, "Scattering of light by large bubbles: Coupling of geometrical and physical optics approximations," *Journal of Quantitative Spectroscopy and Radiative Transfer*, vol. 170, pp. 8–18, 2016.

[67] P. Yang and K. Liou, "Geometric-optics–integral-equation method for light scattering by nonspherical ice crystals," *Applied Optics*, vol. 35, no. 33, pp. 6568–6584, 1996.

[68] P. Yang, J. Ding, R. L. Panetta, K.-N. Liou, G. W. Kattawar, and M. Mishchenko, "On the convergence of numerical computations for both exact and approximate solutions for electromagnetic scattering by nonspherical dielectric particles," *Electromagnetic waves (Cambridge, Mass.)*, vol. 164, p. 27, 2019.

[69] H. Ling, R.-C. Chou, and S.-W. Lee, "Shooting and bouncing rays: Calculating the RCS of an arbitrarily shaped cavity," *IEEE Transactions on Antennas and propagation*, vol. 37, no. 2, pp. 194–205, 1989.

[70] C. Lee, S. Lee, and R. Chou, "RCS reduction of a cylindrical cavity by dielectric coating," *Antennas and Propagation Society International Symposium*, vol. 24, pp. 305–308, 1986.

[71] J. B. Keller, "Geometrical theory of diffraction," *JOSA*, vol. 52, no. 2, pp. 116–130, 1962.

[72] G. L. James, *Geometrical theory of diffraction for electromagnetic waves*. IET, 1986.

[73] P. Y. Ufimtsev, "Elementary edge waves and the physical theory of diffraction," *Electromagnetics*, vol. 11, no. 2, pp. 125–160, 1991.

[74] P. Y. Ufimtsev, *Fundamentals of the physical theory of diffraction*. John Wiley & Sons, 2014.

[75] R. G. Kouyoumjian and P. H. Pathak, "A uniform geometrical theory of diffraction for an edge in a perfectly conducting surface," *Proceedings of the IEEE*, vol. 62, no. 11, pp. 1448–1461, 1974.

[76] R. L. Lee and A. B. Fraser, *The rainbow bridge: rainbows in art, myth, and science*. Penn State Press, 2001.

[77] O. Vallée and M. Soares, *Airy functions and applications to physics*. World Scientific Publishing Company, 2010.

[78] J. M. Pernter and F. M. Exner, *Meteorologische optik*. BoD–Books on Demand, 2012.

[79] A. Haußmann, "Rainbows in nature: recent advances in observation and theory," *European Journal of Physics*, vol. 37, no. 6, p. 063001, 2016.

[80] H. Nussenzveig, "High-frequency scattering by a transparent sphere. II. theory of the rainbow and the glory," *Journal of mathematical physics*, vol. 10, no. 1, pp. 125–176, 1969.

[81] V. Khare and H. Nussenzveig, "Theory of the rainbow," *Physical Review Letters*, vol. 33, no. 16, pp. 976–980, 1974.

[82] H. M. Nussenzveig, "The theory of the rainbow," *Scientific American*, vol. 236, no. 4, pp. 116–128, 1977.

[83] H. M. Nussenzveig, *Diffraction effects in semiclassical scattering*. Cambridge University Press, 1992.

[84] G. Können and J. De Boer, "Polarized rainbow," *Applied Optics*, vol. 18, no. 12, pp. 1961–1965, 1979.

[85] P. Laven, "http://www.philiplaven.com/p8a.html#references," *Scattering Diagrams of the Revised Airy Theory in Parallel Polarization*, 2022.

[86] H. M. Nussenzveig, "Complex angular momentum theory of the rainbow and the glory," *JOSA*, vol. 69, no. 8, pp. 1068–1079, 1979.

[87] P. Laven, "http://www.philiplaven.com/mieplot.htm," *Software MiePlot by Philip Laven*, 2021.

[88] K. F. Ren, "https://amocops.univ-rouen.fr/en/content/download," *Softwares of VCRMEll2D and ABSPhere*, 2014.

[89] W. Möbius, "Zur theorie des regenbogens und ihrer experimentellen prüfung," *Abh. Khl. Saechs. Ges. Wiss. Math. -Phys. Kl.*, vol. 30, no. 105-254, 1907-1909.

[90] W. Möbius, "Zur theorie des regenbogens und ihrer experimentellen pr fung," *Ann. Phys.*, vol. 33, no. 16, pp. 1493–1558, 1910.

[91] C. L. Adler, J. A. Lock, and B. R. Stone, "Rainbow scattering by a cylinder with a nearly elliptical cross section," *Applied Optics*, vol. 37, no. 9, pp. 1540–1550, 1998.

[92] H. Yu, J. Shen, and C. Tropea, "Application of vector ray tracing to the computation of möbius shifts for the primary and secondary rainbows," *Applied Optics*, vol. 54, no. 31, pp. 9093–9101, 2015.

[93] J. A. Lock and G. P. Können, "Rainbows by elliptically deformed drops. I. Möbius shift for high-order rainbows," *Applied Optics*, vol. 56, no. 19, pp. G88–G97, 2017.

[94] T. Pearcey, "XXXI. the structure of an electromagnetic field in the neighbourhood of a cusp of a caustic," *The London, Edinburgh, and Dublin Philosophical Magazine and Journal of Science*, vol. 37, no. 268, pp. 311–317, 1946.

[95] M. V. Berry, "Waves and Thom's theorem," *Advances in Physics*, vol. 25, no. 1, pp. 1–26, 1976.

[96] R. Thom and D. H. Fowler, *tructural Stability and Morphogenesis: An Outline of a General Theory of Models*. CRC press, 2018.

[97] A. D. Gorman, *Waves, Caustics and Thom's Theorem*. The Pennsylvania State University, 1980.

[98] J. F. Nye, "Optical caustics in the near field from liquid drops," *Proceedings of the Royal Society of London. A. Mathematical and Physical Sciences*, vol. 361, no. 1704, pp. 21–41, 1978.

[99] M. V. Berry, J. F. Nye, and F. J. Wright, "The elliptic umbilic diffraction catastrophe," *Philosophical Transactions of the Royal Society of London. Series A, Mathematical and Physical Sciences*, vol. 291, no. 1382, pp. 453–484, 1979.

[100] M. V. Berry and C. Upstill, "IV catastrophe optics: morphologies of caustics and their diffraction patterns," *Progress in optics*, vol. 18, pp. 257–346, 1980.

[101] P. L. Marston and E. H. Trinh, "Hyperbolic umbilic diffraction catastrophe and rainbow scattering from spheroidal drops," *Nature*, vol. 312, no. 5994, pp. 529–531, 1984.

[102] J. F. Nye, "Rainbow scattering from spheroidal drops—an explanation of the hyperbolic umbilic foci," *Nature*, vol. 312, no. 5994, pp. 531–532, 1984.

[103] P. L. Marston, "Cusp diffraction catastrophe from spheroids: generalized rainbows and inverse scattering," *Optics letters*, vol. 10, no. 12, pp. 588–590, 1985.

[104] J. A. Lock, C. L. Adler, B. R. Stone, and P. D. Zajak, "Amplification of high-order rainbows of a cylinder with an elliptical cross section," *Applied Optics*, vol. 37, no. 9, pp. 1527–1533, 1998.

[105] H. Yu, F. Xu, and C. Tropea, "Simulation of optical caustics associated with the secondary rainbow of oblate droplets," *Optics Letters*, vol. 38, no. 21, pp. 4469–4472, 2013.

[106] H. Yu, F. Xu, and C. Tropea, "Optical caustics associated with the primary rainbow of oblate droplets: simulation and application in non-sphericity measurement," *Optics express*, vol. 21, no. 22, pp. 25761–25771, 2013.

[107] J. A. Lock, "Supernumerary spacing of rainbows produced by an elliptical-cross-section cylinder. I. theory," *Applied Optics*, vol. 39, no. 27, pp. 5040–5051, 2000.

[108] C. L. Adler, D. Phipps, K. W. Saunders, J. K. Nash, and J. A. Lock, "Supernumerary spacing of rainbows produced by an elliptical-cross-section cylinder. II. experiment," *Applied Optics*, vol. 40, no. 15, pp. 2535–2545, 2001.

[109] C. L. Adler, J. A. Lock, J. K. Nash, and K. W. Saunders, "Experimental observation of rainbow scattering by a coated cylinder: twin primary rainbows and thin-film interference," *Applied Optics*, vol. 40, no. 9, pp. 1548–1558, 2001.

[110] G. P. Können and J. A. Lock, "Rainbows by elliptically deformed drops. II. the appearance of supernumeraries of high-order rainbows in rain showers," *Applied Optics*, vol. 56, no. 19, pp. G98–G103, 2017.

[111] P. Laven, "Supernumerary arcs of rainbows: Young's theory of interference," *Applied Optics*, vol. 56, no. 19, pp. G104–G112, 2017.

[112] H. Yu, J. Shen, C. Tropea, and F. Xu, "Model for computing optical caustic partitions for the primary rainbow from tilted spheriodal drops," *Optics Letters*, vol. 44, no. 4, pp. 823–826, 2019.

[113] M. Berry, "Inflection reflection: images in mirrors whose curvature changes sign," *European Journal of Physics*, vol. 42, no. 6, p. 065301, 2021.

[114] M. Berry, "Distorted mirror images organised by cuspoid and umbilic caustics," *Journal of Optics*, vol. 23, no. 12, p. 125402, 2021.

[115] P. L. Marston and M. I. Mishchenko, "Scattering by relatively small oblate spheroidal drops of water in the rainbow region: T-matrix results and geometric interpretation," *Journal of Quantitative Spectroscopy and Radiative Transfer*, vol. 283, p. 108142, 2022.

[116] Y. Wu, J. Promvongsa, S. Saengkaew, X. Wu, J. Chen, and G. Gréhan, "Phase rainbow refractometry for accurate droplet variation characterization," *Optics letters*, vol. 41, no. 20, pp. 4672–4675, 2016.

[117] Y. Wu, C. Crua, H. Li, S. Saengkaew, L. Mädler, X. Wu, and G. Gréhan, "Simultaneous measurement of monocomponent droplet temperature/refractive index, size and evaporation rate with phase rainbow refractometry," *Journal of Quantitative Spectroscopy and Radiative Transfer*, vol. 214, pp. 146–157, 2018.

[118] M. Amiri and M. T. Tavassoly, "Spectral anomalies near phase singularities in reflection at Brewster's angle and colored castastrophes," *Optics letters*, vol. 33, no. 16, pp. 1863–1865, 2008.

[119] K. Jiang, *Theoretical study of light scattering by an elliptical cylinder*. PhD thesis, Rouen Normandie Université, 2013.

[120] J. W. Goodman, "Introduction to Fourier optics. 3rd," *Roberts and Company Publishers*, 2005.

[121] J. A. Lock, "Ray scattering by an arbitrarily oriented spheroid. I. diffraction and specular reflection," *Applied Optics*, vol. 35, no. 3, pp. 500–514, 1996.

[122] T. TANAKADATE, "On the theory of rainbow," *Proceedings of the Tokyo Mathematico-Physical Society. 2nd Series*, vol. 4, no. 7, pp. 134–146, 1907.

[123] M. Boitel, "On the supernumerary arcs that accompany the rainbow," *Comptes rendus de l'Acad. Des Sci. T CV*, p. 1522, 1888.

[124] C. Zhang, C. Rozé, and K. F. Ren, "Airy theory revisited with the method combining vectorial complex ray model and physical optics," *Optics Letters*, vol. 47, no. 9, pp. 2149–2152, 2022.

[125] A. S. Glassner, *An introduction to ray tracing*. Morgan Kaufmann, 1989.

[126] G. Sundberg, L. M. Zurk, S. Schecklman, and S. Henry, "Modeling rough-surface and granular scattering at terahertz frequencies using the finite-difference time-domain method," *IEEE Transactions on Geoscience and Remote Sensing*, vol. 48, no. 10, pp. 3709–3719, 2010.

[127] X. Meng, L. Guo, C. Dong, and Y. Jiao, "GO/PO method for the terahertz scattering computation of objects with multiple small-scale grooves," *IEEE Access*, vol. 7, pp. 40738–40745, 2019.

[128] N. Zhang, Y. M. Wu, J. Hu, and Y.-Q. Jin, "The fast physical optics method on calculating the scattered fields from electrically large scatterers," *IEEE Transactions on Antennas and Propagation*, vol. 68, no. 3, pp. 2267–2276, 2019.

[129] K. Falaggis, J. Rolland, F. Duerr, and A. Sohn, "Freeform optics: introduction," *Optics Express*, vol. 30, no. 4, pp. 6450–6455, 2022.

[130] K. Liu, H. Liu, E. Wei, Y. Cheng, and H. Wang, "Backward scattering of electrically large standard objects illuminated by OAM beams," *IEEE Antennas and Wireless Propagation Letters*, vol. 19, no. 7, pp. 1167–1171, 2020.

[131] F. Xu, K. F. Ren, and X. Cai, "Extension of geometrical-optics approximation to on-axis gaussian beam scattering. I. by a spherical particle," *Applied Optics*, vol. 45, no. 20, pp. 4990–4999, 2006.

[132] F. Xu, K. F. Ren, X. Cai, and J. Shen, "Extension of geometrical-optics approximation to on-axis gaussian beam scattering. II. by a spheroidal particle with end-on incidence," *Applied Optics*, vol. 45, no. 20, pp. 5000–5009, 2006.

[133] G. Guo, L. Guo, and R. Wang, "The study on near-field scattering of a target under antenna irradiation by TDSBR method," *IEEE Access*, vol. 7, pp. 113476–113487, 2019.

[134] G. Guo and L. Guo, "Hybrid time-domain ptd and physical optics contour integral representations for the near-field backscattering problem," *IEEE transactions on antennas and propagation*, vol. 67, no. 4, pp. 2655–2665, 2019.

[135] I. N. Bronshtein, K. A. Semendyayev, G. Musiol, and H. Mühlig, *Handbook of mathematics*. Springer, 2015.

[136] J. J. Stamnes, *Waves in focal regions: propagation, diffraction and focusing of light, sound and water waves.* Routledge, 2017.

Résumé

L'arc-en-ciel est l'un des plus beaux phénomènes de la nature. Le principe de sa formation a toujours attiré de nombreux scientifiques. Les propriétés des particules tels que la taille, la forme et la température peuvent être mesurés par les diagrammes de diffusion au voisinage des angles d'arc-en-ciel. Cependant, la prédiction précise ces propriétés et les diagrammes de diffusion n'est pas une tâche facile, surtout pour les grosses particules non sphériques. Le but de cette thèse est de chercher une solution à ce problème par la combinaison du modèle de rayons complexes vectoriels (Vectorial Complex ray model - VCRM en anglais) et de l'optique physique (OP), appelé VCRM+OG.

Les concepts et les lois fondamentaux de l'Optique Géométrique (GO) et OP sont d'abord introduits et examinés dans le but de leur application à la diffusion de la lumière. The OG permet de calculer l'amplitude et la phase de tous les rayons émergents au champ lointain mais échoue pour la prédiction de la diffusion dans la direction avant et près des angles d'arc-en-ciel. OP peut remédier à la diffusion avant en considérant la particule comme un disque mais la rectification de la diffusion près des angles d'arc-en-ciel est un sujet ardu depuis longtemps.

Le VCRM développé au laboratoire peut prédire l'amplitude et la phase d'un rayon à n'importe quelle position pour une particule de forme quelconque de surface lisse. Les éléments essentiels du VCRM sont présentés et appliqués à la diffusion dans un plan de symétrie d'un cylindre elliptique infini et d'un ellipsoïde pour illustrer la démarche, ses avantages et ses inconvénients. Comme le VCRM est un modèle de rayon, le défaut de la discontinuité d'intensité à l'angle de l'arc-en-ciel persiste.

Ensuite, la théorie d'Airy de l'arc-en-ciel a été examinée en utilisant notre VCRM+PO. Il est montré qu'en remplaçant l'amplitude constante et la fonction de phase cubique de la théorie d'Airy par celles calculées avec VCRM, notre méthode peut prédire très précisément les diagrammes de diffusion au voisinage de l'arc-en-ciel en polarisation perpendiculaire ou parallèle pour une particule sphérique de 10 μm à 1 mm (éclairée par la lumière visible) par rapport à la théorie rigoureuse de Debye.

La méthode VCRM+PO a été appliquée finalement à la prédiction des diagrammes de diffusion au voisinage de l'arc-en-ciel d'une particule non sphérique comme un cylindre elliptique infini et un ellipsoïde. L'effet de convergence et la position des cuspides en fonction du rayon vertical de la particule ont été mis en évidence.

On peut conclure donc que VCRM+PO est une méthode puissante pour la diffusion de la lumière par de grosses particules. Elle peut également être utilisée pour la diffusion d'une onde électromagnétique ou d'une onde acoustique.

Mots-clés: Diffusion de la lumière, arc-en-ciel, caustique, modèle vectoriel de rayon complexe, optique physique, front d'onde, facteur de divergence

ABSTRACT

Rainbow is one of the most beautiful phenomena in nature, the physical principle for its formation ever attracted many scientists. The particle parameters like size, shape and temperature can be measured by its scattering diagrams in the neighborhood of rainbow angles. However, the precise prediction of these scattering patterns is not an easy task, especially for large non-spherical particles. The aim of this thesis is to solve this problem by the combination of the Vectorial Complex ray model (VCRM) and physical optics (PO).

The fundamental concepts and laws of GO and PO are firstly introduced and examined in the purpose for their application to the light scattering of an infinite circular cylinder and a sphere. GO permits to calculate the amplitude and the phase of all the emergent rays in far field but it fails in prediction of the scattering in forward direction and near the rainbow angles. PO can remedy the scattering in the forward direction by considering the particle as a disk but the rectification of the scattering near the rainbow angles has been an arduous topic since a long time.

VCRM developed in the laboratory can predict the amplitude and the phase of a ray at any position for a particle of any shape of smooth surface. The essentials of VCRM are then presented and applied to the scattering of an infinite elliptical cylinder and an ellipsoid. Since VCRM is still a ray model the flaw of the intensity discontinuity at the rainbow angle persists.

Then, the Airy theory of rainbow has been examined using our method VCRM+PO. It is shown that by replacing the constant amplitude and cubic phase function in Airy theory by the those calculated with VCRM, our method can predict very precisely the scattering patterns in the neighborhood of rainbow in perpendicular or parallel polarization for a spherical particle from 10 μm to 1 mm (illuminated by visible light) when compared with the rigorous Debye theory.

The method VCRM+PO has been applied finally to the prediction of the scattering patterns in the rainbow region of a non-spherical particles like infinite elliptical cylinder and ellipsoid. The convergence effect and the cusp position as function of the vertical radius of the particle have been highlighted.

Therefore, VCRM+PO is a powerful method for light scattering by large particles. It can also be used in the scattering of the electromagnetic wave or acoustics wave.

Keywords: Light scattering, rainbow, caustics, vectorial complex ray model, physical optics, wavefront, divergence factor